FAULT ZONE IMAGING AND EARTHQUAKE DETECTION WITH DENSE SEISMIC ARRAYS

A Dissertation
Presented to
The Academic Faculty

by

Zefeng Li

In Partial Fulfillment
of the Requirements for the Degree
Doctor of Philosophy (Geological Sciences) in the
School of Earth and Atmospheric Sciences

Georgia Institute of Technology
August 2017

FAULT ZONE IMAGING AND EARTHQUAKE DETECTION WITH DENSE SEISMIC ARRAYS

Approved by:

Dr. Zhigang Peng, Advisor
School of Earth and Atmospheric Sciences
Georgia Institute of Technology

Dr. Ken Ferrier
School of Earth and Atmospheric Sciences
Georgia Institute of Technology

Dr. Andrew Newman
School of Earth and Atmospheric Sciences
Georgia Institute of Technology

Dr. James McClellan
School of Electrical Computer Engineering
Georgia Institute of Technology

Dr. Josef Dufek
School of Earth and Atmospheric Sciences
Georgia Institute of Technology

Date Approved: May 08, 2017

To My Family

ACKNOWLEDGEMENTS

I would like to thank my advisor Dr. Zhigang Peng for his careful guidance and full support throughout my doctoral study. He provided timely and valuable advices to both my research and personal development, which helped me grow as an independent scientist. He gave me enough room to explore new ideas, and provided constructive suggestions that improved the work significantly. Moreover, his devotedness and diligence in seismology has inspired me in the past years and will definitely have profound influence on my future career.

I also would like to thank my collaborators Dr. Yehuda Ben-Zion, Dr. Hongfeng Yang, Dr. Haijiang Zhang, Dr. James McClellan and his student Lijun Zhu. The work would not be possible without their input. I thank my defense committee for their kind support and valuable comments. During my Ph.D. period, I benefitted very much from my colleagues at Geophysics group of Georgia Tech, including Dongdong Yao, Xiaofeng Meng, Chastity Aiken, Chenyu Li, and Dr. Ghassan AlReigib and his group at Center for Energy and Geo Processing. Whenever I met problems about scientific knowledge or technical details, they were always available for discussion and help.

Finally, I would like to express my deep gratitude to my family. My mother, although illiterate, has provided irreplaceable support for my pursuit in higher education. My father, with only two-year schooling, had keen aspiration after knowledge and set himself as an example in lifelong learning. My wife Haixia is the person who I owe most. Without her sacrifice and support, I could not have had such a fruitful journey in my doctoral study.

TABLE OF CONTENTS

LIST OF TABLES

LIST OF FIGURES

LIST OF SYMBOLS AND ABBREVIATIONS

δt	Delay time between fast and slow shear waves
Φ	Polarization direction of fast shear wave, or fast direction
SHmax	Maximum horizontal compression stress
SWS	Shear-wave splitting
FZHW	Fault zone head wave
STA/LTA	Short-term-average to long-term-average ratio
SNR	Signal-to-noise ratio
SAF	San Andreas Fault
NAF	North Anatolian Fault
SJFZ	San Jacinto Fault Zone
SCSN	Southern California Seismic Network

SUMMARY

Natural earthquakes occur on faults. The relationship between fault zone structures and earthquake behaviors remains one of the most interesting problems in seismology. As an important tool to detect earthquakes and image the Earth's interior, seismic arrays have been widely used since the 1960s. Recordings from closely spaced uniform seismometers improved imaging resolution of the Earth's interior and enhanced detection of small-magnitude earthquakes. However, such an increase in data size also poses a challenge in the way that we used to handle and processing seismic data. Visual inspection and manual selection become less practical and sometimes impossible.

My PhD research focuses on obtaining high-resolution seismic properties (e.g., seismic anisotropy and velocity contrast) along major fault zones in California and Turkey, and detecting seismic events/phases multi-scale dense seismic arrays. To process large-size seismic data, I developed several tools to automatically pick P, S and fault zone head waves. Using recently emerging ultra-dense arrays, I proposed a new metric, termed local similarity, to detect weak microseismic signals that are barely above noise level. These studies share the same feature, i.e., using automatic techniques to extract earthquake and structure information from big seismic data recorded by dense or ultra dense arrays. The results are expected to provide valuable information on fault zone structures and microseismic behaviors. The tools developed in these studies can be applied to a wide range of research topics.

CHAPTER 1. INTRODUCTION

1.1 Overview

Natural earthquakes occur on faults. Most of large fault systems reside on plate boundaries. In contrast with the continuous deformation processes in plate interiors, the deformation and evolution on plate-bounding faults are highly episodic and irregular. Earthquake nucleation, rupture process, seismic radiation are largely controlled by the structures and properties of fault, which makes earthquake physics dictated to a large extent by fault zone properties [*Ben-Zion*, 2008]. Aftershock distribution and rupture area usually correlate with fault geometries and asperities [e.g., *McNamara et al.*, 2014; *Michael and Eberhart-Phillips*, 1991; *Schorlemmer and Wiemer*, 2005]. In addition, rock stiffness and fluid conditions around faults can strongly affect their frictional properties and slip behaviors, i.e. regular earthquakes, slow earthquakes, or stable sliding [*Scholz*, 1998; *Sibson*, 1994]. Hence, earthquake physics is largely dictated by fault zone properties [*Ben-Zion and Sammis*, 2003].

As an important tool to study earthquakes and fault zone properties, seismic arrays have been widely used in modern seismology since 1950 [*Filson*, 1975]. Recordings from close spaced uniform seismometers are used to effectively enhance signal-to-noise ratio and can significantly improve imaging resolution of the Earth's interior [*Rost and Thomas*, 2002]. Seismic arrays can also be used to image rupture properties of very large earthquakes [*Ishii et al.*, 2005; *Meng et al.*, 2012]. With the recent sensor advancement, seismic arrays become much denser than before, which provide unique opportunities for imaging fault zone properties and detect seismic events

with unprecedented resolution [*Lin et al.*, 2013; *Inbal et al.*, 2016].

Although many exciting findings in modern seismology benefit from the increasing density of seismic arrays, the associated increase in data size also poses a significant challenge in the way of handling and processing seismic data. Especially, visual inspection and manual selection is becoming less practical. Many popular techniques used in major data centers and seismological research originated from the age when seismic data were in relatively small size and computational power was limited.

The theme of my Ph.D. focuses on fault zone properties and seismic phase/event detections with large seismic data recorded by dense arrays. In the first two chapters, I investigated two important properties of fault zones, i.e. seismic anisotropy within and outside fault damage zones (CHAPTER 2), and velocity contrast along fault interface (CHAPTER 3), which are briefly introduced in Sections 1.1.1 and 1.1.2, respectively. When processing large volume of seismic data during my research, I also developed several tools to automatically pick P, S and fault zone head waves (FZHWs), in order to reduce human workload and improve phase picking accuracy (CHAPTER 3).

The recent years have also seen the emergence of ultra-dense arrays with hundreds to thousands of sensors and tens- to hundred-meter interstation spacing [e.g., *Lin et al.*, 2013; *Ben-Zion et al.*, 2015]. Such arrays, sometimes called large-N arrays, provide unprecedented detection capability for small magnitude earthquakes and other unconventional sources. In order to improve detection completeness of small-magnitude events with Large-N arrays, I developed a new method for seismic event detection (CHAPTER 4). The overview of this subject is presented in Section 1.1.3.

1.1.1 Seismic anisotropy and shear-wave splitting

Seismic anisotropy describes the variation of seismic wave speed with the propagation direction. In the upper crust, seismic anisotropy is commonly caused by the fractures or cracks that align at a preferred direction along the maximum horizontal compressive stress direction SHmax [*Booth and Crampin*, 1985; *Leary et al.*, 1990; *Crampin*, 1991; *Zhang and Schwartz*, 1994]. This is termed as stress-controlled anisotropy. The other category, i.e. structure-controlled anisotropy, includes sedimentary bedding planes, mineral orientation, and fracture alignment along active fault zones [*Boness and Zoback*, 2006].

Seismic anisotropy leads to an interesting phenomenon termed shear wave splitting (SWS)), which describes the observations that seismic shear waves split into two orthogonal components that arrive at slightly different times [*Savage*, 1998; *Long and Silver*, 2009]. SWS is usually quantified by two parameters: polarization direction of the fast component Φ and delay time δt between the fast and slow components. SWS is extensively used to study various structures in the Earth's interior. Teleseismic phases SKS and SKKS are used to image the upper mantle flow direction [*Barruol*, 2004] and D'' layer properties [*Restivo and Helffrish*, 2006]. In comparison, direct S waves are used to estimate density and alignment of fractures in the upper crust [*Peng and Ben-Zion,* 2004; *Yang et al.*, 2011] and volcanic arcs [*Teanby et al.*, 2004; *Savage et al.*, 2010].

1.1.2 Velocity contrast and fault zone head waves

Velocity contrast across fault interface, on the other hand, is likely caused by asymmetric damage zones in which fractures are localized on one side of the fault wall [*Ben-Zion,* 2001; *Sibson*, 2003], and/or lithological contrast across fault strike [e.g., *Michael and Eberhart-Phillips,* 1991; *Thurber et al.*, 2006; *Wdowinski et al.*, 2007]. The

existence of velocity contrast can produce significant differences in seismic radiation, compared to a homogeneous solid, as shown in earthquake rupture simulations [*Shi and Ben-Zion*, 2006]. It leads to a dynamic change on the normal stress in the rupture tips, predicting a statistically preferred rupture direction when an earthquake initiates in a bimaterial interface and propagates unilaterally [e.g. *Dalguer and Day*, 2007; *Ampuero and Ben-Zion*, 2008]. This makes the investigation of velocity contrast relevant to seismic hazard assessment, because rupture propagating towards and away from a site produces significantly different ground motions [*Olsen et al.*, 2006].

Bimaterial interfaces are expected to generate FZHW, which refract along the fault interface with the seismic velocity of the faster side and radiate from the fault to the slow side [*Ben-Zion and Malin*, 1991]. For stations on the slow side, direct P waves sample the slow velocity block and FZHW mostly sample the fast side. Hence, the arrival time differences between them can be used to estimate the velocity contrast on both sides [*Ben-Zion et al.*, 1992]. In addition, FZHW sample the portion of the fast velocity block immediately neighboring the fault interface, which is critical for dynamic rupture propagation. FZHW have been observed along several major plate boundary faults. These include the San Andreas Fault [*Ben-Zion and Malin*, 1991; *McGuire and Ben-Zion*, 2005; *Lewis et al.*, 2007; *Zhao et al.*, 2010; *Allam et al.*, 2014] and the North Anatolian Fault in northwestern Turkey [*Bulut et al.*, 2012; *Najdahmadi et al.*, 2016]. A recent study also found evidence of FZHW on the Garzê-Yushu Fault, an intraplate fault that ruptured during the 2010 Mw6.9 Yushu earthquake [*Yang et al.*, 2014]. These studies of FZHW provide clear evidence for the existence of bimaterial interface along major faults in both interplate and intraplate settings.

1.1.3 Seismic event detection

Seismic event detection is a fundamental operation in observational seismology, which is to detect seismic events of particular interest from continuous recordings. The major goal is to detect events as small as possible while avoid too many false events (which are noise or events out of interest). Traditional earthquake detection workflow includes phase picking (identifying impulsive arrivals of seismic phases) and phase association (grouping these phases into an individual event) [*Allen*, 1982]. Phase picking is commonly done by an energy detector such as short-term average over long-term average (STA/LTA) ratio [*Allen*, 1978; *Earle and Shearer*, 1994]. As computer power increases, many sophisticated detection algorithms have been proposed. Most of these algorithms continuously search over possible source locations by shifting and stacking waveforms or their variants (e.g., envelope, STA/LTA, normalized waveform). Outstanding examples include the source scanning algorithm [*Kao and Shan*, 2004], coalescence microseismic mapping [*Drew et al.*, 2013], and backprojection [*Ishii et al.*, 2005; *Kiser and Ishii*, 2013].

Different from this category, template matching, or matched filtering, takes advantage of predetermined events and cross-correlates them with continuous recordings to detect events with high waveform similarities [*Gibbons and Ringdal*, 2006]. This is based on the fact that nearby seismic events may have similar source mechanisms and ray paths, and hence similar waveforms. Template matching usually detects new events at a factor of 5-10 times the original catalog [*Shelly et al.*, 2007; *Peng and Zhao*, 2009; *Yang et al.*, 2009], but requires predetermined templates as inputs, which are not always available. An auto-detection technique could be used to build template events from

scratch [*Brown et al.*, 2008]. However, with $O(N^2)$ type scaling, this is computationally very intensive and hence cannot be applied to longer time series. Other approaches, such as fingerprinting [*Yoon et al.*, 2015], combination of source-scanning and template matching [*Frank et al.*, 2015], or earthquake search-engines [*Zhang et al.*, 2014] have also been proposed for fast and robust detection of seismic events.

1.2 Motivations

High-resolution fault zone imaging and small-magnitude seismicity around active faults can be achieved with dense fault zone arrays. Hereby I utilize dense arrays for studying shear-wave anisotropy and velocity contrast in fault zones and use Large-N arrays to detect very small seismic events. Seismic anisotropy provide important constraints on crustal stress field and structural heterogeneities, and is indicative of fracturing and rock damage along source-receiver paths. However, how shear-wave anisotropy vary in very-fine scale and how it is mapped at depth remains unclear. In this subject I conducted three projects to address these problems [*Li et al.*, 2014, 2015; *Li and Peng, in prep.*].

As mentioned before, many seismic processing tasks, e.g. seismic phase picking, rely on human's visual inspection and hand-picking. For example, properly picking FZHWs is an essential but laborious task to study fault zone velocity contrast. As a large volume of data from dense arrays poses a challenge in seismic data processing, automation of these processing tasks become necessary, which not only reduces human workload, but also avoids subjective selection and increases research reproducibility. Therefore, I developed two packages for seismic phase picking of P, S and FZHW respectively, and tested them with data sets recorded in central and southern California [*Li and Peng*, 2016a, 2016b].

An extreme case of dense arrays is the recent emerging Large-N arrays that contain hundreds to thousands of sensors and tens- to hundred-meter interstation spacing. These arrays have been increasingly used in the recent years and are expected to significantly enhance seismic monitoring/imaging capability. However, traditional technique is no longer effective to handle such type of new data. Accordingly, my recent work [*Li et al.*, *in revision*] aimed to develop a new detection method that fully takes advantage of the features of Large-N arrays.

1.3 Thesis Organization

This thesis consists of the content from four published papers [*Li et al.*, 2014; *Li et al.*, 2015; *Li and Peng*, 2016a; *Li and Peng*, 2016b], one manuscript in revision [*Li et al.*, in revision] and one manuscript in preparation [*Li and Peng*, in prep.]. In Chapter 2, I present the studies of SWS measurement in the San Jacinto Fault Zone (SJFZ) using temporary and permanent arrays, the whole southern California using two-decade data from Southern California Seismic Network. I also present an SWS tomography method to map the spatial distribution of SWS into 3-D along the North Anatolian Fault in Turkey. Chapter 3 focuses on two automatic phase picking methods that I developed for general P and S waves and more specific FZHWs. In Chapter 4, I present the development of a high-resolution seismic detection method for ultra-dense arrays. This method is applied to a 5200-sensor array to detect ultra-weak seismic signals in the City of Long Beach, California. Finally in Chapter 5, I conclude the thesis by summarizing the findings and developed techniques, and discuss potential directions of future work.

CHAPTER 2. SHEAR-WAVE ANISOTROPY IN FAULT ZONES

The results presented in this chapter are from *Li et al.* [2015a], *Li and Peng* [in prep], and *Li et al.* [2014].

2.1 Spatial Variations of Shear-wave Anisotropy near the San Jacinto Fault Zone, southern California

Summary

We examine crustal anisotropy at several scales along and across the SJFZ by systematically measuring shear wave splitting (SWS) parameters. The analyzed data are recorded by 86 stations during 2012-2014, including five linear dense arrays crossing the SJFZ at different locations, and other autonomous stations within 15 km from the main fault trace. Shear phase arrivals and SWS parameters (fast directions and delay times) are obtained with automated methods. The measurements quality is then assessed using multiple criteria, resulting in 23,000 high quality measurements. Wwe find clear contrast of fast directions between the SW and NE sides of the SJFZ. Stations on the SW side have fast directions consistent overall with SHmax, while stations on the NE side show mixed patterns likely reflecting lithological/topographic variations combined with fault zone damage. The fast directions in the Anza gap section with relatively simple fault geometry agree with the inferred SHmax, and the delay times at an array within that section are smaller than those observed at other across-fault arrays. These indications of less pronounced damage zone in the Anza section compared to other segments of the SJFZ are correlated generally with geometrical properties of the surface traces. Significant variations of fast directions on several across-fault arrays, with station spacing on the orders of a few tens of meters, suggest that shallow fault structures and near-surface layers play an important role in controlling the SWS parameters.

2.1.1 Introduction

SWS refers to a phenomenon that seismic shear waves propagating through an anisotropic medium split into two orthogonally polarized waves with different velocities. The interior of the earth is anisotropic to different levels at different depth sections owing to many factors. Crustal anisotropy may be considered as a result of preferential alignment of fluid-filled cracks that are parallel to the direction of SHmax [*Nur and Simmons*, 1969; *Crampin*, 1978; *Leary et al.*, 1990]. However, studies associated with large strike-slip faults usually observe fast directions that are parallel to the fault strike, especially for stations close to the fault trace [e.g., *Peng and Ben-Zion*, 2004; *Boness and Zoback*, 2006; *Audet*, 2014; *Rasendra et al.*, 2014], consistent with elevated rock cracking along the fault zones [e.g., *Finzi et al.*, 2009; *Hamiel et al.*, 2009]. Other causes of crustal anisotropy include preferential mineral alignment, remnant features of paleostress, and sedimentary layering [*Alford*, 1986; *Sayers*, 1994; *Aster and Shearer*, 1992]. In general, a mixture of mechanisms on a single station can be produced due to different ray paths of seismic events [e.g., *Cochran et al.*, 2003; *Peng and Ben-Zion*, 2004].

Analysis of SWS has been extensively conducted along a number of major fault zones. Examples include the San Andreas Fault [*Silver and Savage*, 1994; *Boness and Zoback*, 2006; *Liu et al.*, 2008], the San Jacinto Fault [e.g., Peacock et al., 1988; *Crampin et al.*, 1990; *Aster et al.*, 1990; *Yang et al.*, 2011], the North Anatolian fault [e.g., *Peng and Ben-Zion*, 2004; *Eken et al.*, 2013], the Chelongpu fault [*Liu et al.*, 2004], the Nojima fault [*Tadokaro and Ando*, 2002], and the Marlborough fault [*Balfour et al.*, 2005]. These studies primarily focused on spatial distributions of shear wave anisotropy, providing important constraints on their physical mechanisms and spatial extent of the fault damage zone [*Li et al.*, 1994; *Shih and Meyer* 1990; *Zhang and Schwartz*, 1994; *Peng and Ben-Zion, 2004*; *Li et al.*, 2014]. Temporal variations of SWS parameters associated with earthquake occurrence and volcano eruptions have been reported, sometimes with controversy [e.g., *Crampin et al.*, 1990; *Aster et al.*, 1990; *Tadokoro and Ando*, 2002; *Gerst and Savage*, 2004; *Crampin and Gao*, 2004; *Liu et al.*, 2005; *Peng and Ben-Zion*, 2005; *Unglert et al.*, 2011; *Godfrey et al.*, 2014].

High-resolution spatial variations of anisotropy around active faults can be achieved with data of dense arrays close to the fault. For example, *Cochran et al.* [2003, 2006]

used dense cross-fault arrays to study spatio-temporal variations anisotropy following the 1999 M7.1 Hector Mine and the 2004 M6.0 Parkfield earthquakes. Such closely spaced stations provide more reliable and detailed measurements of near-fault anisotropy parameters at resolutions on the order of tens of meters.

The SJFZ is an important target for SWS analysis, due to its structural complexity, highly active seismicity and dense seismic instrumentation. The SJFZ contains multiple fault segments that have different slip rates and seismic behaviors [e.g., *Fialko*, 2006; *Sanders and Kanamori*, 1984]. Since 1890, a number of moderate earthquakes (M>6) have occurred along portions of the SJFZ [*Sykes and Nishenko*, 1984; *Sanders and Kanamori*, 1984]. The Anza seismic gap has not experienced any major earthquakes in the past 200 years [*Salisbury*, 2012], although paleoseismic investigations suggest over 20 large earthquakes in the past 4000 years in the region [*Rockwell et al.*, 2015].

In the present paper I conduct a comparative study of within-, near- and off-fault crustal anisotropy, using local earthquake data from January 2012 to June 2014 recorded by five spatially-dense linear arrays that cross the SJFZ at several locations and other temporary and permanent near-fault stations (Figure 2.1). Although several SWS studies using local seismic data have been conducted in this region [e.g., *Peacock et al.*, 1988; *Aster and Shearer*, 1992; *Yang et al.*, 2011], our study utilizes new data sets with dense cross-fault arrays and provides detailed results on spatial variations of near-fault anisotropy. I obtain SWS measurements using an automatic MFAST code [*Savage et al.*, 2010], and compare fast directions with regional compressive stress to identify various features along and across the SJFZ. The results show clear contrast of fast directions between the SW and NE sides of the fault and among different fault zone sections. In the localized Anza seismic gap area, low delay times and fast directions that are quasi-parallel to SHmax are observed. In the other more complex sections of the SJFZ diverse patterns are found. Notable variations of fast directions along several cross-fault arrays document significant changes of fault zone shear anisotropy at scales of tens of meters.

2.1.2 Data

To investigate fault mechanics and evolutionary behavior of the SJFZ, data was used from a dense seismic network (Figure 2.1) deployed around the SJFZ between 2010 and

2014 [e.g., *Allam et al.*, 2014; *Kurzon et al.*, 2014]. The deployment includes five small-aperture linear arrays with instrument spacing 25-50 m across several segments of the SJFZ and additional near-fault stations. From NW to SE, the five linear arrays are Black Burn (BB), Ramona (RA), Sage Brush (SB), Dry Wash (DW), and Jackass Flat (JF). The linear arrays were deployed approximately perpendicular to the surface trace of the fault, with lengths ranging from ~180 m to ~450 m. To compare on- and off-fault anisotropy and augment the along-strike measurements, I also include 42 temporary and permanent stations within 15 km from the main SFJZ trace, which is approximated by a line passing through the center of the SGB array (33.5397° N, 116.5917° W) with an azimuth of 127° (Figure 2.1).

The analyzed data consist of local earthquakes listed in the Southern California Seismic Network catalog from January 2012 to June 2014, during which the linear arrays were operational. I select events using the following criteria: 1) magnitude larger than 1 but less than 4 to ensure signal-noise-ratio and avoid strong source effects; 2) close to the examined station, i.e., epicentral distance less than 25 km from the station or array center; 3) incident angle < 45° assuming a straight ray path (i.e., depth larger than the epicentral distance) to avoid interference of converted phases [*Booth and Crampin*, 1985]. These criteria result in data associated with 2697 local earthquakes and 22548 waveforms recorded by the five linear arrays and 22033 waveforms recorded by other on- and off-fault stations. On average each station recorded data associated with a few hundred up to one thousand events.

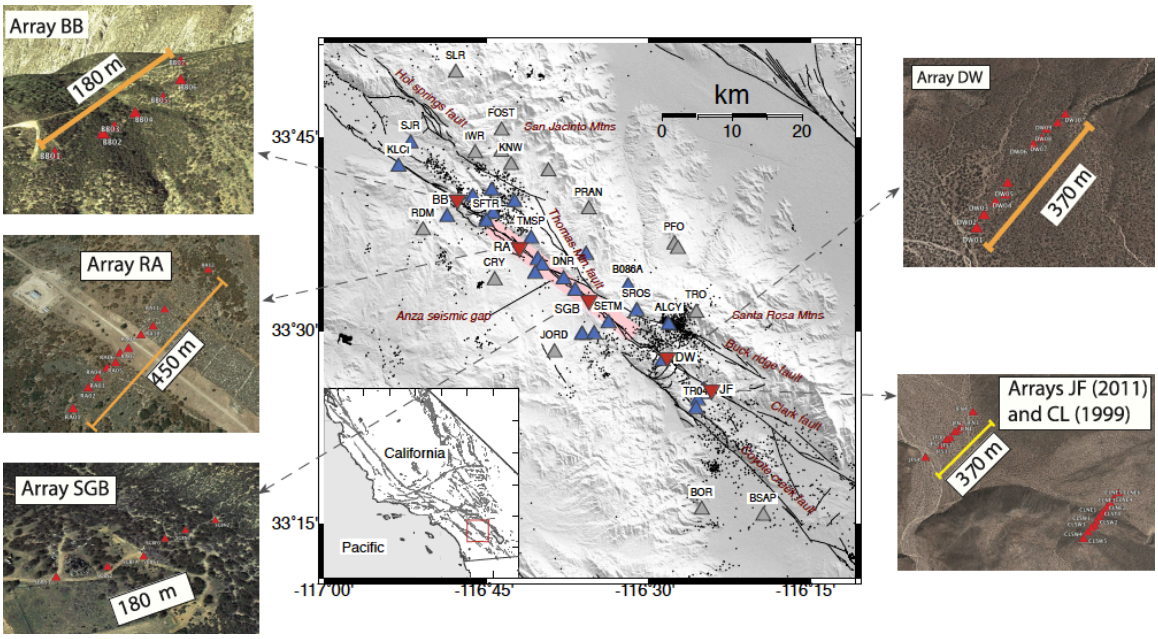

Figure 2.1 Map showing the study region along the San Jacinto Fault in Southern California. Active faults in this region are marked as black lines, and seismicity (1<M<4) between 01/01/2012 and 06/02/2014 is marked as black dots. Blue and gray triangles are individual stations within and outside 5 km from the main fault trace. Inverse triangles are across-fault arrays whose zoom-in plots are shown on top of Google map. The inset shows a map of California with the red rectangle marking the location of the study region.

2.1.3 Method

Because the analyzed data set is relatively large, it is more efficient (and objective) to pick S phases automatically. I use a "predict, search, invert and repeat" method for automatic picking of S phases [*Li and Peng*, 2016]. The method has the following steps: 1) compute theoretical arrival using a reference velocity model; 2) search for arrival around the expected theoretical time using a signal-noise ratio function; 3) With these candidate picks, invert for improved velocity model starting with the initial reference model; 4) repeat steps 1-3 until picks and velocity models become stable. I start with a 1D velocity model of 5 km spacing in depth and velocity value averaged from the Southern California Earthquake Center community 3D velocity model [*Magistrale et al.*, 1996]. The S phases are picked on horizontal components and only those with signal-to-noise ratio (SNR) > 3 are used. To ensure the consistency of S picks among the stations

in each linear array, I align the S picks on the stations in each array with waveform cross-correlations (Figure 2.2). For other fault zone stations, I simply use the picks from the predict-and-search method. I note that small pick inaccuracy is unlikely to affect the SWS measurement significantly. The SWS measuring algorithm, outlined below, analyzes multiple time windows around the pick and uses the best results. The algorithm's flexibility in the precise choice of time window start and end makes it insensitive to small changes in pick arrivals of tenths of seconds.

Fast directions and delay times are computed using the automated program MFAST [*Savage et al.*, 2010]. The code determines the splitting parameters using the covariance matrix method of *Silver and Chan* [1991]. It performs grid-search over the fast direction-delay time (Φ-δt) space to minimize the energy on the component perpendicular to the initial polarization of shear waves. This process is applied over multiple measurement windows. The minimum and maximum window lengths are set using the dominant period of each waveform. Cluster analysis is then performed to determine the best solution among all the windows [*Teanby et al.*, 2004]. The code also uses an automatic algorithm to determine the best band-pass filter for single measurement in terms of the tradeoff between frequency bandwidth and SNR. However, because the dominant frequency for shear waves of local earthquakes is 5-10 Hz, I fix the band-pass filter to be 1-15 Hz and apply this to all the data [*Yang et al.*, 2011]. **Figure 2.3** illustrates the analysis procedure with data of one example event.

The MFAST program also provides multiple parameters for assessing the measurement quality. Here I select measurements that satisfy: 1) SNR>3; 2) delay time δt < 0.4 s and δt error < 0.1 s; 3) fast direction Φ error <15^o; 4) cluster grade A and B (referring to *Savage et al.* [2010] for definition); 5) 20^o < polarization angle of fast wave against incoming wave < 70^o. These criteria are either empirical or inherent from previous studies [e.g., *Peng and Ben-Zion*, 2004; *Savage et al.*, 2010]. Out of 44,300 event-station pairs, 23,000 high quality measurements (~52%) are obtained and used in subsequent studies.

The statistical analysis of Φ is performed generally using the von Mises method [e.g., *Mardia and Jupp*, 2000; *Cochran et al.*, 2003; *Peng and Ben-Zion*, 2004; *Yang et al.*,

2011]. This method essentially treats fast directions as vectors with unit length and averages them as a mean. However, there is a drawback when the fast direction distribution is bimodal or scattered. For example, if a station has two groups of preferential directions at 0° and 90° controlled by different mechanisms, the mean value from von Mises method would be 45°, with no physical meaning. Therefore, I only use the resultant length R (ranging from 0 to 1) to quantify the variance of the directions. For the dominant directions, I use a 10°-long sliding window to calculate the number of measurements within that window, and shift the window every 1° between 0° and 180°. Given the 180° ambiguity of fast direction, special treatment is needed near the boundaries. For example, the number of measurements within the window centered at angle 0° is counted in the range of [0° – 5°] and [175°– 180°]. Finally, the center of the window with most measurements is taken as the dominant fast direction.

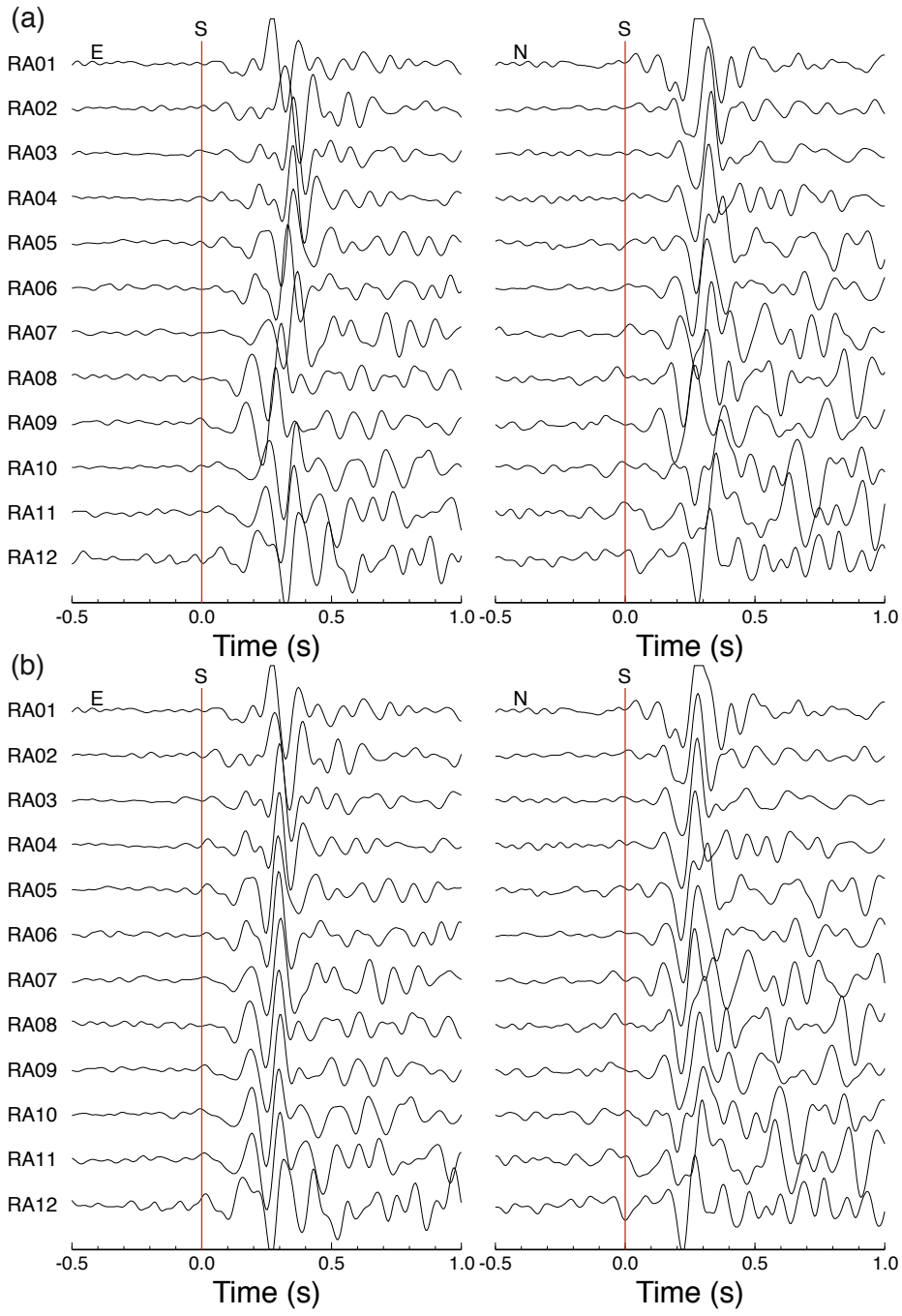

Figure 2.2 An example of automatically picked S arrivals on RA array. (a) Automatic S picks on E and N components using the predict-and-search method [*Li and Peng*, 2015]. (b) S picks that are refined by waveform cross-correlation on basis of (a).

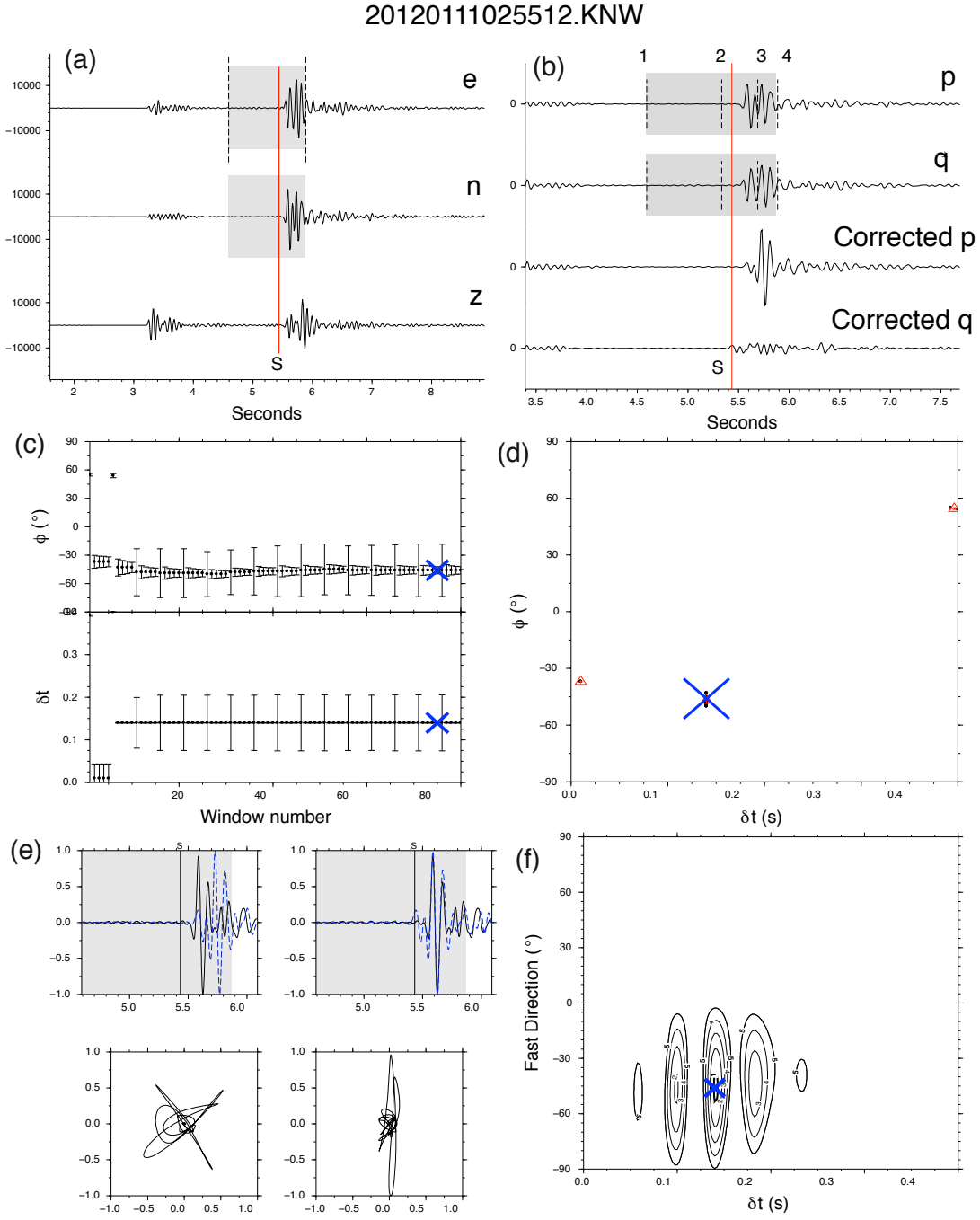

Figure 2.3 An example of automatic SWS analysis on an M 1.13 event (event ID 15235601) recorded at station KNW. (a) 1-15 Hz filtered waveform. Red line marks the S pick. The vertical dashed lines and the gray shading mark the time window used in the SWS analysis. (b) The top two components that are rotated to incoming polarization parallel (p) and perpendicular (q) direction. The bottom two are components corrected with the determined delay time and fast direction. Dash lines mark the possible range for the starting (1, 2) and ending (3, 4) of the window. (c) The fast directions and delay times that are determined from 80 different time

windows. (d) The distributions of fast directions and delay times determined from different time windows. The blue X marks the best cluster based on the criteria outlined in *Teanby et al.* [2004]. (e) Waveforms (top) and particle motions (bottom) for the original (left) and SWS corrected (right) waveforms. (f) Contours of the second eigenvalue of the covariance matrix for difference fast directions and delay times. The blue cross corresponds to the best-fitting parameters (delay time δt = 0.15 s, fast direction Φ = –45°).

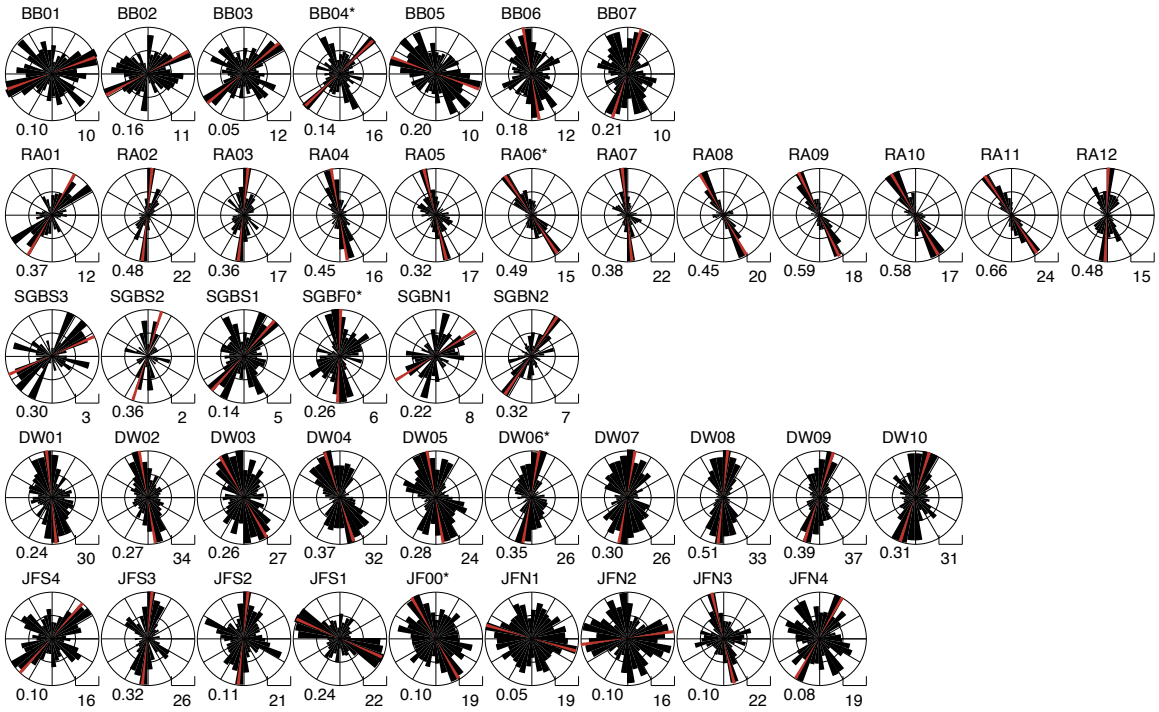

Figure 2.4 Rose diagrams of the fast directions on the five cross-fault arrays. The number at the lower right denotes the number of measurement for unit length. The number at the lower left denotes the resultant length. For each array the station from left to right corresponds to SW to NE across the fault.

2.1.4 Results

Figure 2.4 shows the rose diagram of fast directions from data of the five linear arrays. The RA array, which is located in the Anza seismic gap, displays highly consistent fast directions. From SW to NE across the fault, the dominant fast directions change gradually from NE-SW to NW-SE. Station RA12, which is at the NE edge of the array and somewhat separated from the remaining stations of the array, shows fast direction along N-S, different from the transition trend shown by stations RA01-RA11. The DW array indicates reasonably consistent fast directions, although with slightly larger scatter,

with changing dominant fast directions from NW-SE to NE-SW for stations across the faults (from SW to NE). In contrast to the clear dominant fast directions at the RA and DW arrays, the BB, SGB, and JF arrays show considerable scattering in fast directions. The scattering at the SGB array is partially attributed to the small number of high-quality results (many of the measurements are rejected by the selection criteria). The BB and JF arrays have many stations with resultant length less than 0.2, showing bimodal or disordered fast directions.

The delay times for all five arrays are plotted against their event depths in Figure 2.5. Figure S 2.1 provides a similar plot for delay times versus hypocentral distances. The delay times at each station usually have one standard deviation as large as 50-80% of the mean. A general pattern is that the delay times have no significant dependence on event depth at most stations. One possible exception is that at some stations in the RA array the delay times weakly correlate with depths. However, it should be noted that the number of measurements with high delay times on the RA array is smaller than that for the other arrays, making the correlation less reliable.

Figure 2.6 and Figure 2.7 display the rose diagrams of fast directions and delay times versus depth for stations that are within 5 km from the main fault branch. Figure 2.8 and Figure 2.9 show the same quantities for stations with distance from the main fault greater than 5 km. The corresponding plots for delay-time versus hypocentral distances are shown in Figure S 2.2 and Figure S 2.3. I note that this simple grouping criterion cannot be used to judge the distance from individual fault trace, since the SJFZ has complex geometry and multiple branches. Nevertheless, in comparison with the BB, SGB and JS fault zone arrays, most stations in both groups show clear preferential fast directions (Figure 2.6 and Figure 2.8). High scattering in delay times can be seen at individual stations, and there is no significant depth dependence for most stations, except a few such as stations JORD, FRD, RRSP, TMSP and TFRD.

Some of the employed stations were included in previous studies, which can be used to check the consistency of results. For example, waveforms recorded at station KNW were analyzed by *Peacock et al.* [1988], *Crampin et al.* [1990], *Aster et al.* [1990] and *Yang et al.* [2011]. All these studies indicated a consistent fast direction about 30° to west,

which is also obtained in our analysis (Figure 2.8). Similar agreement is found for the results associated with stations CRY, DNR, FRD, SND, SRL and WMC.

Bimodal distributions of fast orientations are observed at some stations, e.g. TR02, SROS (Figure 2.6) and FOST, RDM (Figure 2.8). These may result from multiple mechanisms present in the vicinity of the stations [e.g., *Peng and Ben-Zion*, 2004]. Analyzing the back azimuthal dependence of SWS measurements can clarify the origin of different mechanisms. To explore this, I project the measurements for each station in stereonet, but find no evidence of back azimuthal dependence at these stations (Figures S 2.4-S 2.6). For example, station FOST has two preferential directions, N40°W and N80°E. The event clusters both from the SW and NW display a mixture of the two patterns. This indicates there are likely pervasive mixed anisotropy mechanisms (or conjugate joint fractures) surrounding the stations with bimodal distributions.

Figure 2.10 provides a summary map of the mean fast directions scaled by the mean delay times. The preferential fast directions are plotted with SHmax derived from the focal mechanism inversions of *Yang and Hauksson* [2013]. A general observation is that stations on the SW side of the fault show fast directions largely consistent with the SHmax direction. In contrast, the fast directions on the NE side of the fault show mixed patterns. Some fast directions are sub-parallel to fault strike (e.g., IWR, PRAN, B086A and TRO), while others are parallel or subparallel to the SHmax direction (e.g., GVAR1, BALD) and a few are neither parallel to the fault nor the SHmax direction (e.g., PSPR and FOST).

Stations that are close to the SJFZ (including the across-fault arrays) also indicate mixing patterns. Around the Anza seismic gap (approximately from the RA to SGB array), the fast directions agree well with the SHmax direction at stations TMSP, HSSP, WMC, DNR, and SETM. As mentioned, the RA array in this region shows clear preferential fast directions, with a gradual change across the fault from NE-SW to NW-SE. At the SGB array, the fast directions are rather scattered (Figure 2.4), but the mean fast directions are generally to the NE-SW, roughly perpendicular to the SJFZ strike. The fast directions at array BB are also scattered, and the dominant directions are to the NE-SW for stations on the SW side, and nearly N-S for stations on the NE side. Between arrays BB and RA, the fast directions at stations RHIL, RRSP and SFTR are aligned

between the SJFZ fault strike and the SHmax directions. Close to arrays DW and JF, station SROS has fast direction parallel to the SJFZ fault, while station ALCY has fast direction parallel to the SHmax direction, consistent with the fast directions at the 5 stations NE of the fault in the DW array. In comparison, station DWRPT immediately to the SW of array DW has a fast direction that is between the SHmax direction and the SJFZ strike, consistent with the directions at the five stations in the DW array SW of the fault. Finally, stations near array JF have fast directions that are either parallel to the SHmax direction, or at a high angle to it, consistent with the scattered patterns observed within the JF array (Figure 2.4).

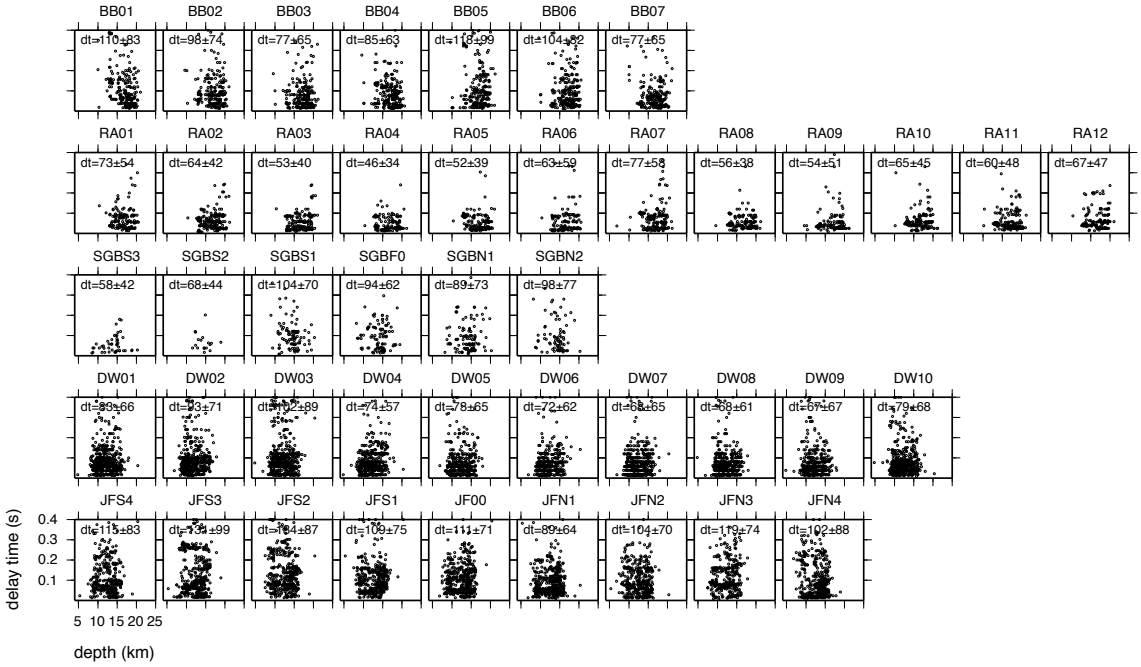

Figure 2.5 Delay times versus event depth on the cross-fault arrays. The station name, average and standard deviation of δt are marked on top of each panel.

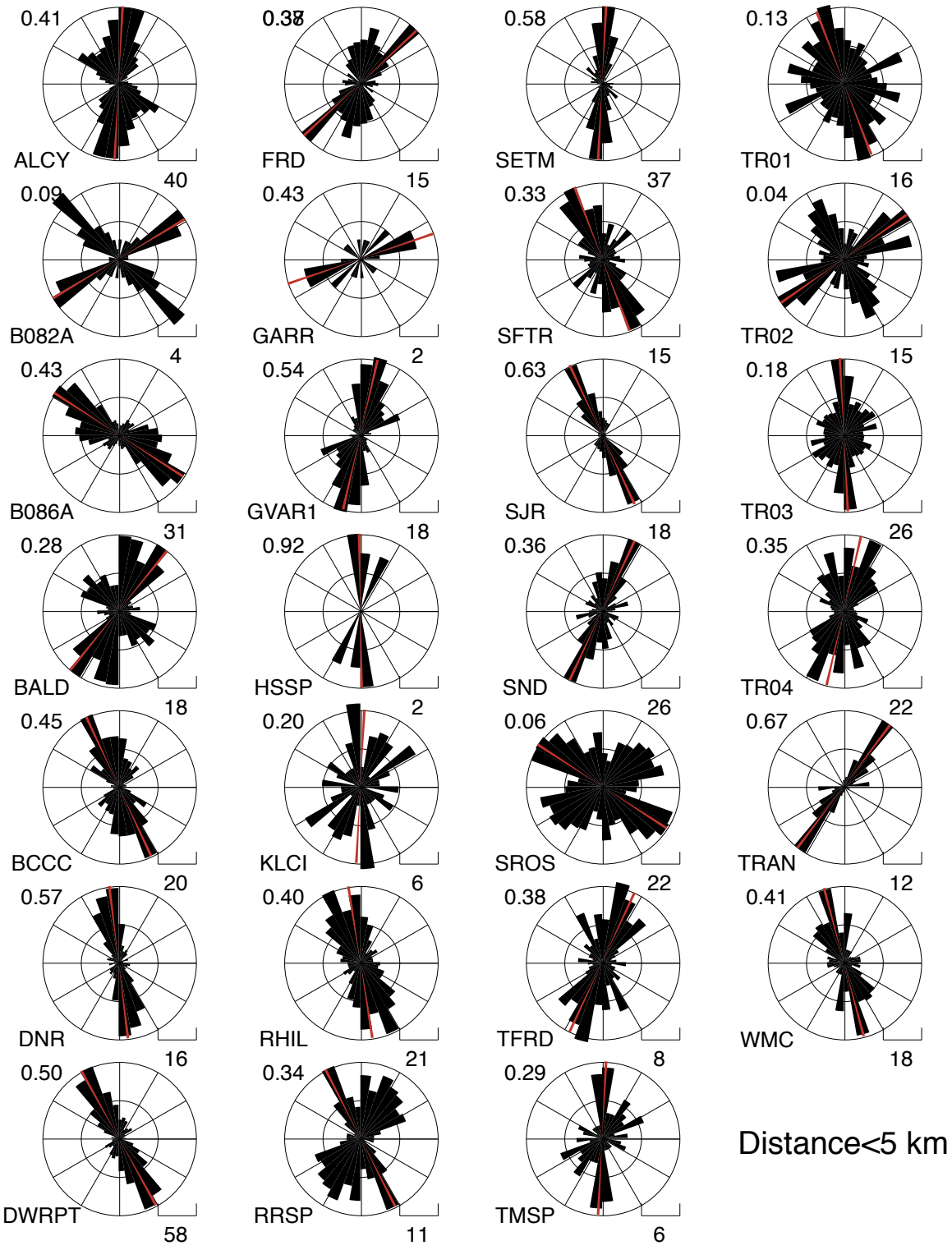

Figure 2.6 Rose diagrams of the fast directions on the stations that are less than 5 km from the main fault. Other symbols/notations are the same as in Figure 2.4.

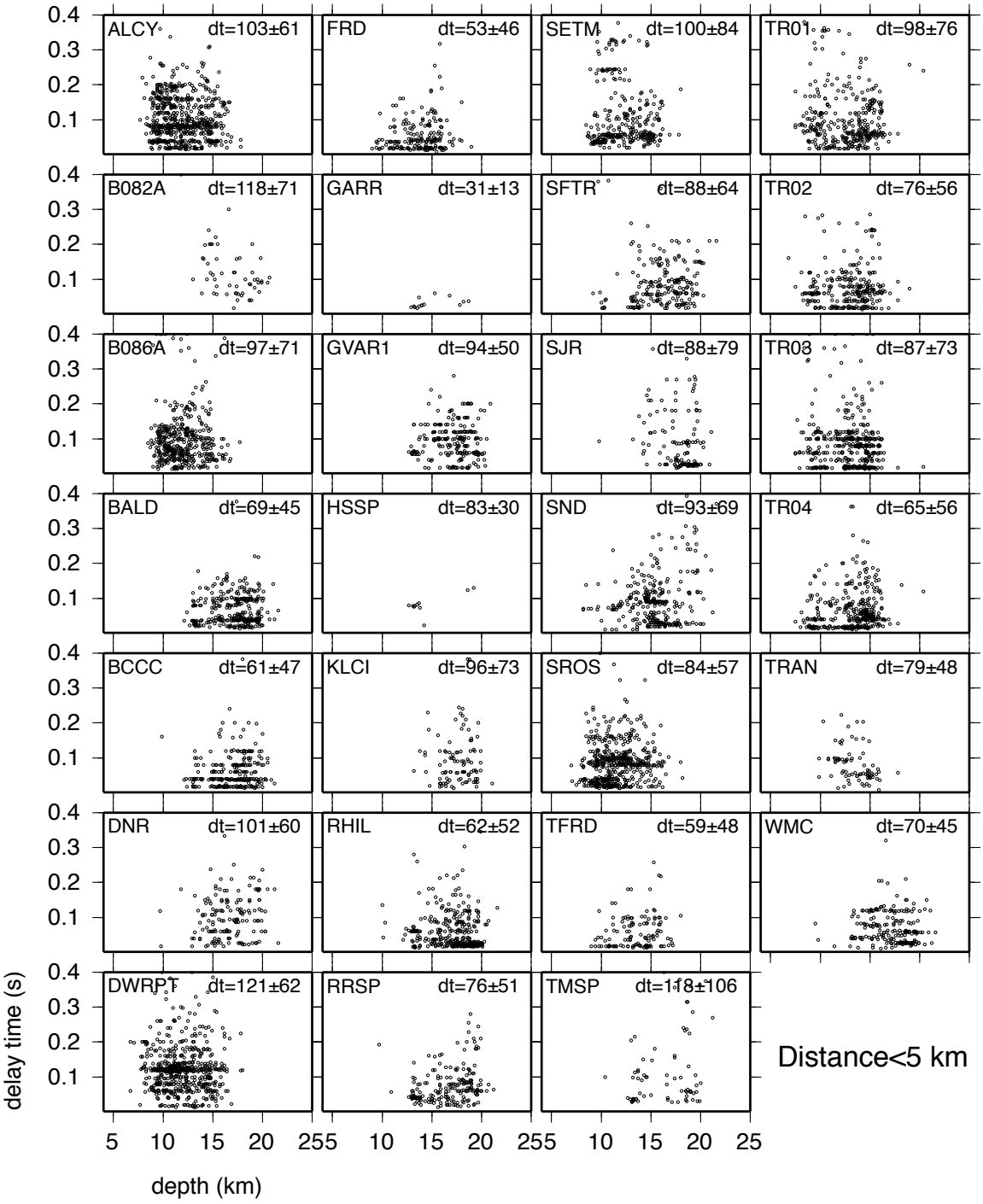

Figure 2.7 Rose diagrams of the fast directions on the stations that are less than 5 km from the main fault. Other symbols/notations are the same as in Figure 2.4.

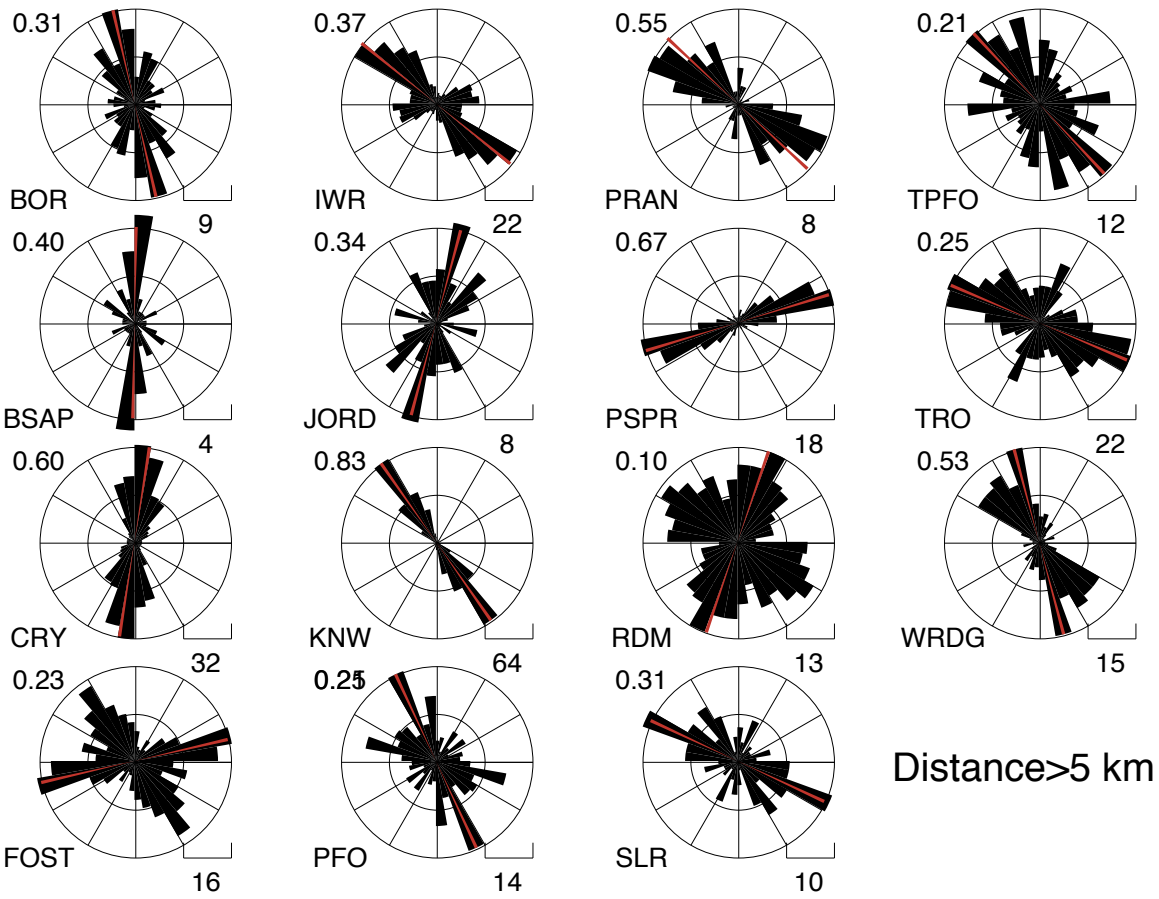

Figure 2.8 Rose diagrams of the fast directions on the stations that are more than 5 km from the main fault. Other symbols/notations are the same as in Figure 2.4.

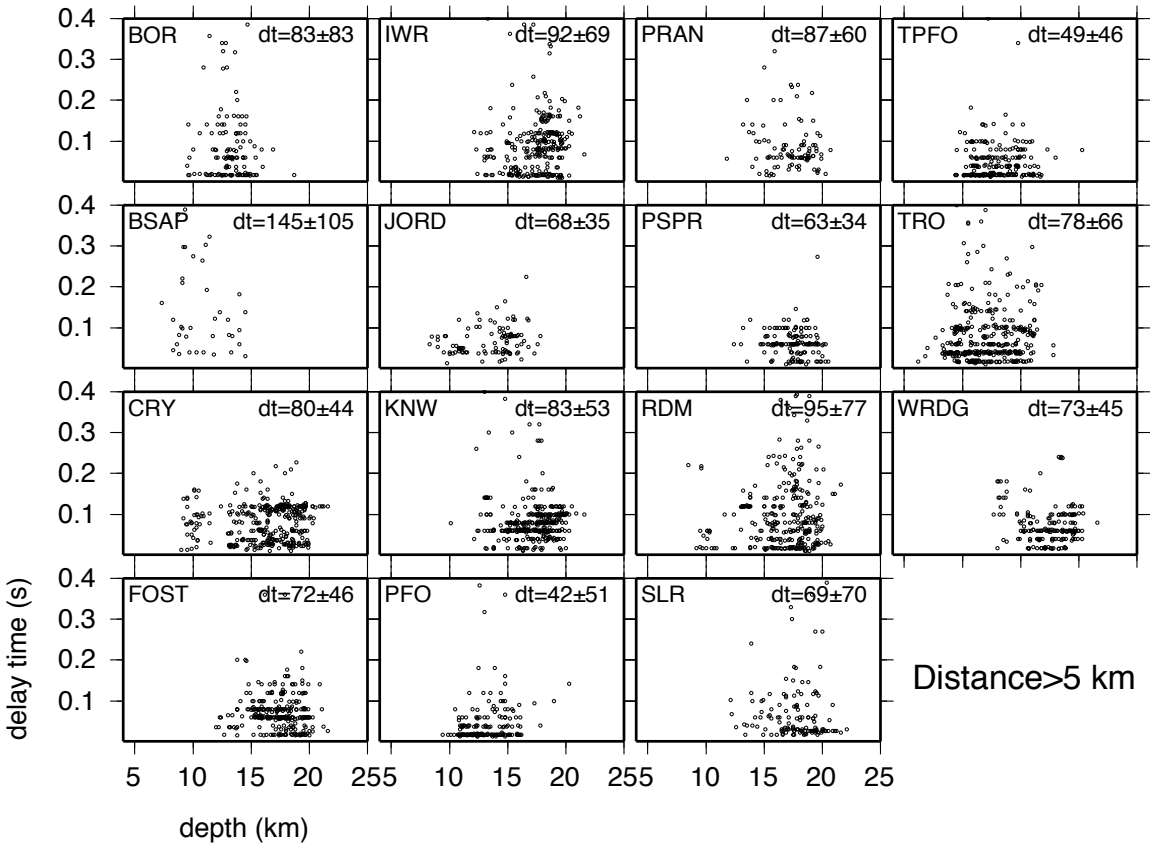

Figure 2.9 Delay times versus event depth on the stations that are more than 5 km from the main fault. Other symbols/notations are the same as in Figure 2.5.

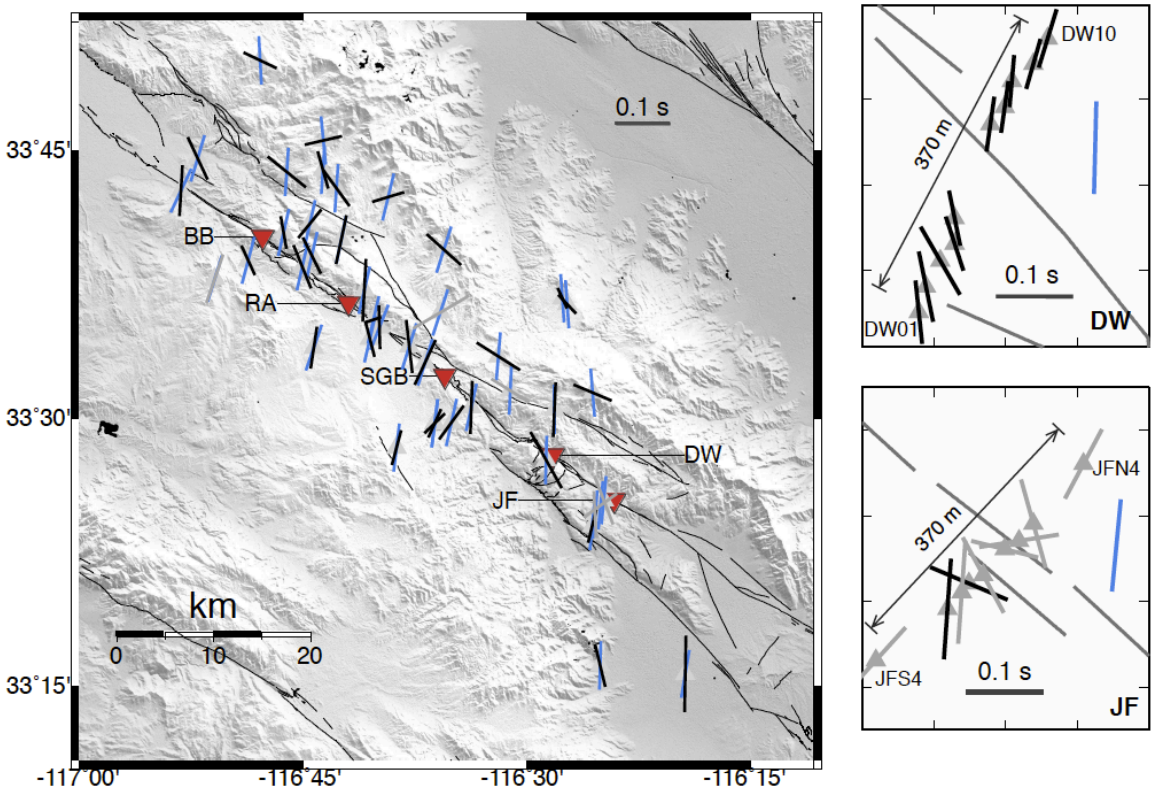

Figure 2.10 Summary of the dominant fast directions and average delay times observed at all stations along the San Jacinto Fault Zone. The gray lines mark the active faults. Black bars are oriented along the dominant fast directions and scaled by the average delay times. Blue bars denote the orientations of maximum horizontal compressive directions from the stress model of *Yang and Hauksson* [2013]. The five boxes show the zoom-in plots for the five arrays. Gray bars show fast directions with resultant length less than 0.2, indicating poor concentration of fast directions.

2.1.5 Discussion and conclusion

I systematically measured the SWS parameters within and around the SJFZ, using seismograms recorded by five across-fault linear arrays and various standalone stations (Figure 2.1). The recording stations sample properties of fault zone damage and the opposite sides of the fault at various sections of the SJFZ. The results are generally compatible with those from previous studies [e.g., *Aster and Shearer*, 1992; *Yang et al.*,

2011], but I also find significant variations of shear-wave anisotropy in both along-strike and across-fault directions in the SJFZ.

In general, stations on the SW side of the fault have fast directions that align well with nearly N-S SHmax direction. The stress field derived from focal mechanism inversions shows no distinct variations, and most of SHmax directions have very small angle with respect to the north [*Yang and Hauksson*, 2013]. This suggests that anisotropy on the SW side of the SJFZ is likely controlled by regional maximum compressive stress [e.g., *Yang et al.*, 2011]. On the other hand, many stations on the NE sides have fast directions that are subparallel to the local fault strike. A few stations also have fast directions that are almost normal to the SJFZ strike (e.g., GVAR1 and BALD).

The regions around active fault sections within the broad damage zones indicated by tomographic studies [*Allam et al.*, 2012, 2014; *Zigone et al.*, 2015] have mixed orientations. Stations in the Anza gap (NW of the trifurcation area) generally have fast directions that are parallel to the regional SHmax directions. However, stations in the trifurcation area (SE of array SGB) have scattered fast directions. While some stations have near-fault parallel directions (e.g., SROS), others have fast directions closer to the SHmax directions (e.g., ALCY and SETM), consistent with the complex fault geometries and damaged rocks in this region. Finally, the fast directions associated with the dense arrays RA and DW show systematic variations across the fault. The measurements at the other three dense arrays are more scattered.

Previous studies suggested that the crustal anisotropy at some stations around the SJFZ were controlled by local alignment of anisotropic layers. For example, *Aster and Shearer* [1992] documented that the well-defined initial shear wave polarization of N40^{o}W at station KNW is consistent with the local alignment of anisotropic bedrock minerals such as biotite. In the region of station KNW, the NE side of the SJFZ is rather complex with multiple fault branches (e.g., the Hot Spring fault, the Thomas Mountain fault, and the Buck Ridge fault) and several mountains with changing topographies (the San Jacinto and Santa Rosa Mountains) covered by sedimentary and metamorphic rocks. Since sedimentary bedding and mineral alignments in metamorphic rocks can lead to structural-induced anisotropy that is different from stress-induced anisotropy, it is

possible that mixed fast directions along and to the NE side of the SJFZ could be produced by anisotropic bedrock layers within a relatively small region.

I do not have detailed local geological information for all stations to confirm whether local rock properties are the primary reason for fast directions not consistent with the regional stress field. Nevertheless, I argue that shear-wave anisotropy in various stations around the SJFZ are likely controlled by fault zone rock damage. For example, the fast orientations at array RA in the Anza gap changes systematically from nearly N-S (regional SHmax) directions to sub-parallel fault direction. This is consistent with the rock damage asymmetry (shifted to the NE) observed from field mapping [*Dor et al.*, 2006], fault zone trapped waves [*Lewis et al.*, 2005] and local earthquake tomography [*Allam and Ben-Zion*, 2012; *Allam, et al.*, 2014]. High angle of polarization to the strike of damage zones may reflect stiffness anisotropy (i.e., low stiffness normal to the damage zone) observed at other active faults [*Pischiutta et al.*, 2012, 2013].

I note that the results have significant variations of fast directions over the short-aperture across-fault arrays, as well as scattered delay times at single stations. Some values could be affected by measurement errors and/or other fault-zone related signals. For example, cycle skipping (i.e., matching between the fast wave and slow wave with a cycle shift) could result in erroneous measurements of both fast directions and delay times. Although the employed MFAST program utilizes a multiple-window approach to mitigate this issue, it may not remove it completely [*Savage et al.*, 2010]. In addition, beyond shear wave splitting, damaged rocks and velocity contrasts in the fault zone structure produce additional seismic phases such as fault zone head waves [*Ben-Zion*, 1990; *Ben-Zion and Malin*, 1991], trapped waves [*Ben-Zion and Aki*, 1990; *Lewis et al.*, 2005], and diffracted waves [*Yang and Zhu*, 2010] and various scattered phases [*Hong and Menke*, 2006; *Hillers et al.*, 2013]. In particular, fault zone head waves and diffracted waves may arrive earlier than the first arrivals and smear the waveform of direct S waves, leading to the erroneous in SWS measurement. For example, Figure 2.2b shows precursory signals before the large-amplitude S wave at stations RA01-RA04. This is interpreted as the splitting signals, but I cannot rule out the possibility that they are generated by other causes (fault zone refraction/diffraction). These complications may

result in scattered measurements observed at some fault zone (and some off-fault) stations.

As mentioned, the fast directions in the Anza gap (starting from the RA array and ending slightly south to the SGB array) agree with the SHmax estimates. The Anza gap is in the central portion of the SJFZ, and it is geometrically simple with an active surface trace connected with the Clark Fault further to the south. The agreement between the fast directions and SHmax is consistent with this simple geometry. Although scattered, most delay times at array RA are less than 0.1 s (Figure 2.5), and the mean value is less than those observed at other across-fault arrays (Figure 2.10). This suggests that the degree of anisotropy is less at array RA, as compared with other arrays. *Yang et al.* [2014] examined P-arrival travel time differences across the fine linear fault zone arrays and found relatively small time differences between the two-end stations at array RA, suggesting that low-velocity damage zone is less developed in the Anza gap.

The inclusion in the analysis data from five dense across-fault arrays allows us to study spatial variations of anisotropy in a fault zone region at scales of tens of meters. Arrays JF and BB have scattered fast directions, while array SGB has fast directions that are nearly perpendicular to the local fault strike. Arrays RA and DW have more consistent fast directions, and they also vary systematically across the fault (Figures 2.4 and 2.10). In particular, the fast directions at the RA array in the relatively simple Anza section change from nearly stress-parallel (SW side) to fault-parallel (NE side). The largest change is observed right across the surface fault trace (RA07). At station RA01 and RA12 in both ends of the array, the fast direction returns to be near stress-parallel. The pattern is somewhat reversed at array DW in the complex trifurcation area, where the fast directions on the SW side are closer to the fault strike, while those on the NE side of the fault are sub-parallel to SHmax.

The existence of fractures with nearly fault-parallel direction leads to approximately fault-parallel fast direction, which has been extensively observed in many fault zones [e.g., *Savage et al.*, 1990; *Fletcher et al.*, 1990; *Peng and Ben-Zion*, 2004; *Liu et al.*, 2005; *Boness and Zoback*, 2006; *Liu et al.*, 2008]. If we assume that stations in the fault damage zones record predominately fault-parallel fast directions, our results would imply the existence of damage zones approximately beneath RA06 – RA11 for the RA

array and beneath DW01 – DW05 for the DW array. On the other hand, results from body wave travel times suggest low velocity zones below RA01 – RA07 and DW06 – DW12 [*Yang et al.*, 2014], which is almost the opposite from our results.

We speculate that these differences are related to the fact that travel time delays (and fault zone trapped waves) are sensitive to the entire crack populations in the low-velocity damage zones, while SWS is mostly controlled by a subset of cracks that has a preferred direction. In this sense, these phenomena are complementary rather than reflecting the same structure. Further analysis is needed to better quantify the location, thickness and depth extent of the fault damage zone in relation to various seismic signals (e.g., shear-wave and stiffness anisotropy, guided waves). This will be the subject of future work.

2.1.6 Supplementary figures

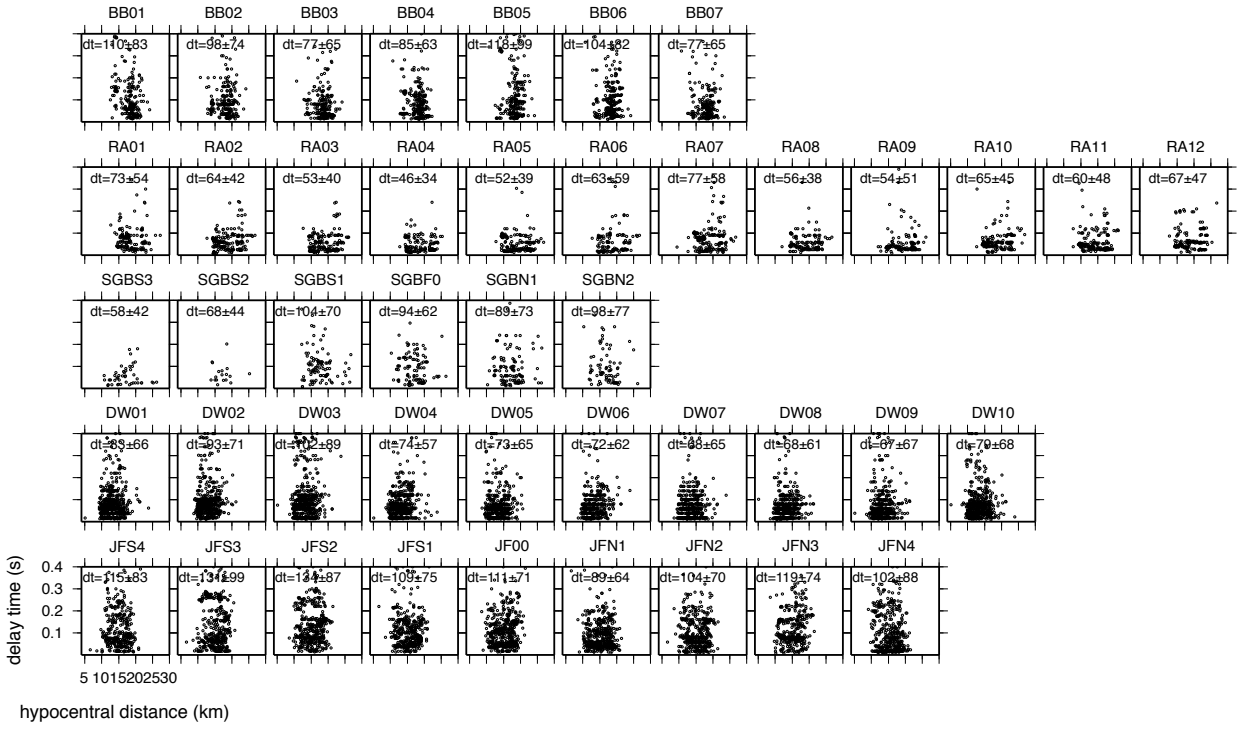

Figure S 2.1 Delay times versus event depth on the cross-fault arrays. The station name, average and standard deviation of δt are marked on top of each panel.

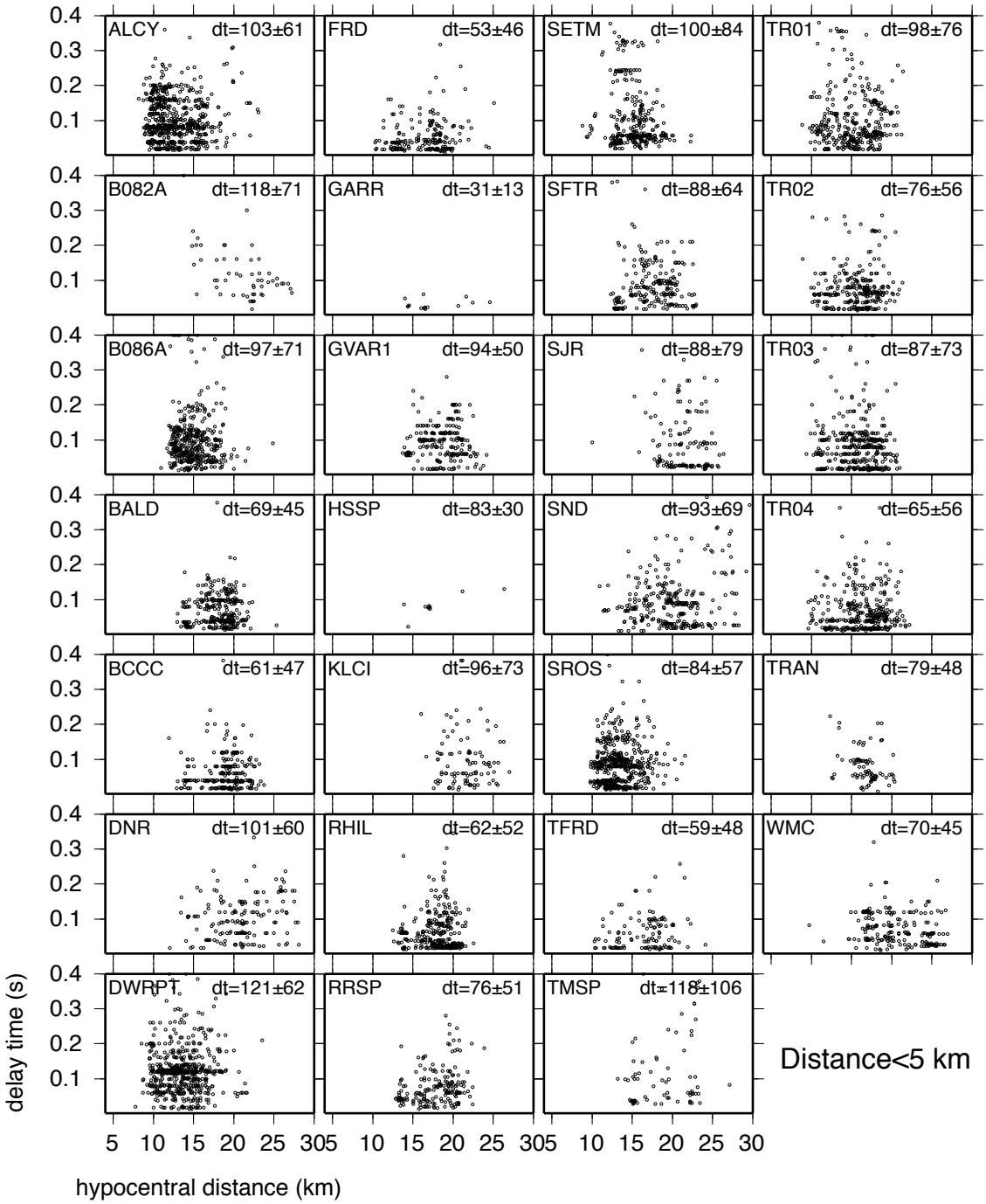

Figure S 2.2 Delay times versus event depth on the stations that are 5 km within the main fault. Other symbols/notations are the same as in Figure S 2.1.

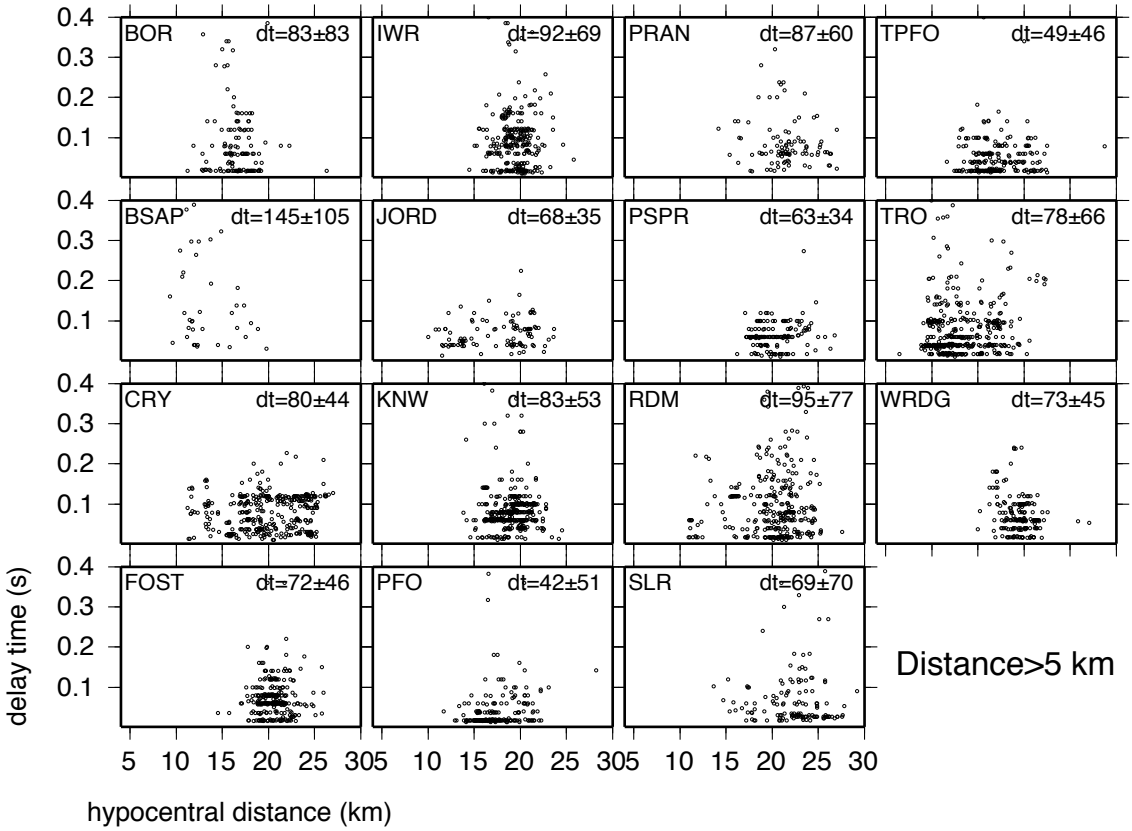

Figure S 2.3 Delay times versus event depth on the stations that are more than 5 km from the main fault. Other symbols/notations are the same as in Figure S 2.1.

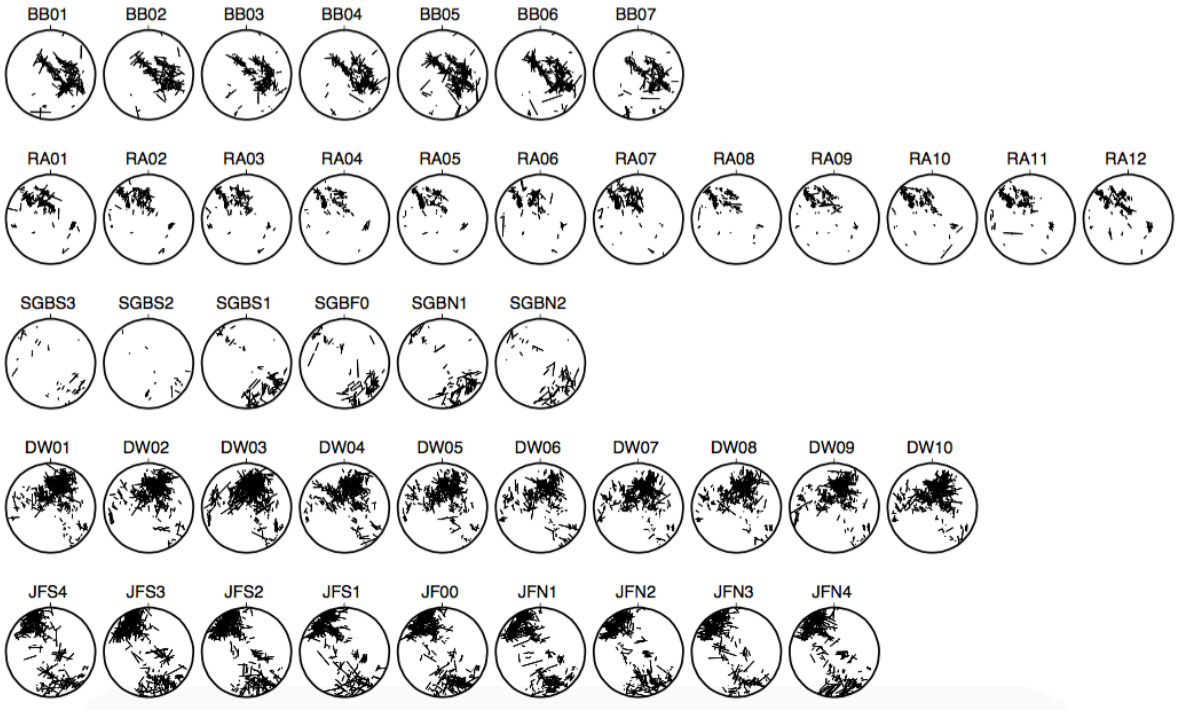

Figure S 2.4 Stereonet projections of SWS measurements on the linear arrays. The black bars are oriented along the measured fast directions and scaled by delay times.

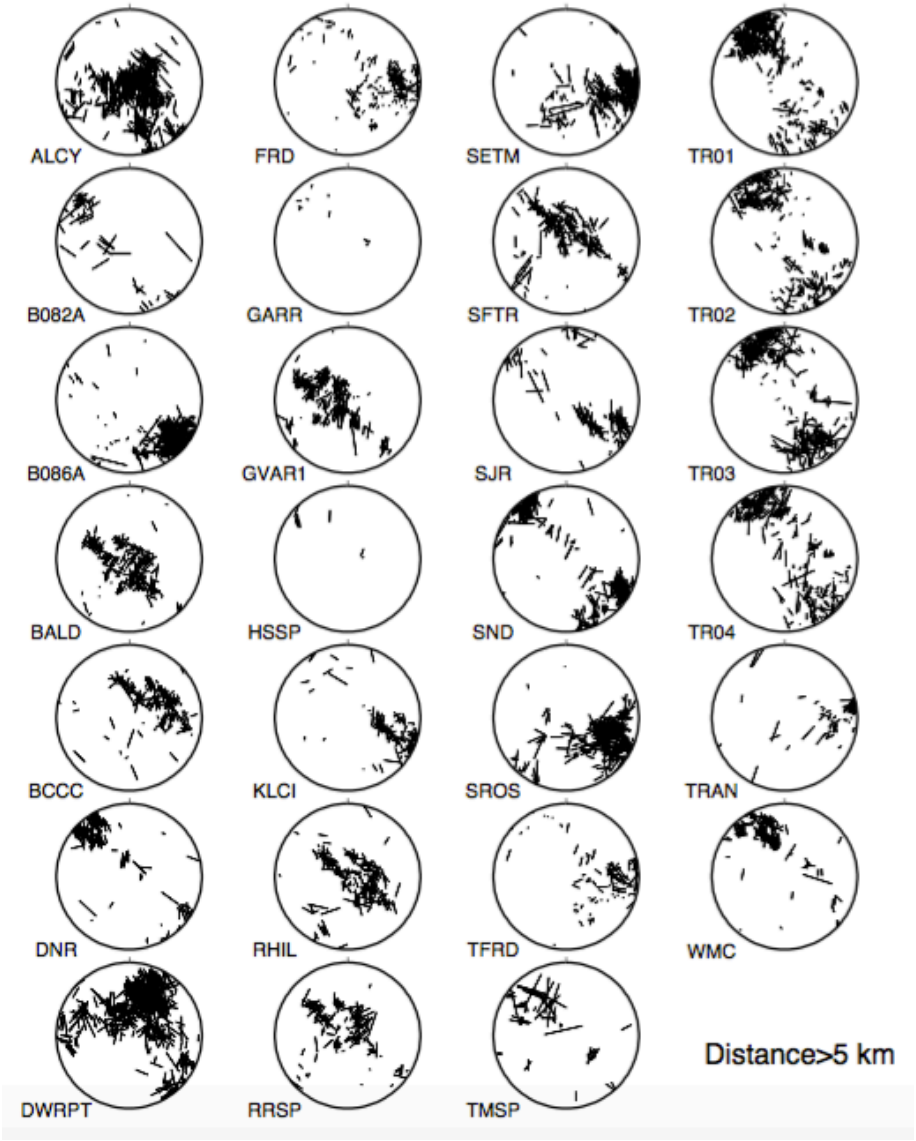

Figure S 2.5 Stereonet projections of SWS measurements on the stations that are 5 km within the main fault. Other symbols are same as Figure S 2.1.

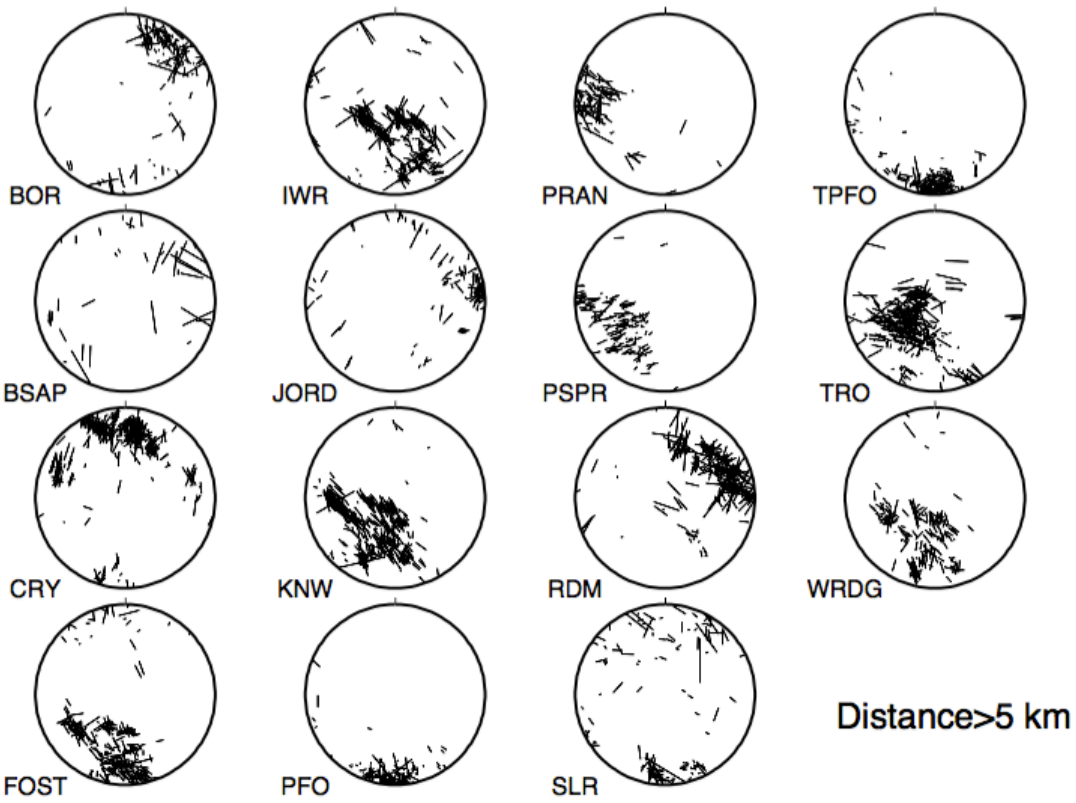

Figure S 2.6 Stereonet projections of SWS measurements on the stations that are more than 5 km from the main fault. Other symbols are same as Figure S 2.1.

2.2 Two Decades of Shear-wave Splitting Measurements in Southern California

Summary

Based on the workflow established in the previous results, I build an automatic system to measure SWS parameters (i.e. fast direction and delay time) using local earthquakes in Southern California from 1995 to 2014. The input data include 330,000 local earthquakes and more than 300 stations, which result in 232,000 SWS measurements that satisfy the initial selection criterion. Measurement quality is then assessed using multiple criteria, resulting in 90,000 high-quality measurements. Compared to previous SWS studies in Southern California, our results provide the most uniform and complete database of local SWS measurements. This database can be used to constrain stress field and investigate structure heterogeneities in this region.

2.2.1 Introduction

Southern California is an important region for SWS studies due to its structural complexity, highly active seismicity and dense seismic instrumentation. Numerous SWS studies have been conducted in southern California at various scales [*Aster et al.*, 1990; *Crampin et al.*, 1990; *Li et al., 1994*; *Paulssen*, 2004; *Boness and Zoback*, 2006; *Yang et al.*, 2011]. These studies used different methods and focused on different stations and time periods, resulting in heterogeneous SWS measurements. This may cause confusions when comparing among different results and inconvenience for further use of these dataset, e.g. input for constraining stress field.

In this paper I present a uniform database of local SWS measurements for Southern California in two-decade period (1995-2014). The measurements are obtained via fully automatic procedure, which include download waveform data, pick phases automatically, and measure SWS parameters. The measurements are then assessed by various objective criteria. I then use the selected high-quality measurements to analyze the spatial and temporal variations of shear-wave anisotropy in southern California. The

results presented in this study can be easily reproduced due to the implementation of automatic procedure and objective selection criteria.

2.2.2 Method and data

The automatic workflow is largely based on the work in the previous section. Basically, I compile several tools into a single system (Figure 2.11), including the Seismogram Transfer Program (STP, developed by Caltech), the PSIR phase picker [*Li and Peng*, 2016a], and the MFAST code [*Savage et al.*, 2010]. The PSIR phase picker uses a "Predict, Search, Invert, and Repeat" procedure. It searches for actual abrupt amplitude changes around predicted theoretical arrivals, in order to improve pick accuracy. Additional details can be found in Li and Peng [2016a] and Section 3.1. Fast directions and delay times are computed using the automated program MFAST [*Savage et al.*, 2010]. This code performs grid-search over the fast direction-delay time (Φ-δt) space to minimize the energy on the component perpendicular to the initial polarization of shear waves.

The input data include 330,000 local earthquakes from 1995 to 2014, which are recorded by the Southern California Seismic Network (SCSN) and relocated by *Hauksson et al.* [2012] (Figure 2.12a). The SCSN consists of more than 300 historical and current stations (Figure 2.12b). I choose the time period of 1995-2014, because before 1995 only a handful of stations had horizontal components. Here I select the events that are within the 45° cone beneath a station (also known as the shear-wave window), i.e. the epicentral distance is less than the event depth, in order to avoid P/S converted phases contaminating direct S phases [Booth and Crampin, 1985; Peng and Ben-Zion, 2004].

The initial measurements then undergo quality control for further analysis. High-quality measurements are defined as: 1) SNR>3; 2) delay time δt < 0.4 s and δt error < 0.1 s; 3) fast direction Φ error <15^o; 4) cluster grade A and B (referring to *Savage et al.* [2010] for definition); 5) 20^o < polarization angle of fast wave against incoming wave <

70°. These criteria are either empirical or inherent from previous studies [e.g., *Peng and Ben-Zion*, 2004; *Savage et al.*, 2010].

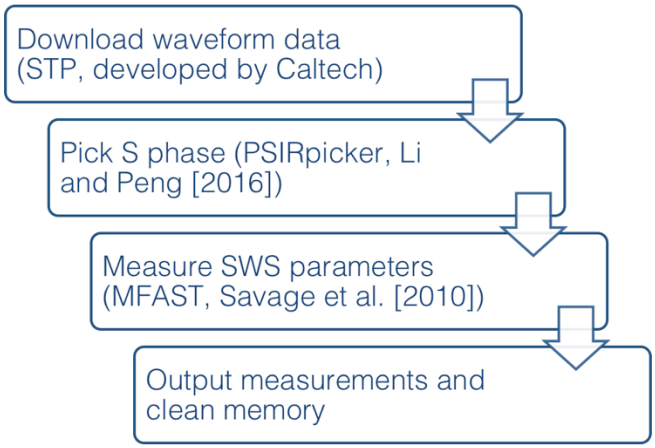

Figure 2.11 Complete flowchart of automatic measurement of SWS parameters.

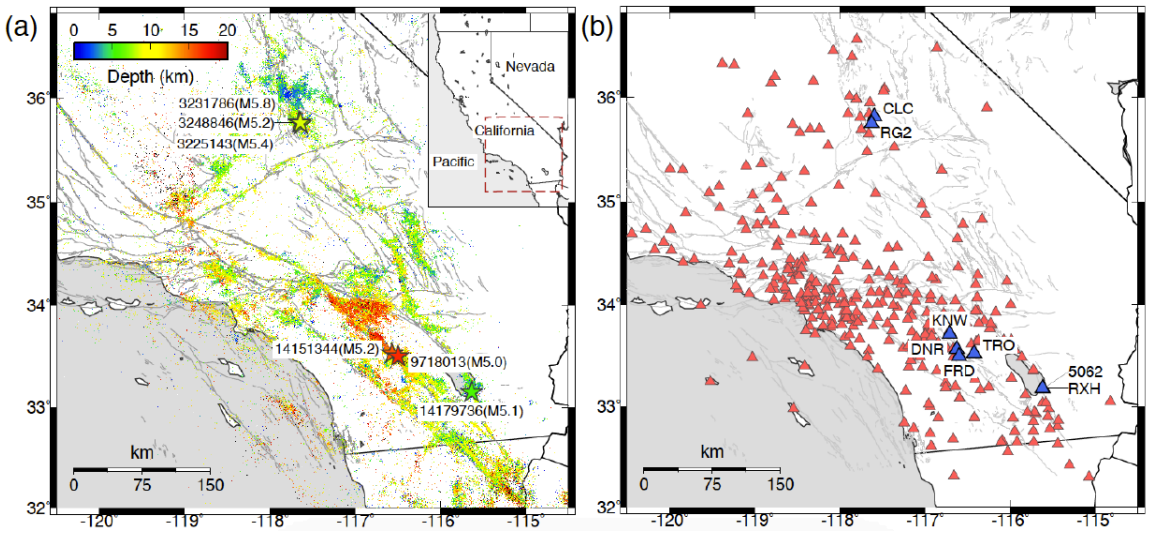

Figure 2.12 Maps of faults, seismicity in southern California and the Southern California Seismic Network (SCSN). (a) Faults are denoted by gray lines. The dots color-coded by depth represent relocated seismicity in 1995-2014 [*Hauksson et al.*, 2012]. The stars mark M>5.0 events closely examined in this study. The dashed red box in the inset marks the study region. (b) The triangles represent the stations of SCSN. The blue triangles with names mark the stations closely examined in this study.

2.2.3 Results and discussion

The results consist of 232,000 SWS measurements. After quality control, 90,000 high quality measurements are obtained. Figure 2.13 shows the very good consistency of measurements on the station KNW over two decades, suggesting the stability of SWS measurement. The patterns also agree very well with previous studies [*Peacock et al.*, 1988; *Crampin et al.*, 1990; *Aster et al.*, 1990; *Yang et al.*, 2011]. However, when some moderate earthquakes occur near a station, the patterns could be interrupted (Figure 2.14). For example, station FRD only 20 km away from KNW has different patterns when M 5 events occurring nearby. In 2001 and 2005, two M 5 events occurred and the SWS parameters at station FRD are different from other time periods. In contrast, the 2011 M 3.1 event near FRD did not change the pattern significantly. This interesting observation could be interpreted in different ways. One possibility is that the 2001 and 2005 M 5 events actually perturbed the stress field and the fracture alignment around FRD, resulting in different SWS parameters. Alternatively, it could be that the seismicity following the 2001 and 2005 events occurred in different regions as compared with the background seismicity, resulting different parts of the crust been sampled. Detailed analysis of spatial seismicity distribution might help to distinguish these two interpretations.

After averaging the measurements on each station, I obtain a spatial map of fast directions (Figure 2.15). As fast directions can be controlled by both stress and structures, the complex patterns could be a result of heterogeneous stress fields and/or pronounced

local structures. However, it could be observed that the overall orientations on most stations are consistent with the quasi-north SHmax direction, which is measured from inverting focal mechanism solutions of earthquakes in this region [*Yang and Hauksson*, 2012]. However, some large geological structures can affect the SWS measurements. For example, the stations near the San Andreas Fault generally have fault-parallel direction, consistent with previous findings [e.g., *Boness and Zoback*, 2006]. By zooming in further to local scale, we can identify finer patterns. The area around the Los Angeles basin, for example, has striking localized patterns in different geological blocks (Figure 2.15b). Along the San Andreas Fault in the NE, the fast directions are mostly along the fault strike. However, the patterns in the SW are divided by the Santa Monica and Raymond Hill faults. The Los Angeles basin in the SE side has general SHmax-parallel fast directions, while in the NW side fast directions are quasi parallel to the San Gabriel fault, which is the NE boundary of the block. Along the Santa Monica and Raymond Hill faults, however, the fast directions are generally along the NE-SW fault trend. These observations show clear evidence that fast directions tend to follow localized terrains and major faults.

Comparison of fast directions to focal-mechanism derived SHmax also shows some localized patterns (Figure 2.16). Generally the fast directions agree with SHmax, especially in the regions around the Los Angeles basin, the Eastern California Shear Zone and the Salton Sea. However, several regimes have notably inconsistent directions between them, from NW to SE including the San Andreas Fault, the Santa Ynez Fault, the block NW to the Los Angeles basin, both sides of the San Jacinto Fault, the southern end of Peninsular Ranges near San Diego. The significant inconsistency in these areas

implies that localized structures are likely primary causes of shear-wave anisotropy. However, the controlling structure types could be different. It is very likely that the fault structures around San Jacinto Fault and Santa Ynes Fault are dominant in controlling anisotropy along them. In comparison, in the other block-shape areas, sedimentary layers or plutonic materials may be possible (but speculative) factors.

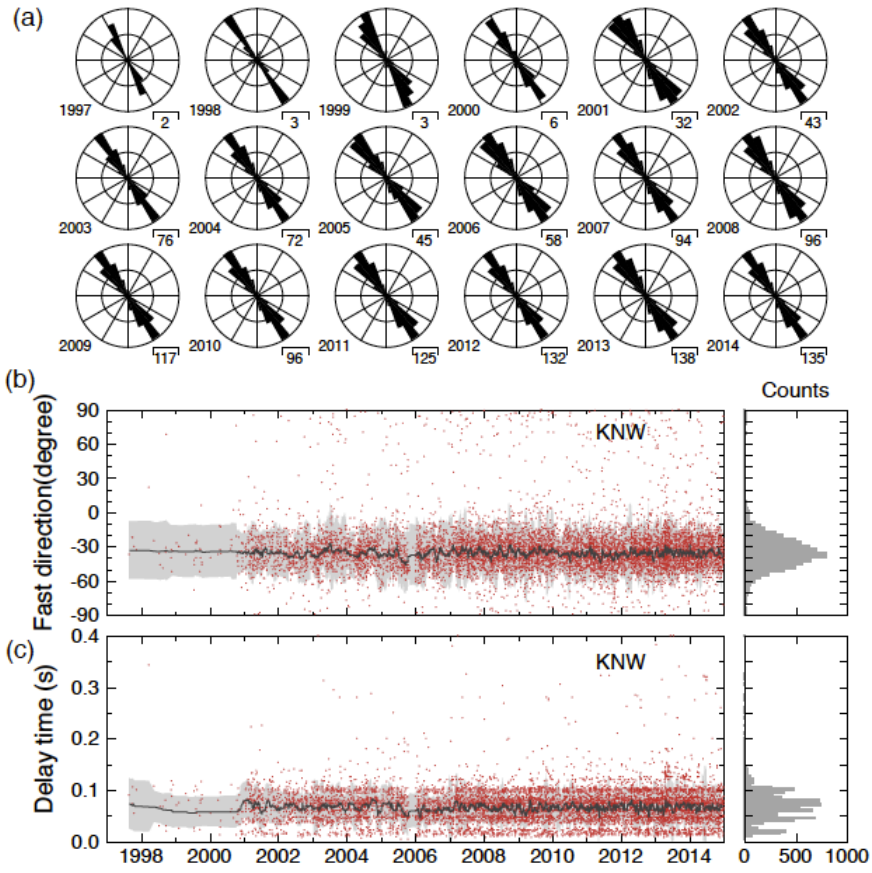

Figure 2.13 Temporal changes of fast directions and delay time in station KNW. (a) Yearly rose diagram of fast directions at KNW from 1997-2014. (b) Fast direction measurements at KNW. The black curve represents the running median for a 50-measurement window. The shaded area marks one standard deviation range. The right panel is a histogram of all the measurements. (c) Delay time measurements at KNW. Symbols are same as those in (b).

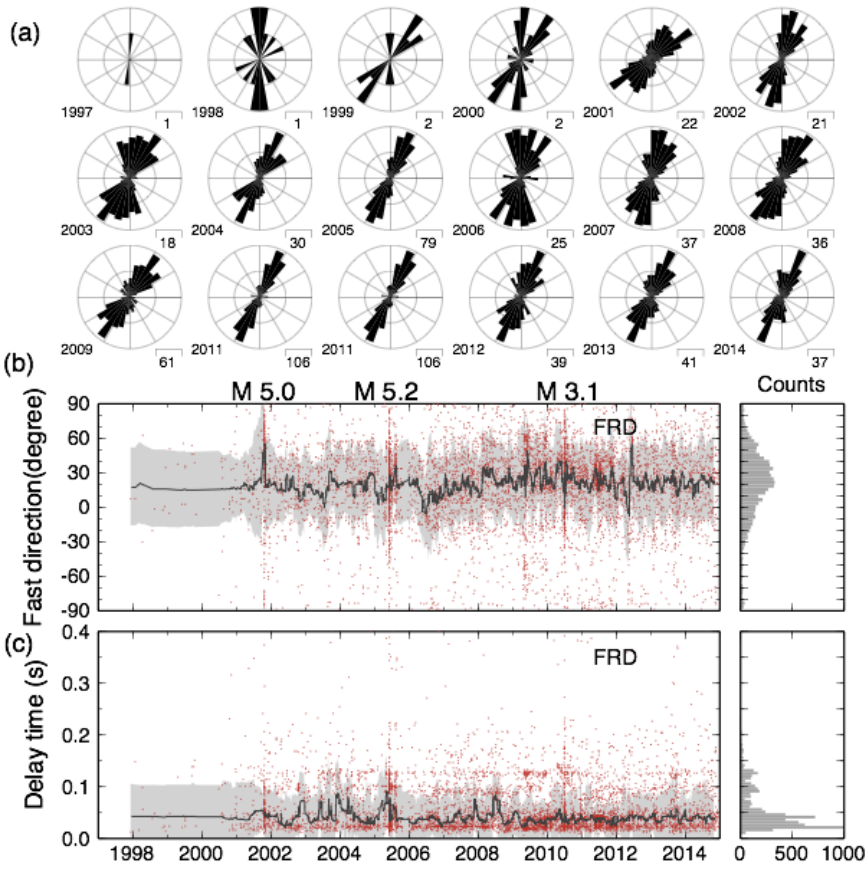

Figure 2.14 Temporal changes of fast directions and delay time in station FRD. Symbols are the same as those in Figure 2.13. Note that the patterns are interrupted with some M~5 events near the stations.

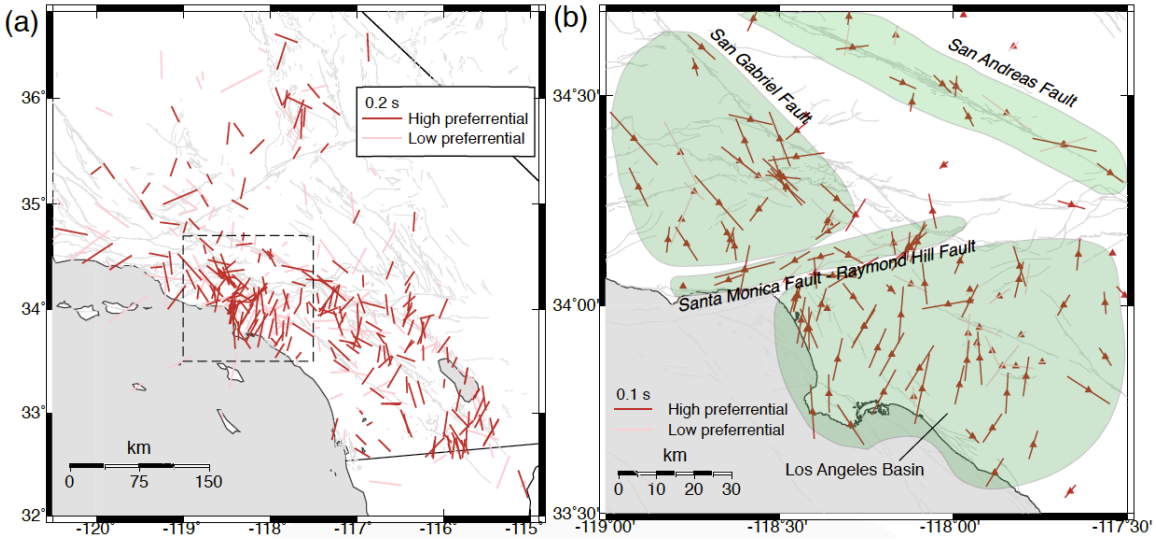

Figure 2.15 Dominant fast directions and average delay times of shear wave splitting in southern California. (a) The bars are oriented along the dominant fast directions and scaled by average delay times on the stations. Red and pink bars denote the stations with highly and low preferential directions, respectively. (b) A zoomed-in map near the Los Angeles Basin as marked by the dashed box in (a). The green shaded areas represent the regimes with similar fast directions. Other symbols are same as those in (a).

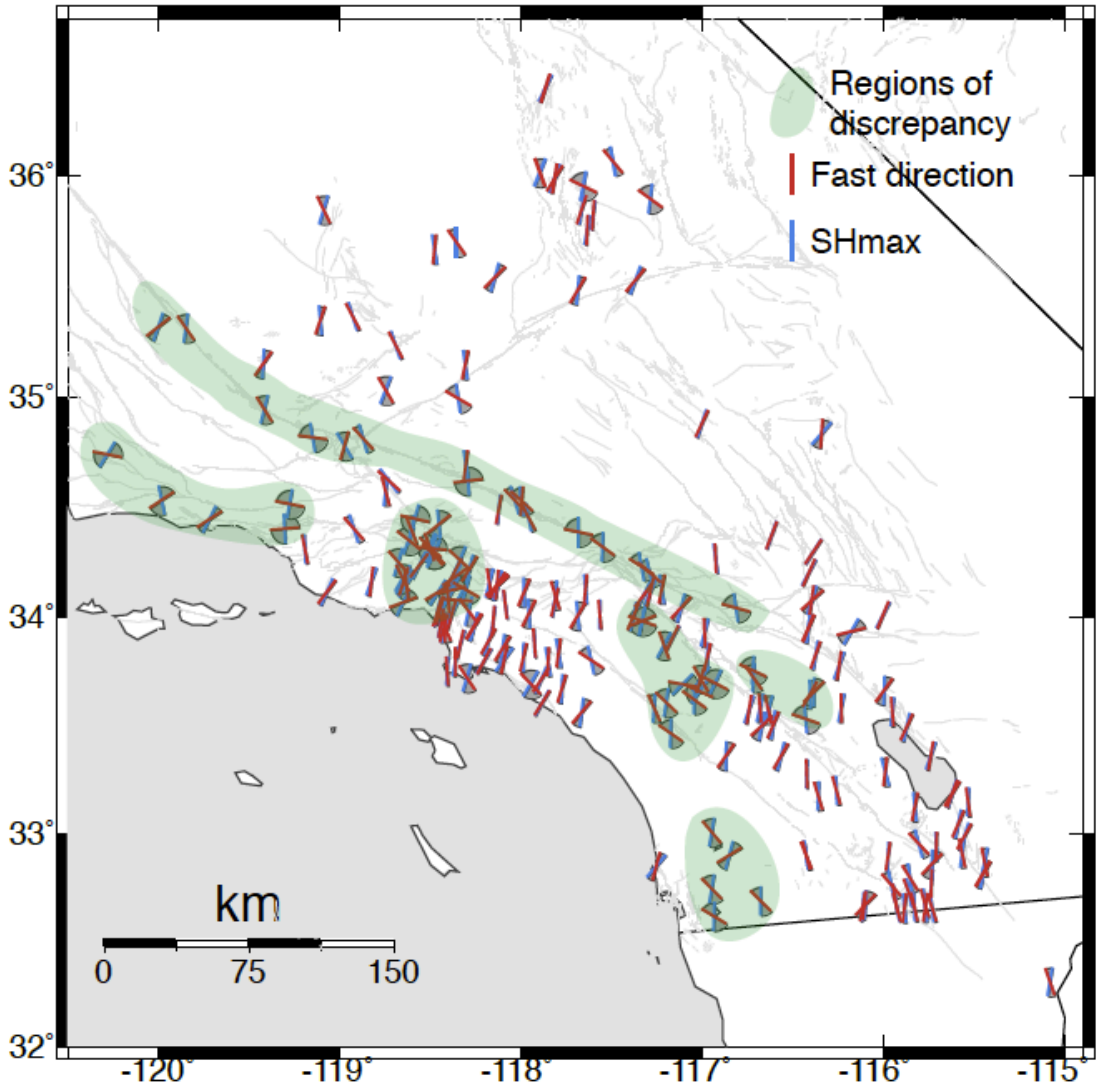

Figure 2.16 Comparison of fast directions (red bars) and maximal horizontal compression stress (SHmax, blue bars). The angle difference between them is shaded with pie shape. Light green areas mark the major areas where fast directions are significantly different from SHmax. SHmax are extracted from focal mechanism analysis by *Yang and Hauksson* [2013].

2.3 Shear-wave Splitting Tomography in the North Anatolian Fault, Western Turkey

Summary

I use a three–dimensional (3D) SWS tomography method developed by *Zhang et al.* [2007] to map the spatial distribution of crustal anisotropy in the Karadere–Düzce branch of the North Anatolian Fault (NAF) in western Turkey. The input data consists of 20751 measurements of the SWS delay times from 7856 aftershocks of the 1999 Mw 7.4 İzmit and Mw 7.1 Düzce earthquakes. The results show a continuous belt–like highly anisotropic zone along the Karadere–Düzce branch of NAF, generally ~3 km wide and down to ~5 km deep. The observed asymmetric pattern of anisotropy along the Karadere segment is qualitatively consistent with asymmetric damages from the unilateral eastward propagation of the Izmit rupture. Another strong anisotropy region was found near the end of the Izmit rupture zone, close to the dipping direction of the fault segment that ruptured during the subsequent Düzce earthquake. These results are generally consistent with the shallow fault–zone anisotropy inferred from previous studies. While the anisotropy generally becomes weaker at depth and/or outside the fault zone, I also identify several highly anisotropic regions as deep as ~10 km, primarily within the Almacik Block. These isolated anisotropy regions could be explained by individual intrusive igneous rock bodies with different mineral alignment. Overall, seismic anisotropy in upper crust of the Karadere–Düzce Branch of the NAF is structurally controlled.

2.3.1 Introduction

Seismic shear waves propagating through anisotropic media are expected to separate into fast and slow components, a phenomenon termed SWS. In the upper crust, shear wave anisotropy is widely observed and usually considered as a result of preferential alignment of fluid−filled cracks in rocks or sediments [*Crampin and Booth*, 1985; *Leary et al.*, 1990; *Crampin*, 1991; *Zhang and Schwartz*, 1994]. In this case, the fast polarization direction is parallel to the maximum horizontal compressive stress direction due to alignment of preexisting cracks in that direction. Other mechanisms are mainly structurally controlled, including preferential mineral alignment, sedimentary bedding planes, and alignments along active fault zones [*Boness and Zoback*, 2006].

Generally two SWS parameters are measured: polarization direction of the fast component and delay time dt between the fast and slow components. While visual inspection was used to measure SWS parameters in many earlier studies [*Crampin*, 1990], automated methods are needed to obtain a large data set of SWS measurements. These include the cross−correlation method [e.g., *Fukao*, 1984; *Liu et al.*, 2003], the covariance matrix (CM) method [e.g., *Silver and Chan* 1991], and the aspect ratio (AR) method [*Shih et al.*, 1989]. To understand spatial distribution of crustal anisotropy, many studies simply average the SWS parameters at each station and superimpose them on the station location [e.g., *Boness and Zoback*, 2006; *Yang et al.*, 2011]. Other recent studies have proposed to plot the average measurements at the earthquake source region [e.g., *Peng and Ben−Zion*, 2004], or somewhere between the source and receivers [e.g., *Liu et al.*, 2008]. When plotting the rose diagrams of fast polarizations on stations, *Eken et al.* [2013] showed that stricter quality criteria can lead to preferred fast polarization more

clearly, which might result from near–station anisotropic bodies. However, in all these cases, the exact location and magnitude of the anisotropy zone along the ray path remains unclear.

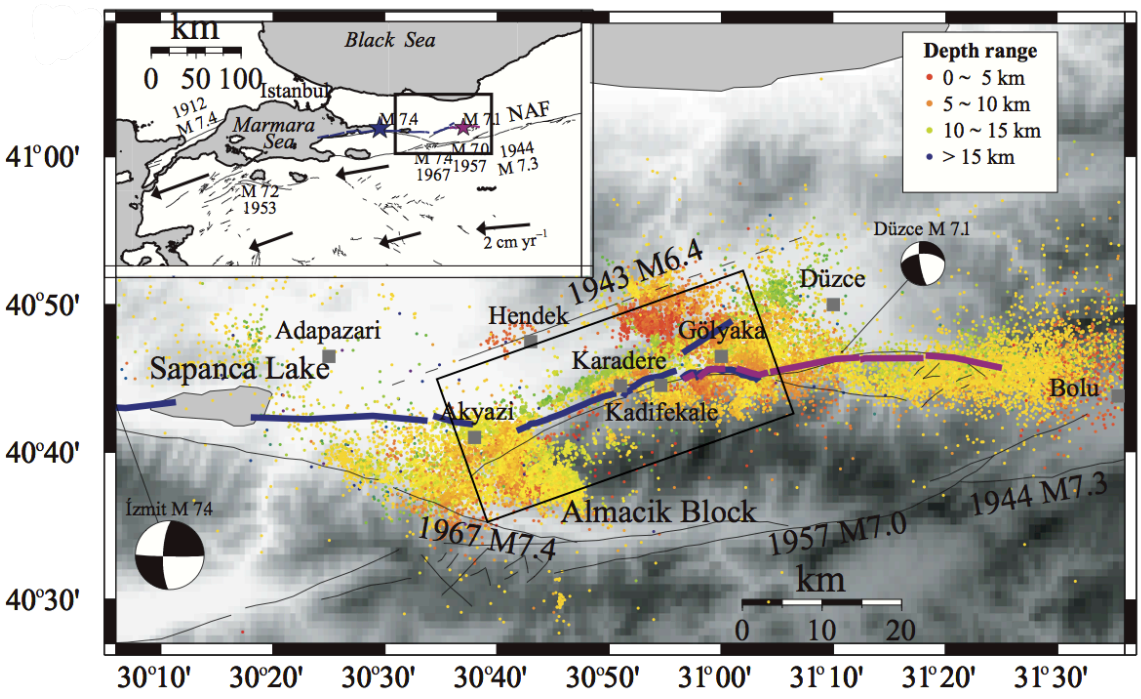

Figure 2.17 Map of study region. Epicentral distribution of ~26000 earthquakes recorded by the PASSCAL seismic experiment along the Karadere–Düzce branch of the NAF. Aftershock locations are marked with colors denoting different depth ranges. The surface ruptures of the Izmit and Düzce earthquakes are indicated with thick blue and purple lines, respectively. The box marks the SWS tomography region. The inset illustrates the tectonic environment in northwestern Turkey.

Various efforts have been made to map the spatial distribution of anisotropy. For example, *Audoine et al.* [2004] developed a method to produce spatial average of splitting parameters by dividing the source–receiver paths into many grid points. More rigorous anisotropy tomography methods have also been proposed to image the spatial distribution of anisotropy [e.g., *Abt and Fisher*, 2008; *Long et al.*, 2008]. However,

complicated waveforms pose difficulties in inversion due to the nonlinear effect of multiple layers of anisotropy [e.g., *Silver and Savage*, 1994]. *Long et al.* [2008] developed a 2.5D SWS intensity tomography method to study upper mantle anisotropy, which calculates sensitivity kernels for heterogeneously anisotropic media. In their method, splitting intensity measured from long period SKS waves, instead of standard splitting delay time and fast polarization, is used to image the anisotropy structure. In comparison, *Abt and Fischer* [2008] imaged 3D anisotropy structure in upper mantle using the SWS parameters by assuming the anisotropy is caused by the lattice−preferred orientation of olivine and orthopyroexene. Partial derivatives of fast polarization and delay time with respect to the orientation of olivine α−axis and anisotropy strength are numerically calculated by modeling splitting parameters for a synthetic wavelet using the Christoffel equation.

Recently, *Zhang et al.* [2007] developed a SWS tomography method to map the spatial distribution of anisotropy in upper crust by back projecting the splitting delay times along ray paths derived from known 1D or 3D velocity models. Comparing with other techniques [e.g., *Long et al.*, 2008; *Abt and Fisher*, 2008], this method does not handle the anisotropic direction in the inversion and the partial derivative of delay time with respect to anisotropy percentage is calculated using ray theory. In this simplified method, all measurements of station−event pairs are utilized in the inversion and weighted by an objective parameter, such as the waveform cross−correlation coefficient between slow and fast shear waves. However, so far it has only been used in the Parkfield section of the San Andreas Fault to map the 3D anisotropy distribution, where 3D velocity models have been well developed [e.g., *Thurber et al.*, 2006].

In this study, I apply the same method to the Karadere–Düzce branch of the North Anatolian Fault (NAF) in northern Turkey. The NAF is the active transform boundary between the Eurasian and the Anatolian Plates. Several earlier studies have found clear crustal anisotropy near the epicentral region of the 1999/08/17 Mw7.4 İzmit earthquake that ruptured the western segment of the NAF [*Crampin and Booth*, 1985; *Evans et al.*, 1985). *Peng and Ben-Zion* [2004] analyzed the SWS parameters in Karadere–Düzce Branch of the NAF ruptured during the İzmit earthquake and the 1999/12/12 Mw 7.1 Düzce earthquake. They found predominant fault–parallel fast directions for stations within a 1 km broad zone around the rupture zones of the two recent earthquakes. *Hurd and Bohnhoff* [2012] used several stations in a larger region around the NAF and found similar results.

In this study, I use the SWS tomography method [*Zhang et al.*, 2007] to map the spatial distribution of anisotropy around the Karadere–Düzce of the NAF, based on the SWS parameters measured by *Peng and Ben–Zion* [2004]. Our results, which will be presented below, are generally consistent with the previous observations, but contain more quantitative information on the along–strike and depth extent of crustal anisotropy in this region.

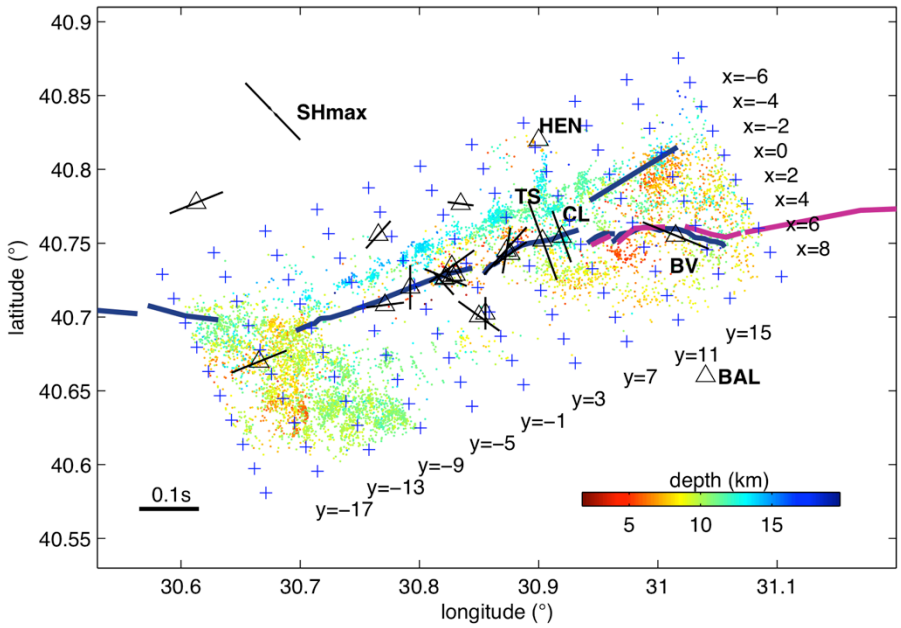

Figure 2.18 Map of the distribution of events (color-coded dots) used in the inversion, stations (triangles), and the inversion grid (crosses). The solid bars over the stations represent the dominant fast axis direction and the average delay time. The surface ruptures of the Izmit and Düzce earthquakes are indicated with thick blue and purple lines, respectively. Background seismicity is the events used in inversion and marked with colors based on the depth. Arrow pair represents the regional maximum horizontal stress direction. Note that station HEN and BAL used by *Hurd and Bohnoff* [2012] are not included in the inversion.

2.3.2 Data selection

I use the SWS measurements from numerous aftershocks recorded by 31 stations (Figure 2.17). Specifically, a temporary 10−station PASSCAL seismic network covered a 6−month period after the İzmit earthquake on Aug 17, 1999. 7 additional stations were deployed for the first 2 weeks after the İzmit mainshock, and another 14−station array was deployed across the Karadere branch of the NAF for the last 2−week period. A total of ~22000 SWS measurements were automatically calculated by a covariance matrix method.

In this study, I focus on the region along the fault strike and in the immediate vicinity of the Karadere segment, which is trending ~70^{o} to the east. The west side of the study region starts from a 5−km−long surface−rupture gap near the town of Akyazi during the İzmit earthquake [*Tibi*, 2001] (Figure 2.17). The Almacik block in the south of the Karadere segment is primarily mafic embedded with andesitic to basaltic rocks and sedimentary sequences [*Yilmaz et al.*, 1997]. To the east end of Karadere segment, the rupture bifurcated during the İzmit earthquake and stopped near the Düzce basin [*Gulen et al.*, 2002] (Figure 2.17). However, the southern strand of the bifurcation partly re−ruptured during the subsequent Düzce earthquake.

Figure 2.18 shows the inversion grid for the SWS tomography and the average SWS parameters at each station (refer to figure 7 of *Peng and Ben−Zion* [2004] for the rose diagram for each station). I choose this region because of its dense event−station coverage. The inversion coordinate system is rotated ~70 degrees clockwise from the north so that the Y−axis is subparallel to the strike of the Karadere segment. The line X = 0 roughly follows the surface trace ruptured during the İzmit earthquake, and the center of the coordinate is at longitude 30.85^{o}E and latitude 40.74^{o}N. 20751 SWS measurements are selected from 7856 events with their ray paths within –21 to 19 km along the Y direction (along−strike) and –8 to 10 km along the X direction (perpendicular to the strike). The majority of the events were distributed at the depth range of 5−10 km (Figure 2.18). The inversion grid nodes in the Z direction are at Z=0, 2.5, 3.5, 6.0, 9.0, and 13.0 km (Table 2.1). In this study I do not apply further selection criteria as *Peng and Ben−Zion* [2004] did. However, I weigh each measurement by the corresponding

cross–correlation coefficient of fast and slow components in inversion in order to reduce the influence of low quality measurements.

Figure 2.18 shows that most fast polarization directions for the stations on or close to the fault are parallel or subparallel to the nearby fault strike. It is interesting to find that the fast polarizations at stations TS and CL are almost perpendicular to the fault strike (Figure 2.18). If the anisotropy is stress–induced and the maximum compressive stress direction is perpendicular to the fault strike, the fast polarization direction is fault perpendicular. However, the direction of the regional maximum horizontal compressive stress is NW–SE [*Bellier et al.*, 1997; *Tadokoro et al.*, 2002; *Görgün et al.*, 2010], which has a large angle against the local fault strike. Therefore, the fault–perpendicular fast polarization anomaly is not due to stress–induced anisotropy. It is likely the existence of anisotropic bodies with preferred mineral alignment could cause the fault–perpendicular polarization. It is noted that the cycle skipping arising from SWS analysis could also cause the fault–perpendicular fast polarization, where the fast and slow components are mismatched by one or more half cycles.

3. Method

The SWS tomography method developed by *Zhang et al.* [2007] is based on two major assumptions. First, it assumes a single–layer anisotropy model that contains vertically oriented microcracks or shear fabric and hence is azimuthal. This is common for crustal anisotropy [*Crampin, et al.*, 1978; *Crampin*, 1987; *Boness and Zoback*, 2006] and also one of the assumptions for the *Silver and Chan* [1991] method, which was used to obtain the measurements in this study. The second assumption is that splitting delay

time is accumulated for each ray segment along the entire ray path [*Fischer et al.*, 2000]. However, the physical meaning of the measured splitting time is still vague when the anisotropy is complicated. In particular, it is not clear whether the measured delay time represents the summation of anisotropy for layers with different fast directions. The previous debate on the ability of using delay times to predict the occurrence of an earthquake also shows the ambiguity of the physical meaning of delay times [e.g., *Aster et al.*, 1990; *Crampin et al.*, 1991; *Aster et al.*, 1991]. However, based on a very simplified model given by the first assumption, the shear wave splits once when entering a single layer of azimuthally anisotropic material, and the delay times between fast and slow shear waves keeps increasing when travelling through the material. In addition, *Silver and Savage* [1994] showed that the *Silver and Chan* [1991] method would produce apparent splitting measurements of the fast polarization and delay time for a two−layer anisotropy model. As a result, the splitting times obtained from this method represent the apparent strength of the anisotropy over the entire ray path. Therefore, it is reasonable to assume that the splitting time is accumulated along the ray path for a relatively simplified model.

Based on the assumptions above, the total observed delay time dt can be expressed as

$$\delta t = \int \frac{K\alpha}{V} dl \qquad (1)$$

where a is the angle between the ray path and the vertical direction, dl is the incremental ray path, and K is the anisotropic strength. The anisotropic strength K is defined as

$$K = \frac{V_{fast} - V_{slow}}{V} \quad (2)$$

where V_{fast} and V_{slow} are the fast and slow S−wave velocities, respectively, and V is the average S−wave velocity.

In the SWS tomography program, regularization methods including damping and smoothing are introduced to stabilize the inversion. Trade−off L−curve analysis is used to search for the appropriate damping and smoothing values that balance minimizing the model variance and data variance (Figure 2.19). I tested 165 pairs of damping and smoothing parameters and determined damping value of 20 and smoothing weight of 1 are suitable for this inversion (Figure 2.19).

I use a simple 1D layered velocity model (Table 2.1; *Seeber et al.*, 2000) to compute the ray paths for inverting the anisotropy model according to Equation 1, although a 3D velocity model around the study region has been recently published [Koulakov et al. 2010]. It is true that by using the simple 1D velocity model, the anisotropy model will be less accurate. However, the main features of the anisotropy model will be similar for both velocity models. This is because the ray paths do not differ significantly, and as a result the linear system according to Equation 1 is also similar. A small change in the velocity will result in a proportional change in the anisotropy percentage. Considering the velocity perturbation between the 1D and 3D models is generally ~5%, the resulting change in the anisotropy percentage is also ~5%. This will have a minimum effect on the overall anisotropy patterns observed later.

Table 2.1 1D velocity model in Karadere-Düzce branch of NAF

Lay Top (km)	0.0	2.5	3.5	6.0	9.0	13.0	30.0
Vp (km/s)	3.443	5.519	5.628	5.906	6.053	6.332	8.000
Vs (km/s)	1.990	3.190	3.253	3.414	3.499	3.660	4.624

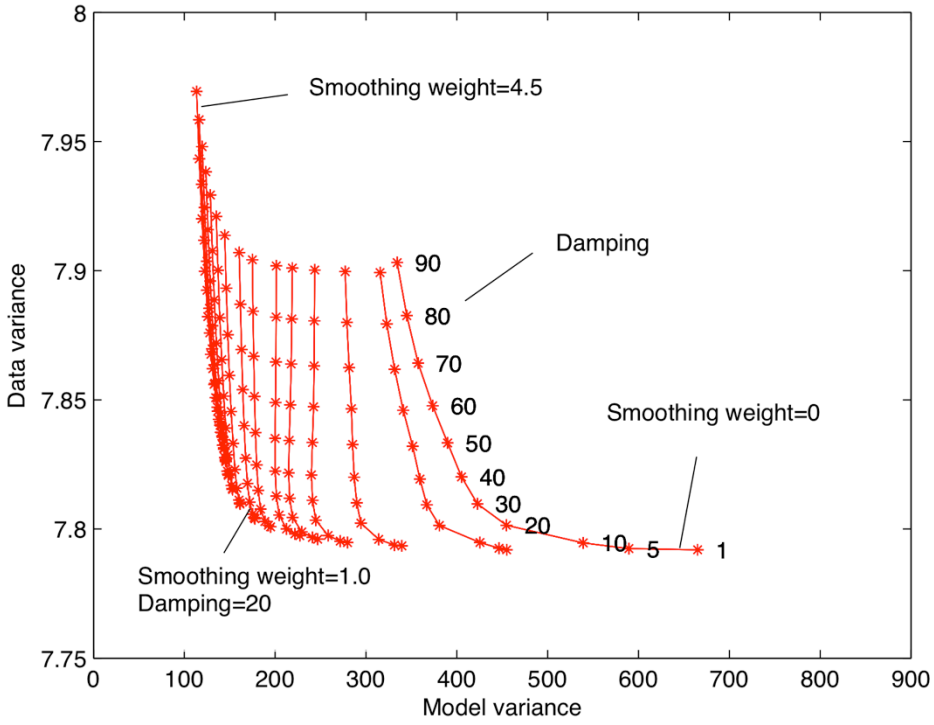

Figure 2.19 L-curves of smoothing and damping parameters. The optimal pair chosen for inversion is smoothing weight=1.0 and damping weight=20.

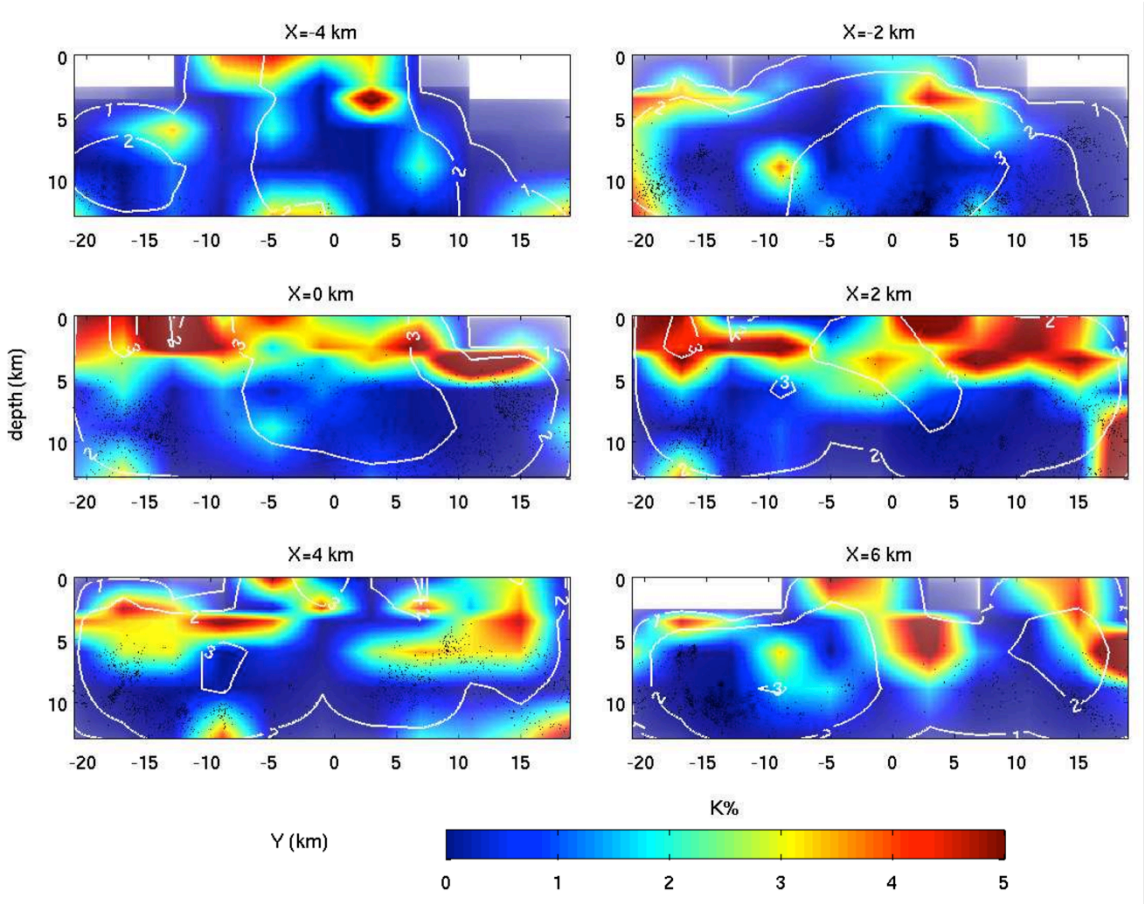

Figure 2.20 Along-fault sections of anisotropy percentage at X=-4, -2, 0, 2, 4 and 6km, respectively. White contours are DWS plotted in a logarithmic-based-10 scale. Black dots are events within half of the grid size of each section. Colors are weighted by DWS values (areas with low DWS are faded and areas with high DWS are stressed). The areas without any ray path (DWS=0) are not sampled and thus whitened.

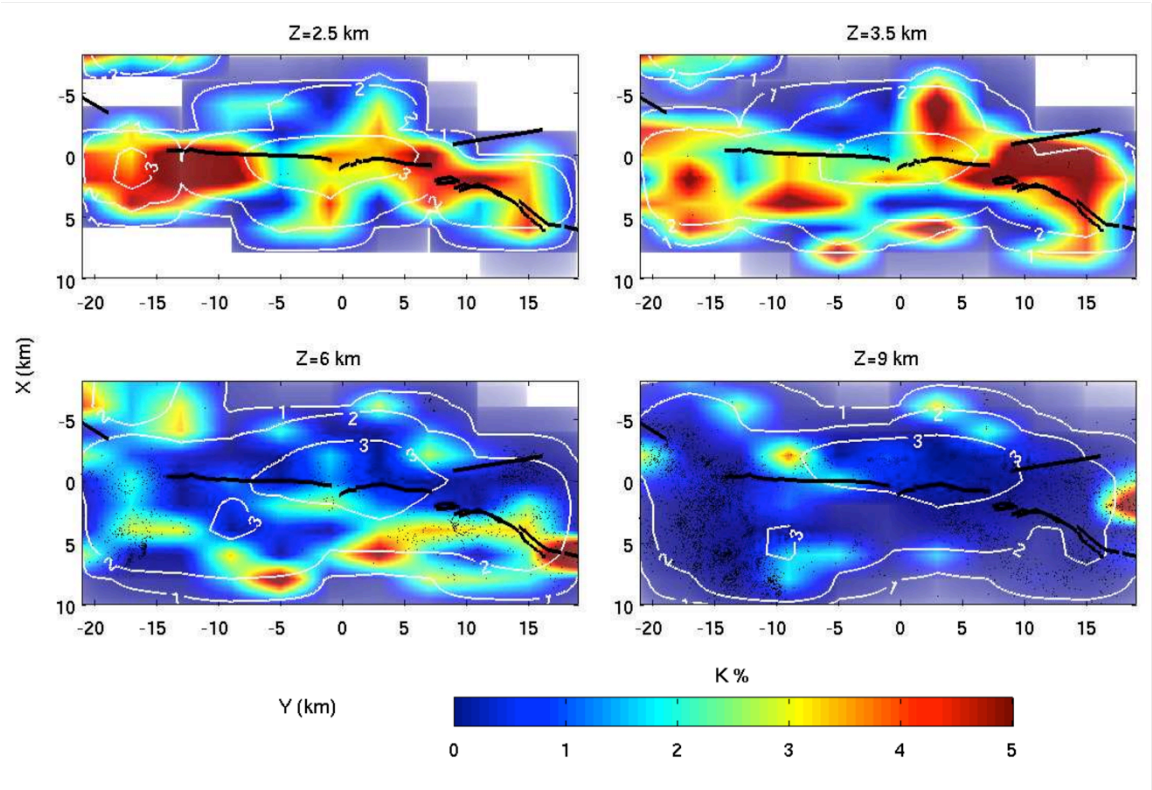

Figure 2.21 Horizontal sections of anisotropy percentage at Z=2.5, 3.5, 6 and 9km, respectively. Black lines are the projected fault surface traces of Karadere and Düzce segments. White contours are DWS plotted in a logarithmic-based-10 scale. Black dots are events within half of the grid size of each section. Colors are weighted by DWS values (areas with low DWS are faded and areas with high DWS are stressed). The areas without any ray path (DWS=0) are not sampled and thus plotted whitened.

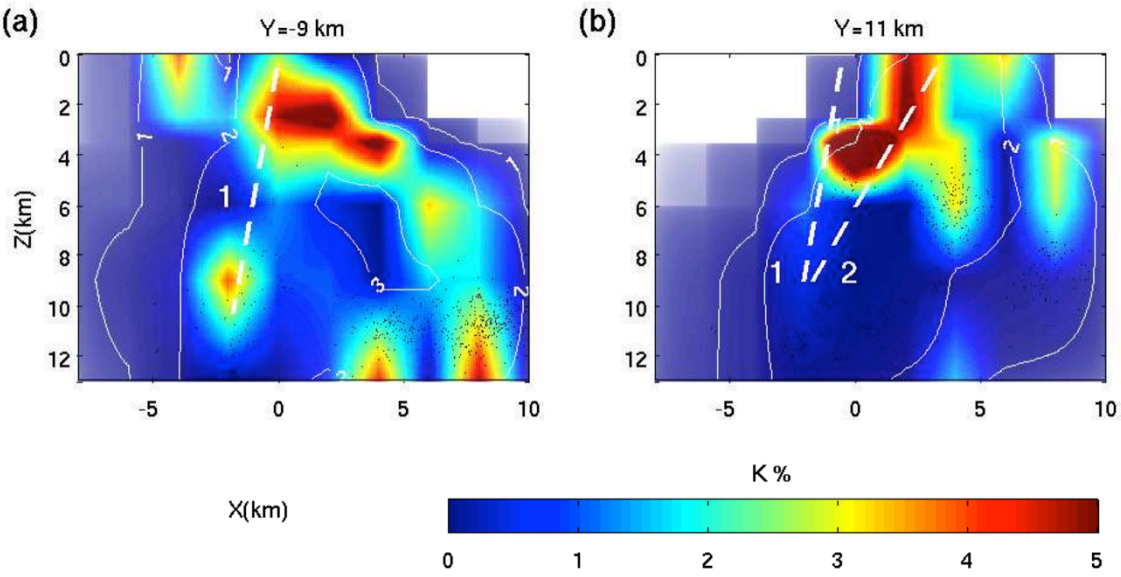

Figure 2.22 Comparison of anisotropy percentage in northeast-trend Karadere segment and near east-trend Düzce segment. (a) The white dash line 1 indicates the rupture dip of Karadere segment. Black dots represent the events within half of grid size at the section. (b) Similar to (a). The white dash line 2 indicates the rupture dip of Düzce segment. Colors are weighted by DWS values (areas with low DWS are faded and areas with high DWS are stressed). The areas without any ray path (DWS=0) are not sampled and thus whitened.

2.3.3 Results

To characterize the resolution capability of the SWS tomography method in this study, I use two ways: the ray path density quantified by the Derivative Weighted Sum (DWS) for each inversion grid node and the checkerboard resolution test. In real applications, ray−sampling density has been routinely used to qualitatively describe if the model is well resolved [e.g., *Haslinger et al.,* 1999] although ray angular coverage information is not considered. DWS is a measure of model sampling, representing the relative density of ray paths weighted by the importance of each ray segment by its

distance to the grid node. In general, the model areas with higher DWS values are better resolved [*Haslinger*, 1999; *Zhang and Thurber*, 2007].

Similar to the checkerboard resolution test used for velocity inversion, I also constructed a checkerboard anisotropy model with anomalies from 0 to 5% (See Figure S 2.7–2.12). The checkerboard resolution test shows the recovery of anomalies in the regions of interest is generally acceptable (e.g., X = 0 ~ X = 2 in the immediate vicinity of the fault). The resolution in the deeper part of the model is higher than in the shallower part because of the better ray coverage, which is also reflected by the distribution of DWS values.

Figures 2.20 and 2.21 show the cross–sections at different X values (along the faults trike) and horizontal slices at different depths of the 3D anisotropy percentage model, respectively. Figure 2.22 shows cross sections of the anisotropy percentage model at Y = -9 km and 11 km, around the center of the Karadere segment and the Düzce segment that ruptured during the İzmit and Düzce earthquakes, respectively. The anisotropy models in Figure 2.20 to 2.22 are shown in a faded color scheme in which the areas with lower DWS values are more faded and the areas with higher DWS values are more highlighted. The areas without ray coverage (DWS=0) are whitened. The areas of interest generally have moderate to high resolution (DWS=10~1000, Figs. 4–6).

In the shallow crust (depth < 5km) of the Karadere–Düzce branch of the NAF, the anisotropy is very strong (as high as 5%) and concentrates around the Karadere fault trace (e.g., X = 0 and X = 2 km). The belt–like anisotropic zone is generally shallower than 5 km, and becomes deeper to the northeast (Y > 10 km), close to the fault segment that was ruptured twice during the İzmit and Düzce earthquakes (Figure 2.20). The anisotropy

zone is mainly shifted to the SE side of the fault trace (X = 0 ~ 5 km) for the SW fault segment (Y = -20 ~ -5 km) (Figure 2.21). Between -5 and 5 km along the Y direction, the anisotropic zone becomes more diffuse, with the highest anisotropy concentrated around the Karadere rupture zone (Figure 2.21). This coincides with anomalous fast polarization directions observed at stations TS and CL between Y = 3 and Y = 7 km [*Peng and Ben-Zion*, 2004], and a minor step over [*Hartleb et al.*, 2002] to the east of the Kadifekale town (at X = 0 and Y = 0 km). However, for the anomalous fault–perpendicular fast polarization, the possibility of cycle skipping cannot be ruled out. It is possible that the real fast polarization is along the fault strike while cycle skipping leads to a 90^{o} ambiguity of fast polarization and one or more half periods increase in delay times. Further to the east (Y = 5 ~ 19 km), the anisotropy zone is mainly centered around the rupture zones of the İzmit and Düzce earthquakes at shallow depths (Slice Z = 2.5 km and Z = 3.5 km of Figure 2.21). Another high anisotropy zone is observed from the surface down to the depth of 6 km to the NW side of the surface rupture zone near station BV (X = 0 km), where the maximum delay times of up to 0.3 s were observed.

At Y = –9 km around the center of the Karadere segment that ruptured during the İzmit earthquake, the anisotropy extends discontinuously from the near surface to the depth around 12 km, with a broken zone around the depth of 5 km (Figure 2.22). Overall, the dipping trend of the anisotropy zone follows closely to the fault dip angle of the Karadere segment, which is approximately 80^{o} to the north [*Ben–Zion et al.*, 2003; *Bulut et al.*, 2007]. However, the strongest anisotropy is localized within the Almacik block to the SE side of the fault, which is also shown in Figure 2.20. At Y = 11 km around the western end of the segment that ruptured during the Düzce earthquake, the anisotropy

greater than 5% is mainly concentrated from 3 to 7 km in depth and between the extension of the Karadere segment and the Düzce segment that ruptured twice (Figure 2.22). The anisotropy zone dips about 50^{o} to the north, close to the dipping angle ($50-70^{o}$ to the north) of the Düzce mainshock rupture and its aftershocks [*Burgmann et al.*, 2002]. The coincidence of anisotropic zones with fault geometries indicates that they are strongly structure–related.

In addition to these strong anisotropy anomalies around active rupture zones at shallow depths, I also observe pockets of isolated anisotropy anomalies at greater depths away from the faults. They are generally at the dimension of kilometers in radius and have comparable anisotropy percentage with the belt–like anisotropic zone in the fault zone.

2.3.4 Discussion

Peng and Ben–Zion [2004] only selected events that are within the shear–wave window (i.e., the epicentral distance less than the depth) for measuring their SWS parameters. If the subsurface velocity structure is uniform, this corresponds to an incidence angle of 45^{o}. However, because of the lower velocity near the surface, the rays tend to be more vertical as the ray approaches to the surface. For the anisotropy tomography in this study, as the velocity tomography, it also relies on the crossing rays to image the anisotropy structure. As a result, the model resolution in the shallower depths is relatively worse, as shown in the checkerboard resolution test in supplementary materials.

Nevertheless, due to the dense distribution of earthquakes and thus good ray coverage in our study area, we were able to determine the 3D anisotropy distribution around the Karadere–Düzce branch of the North Anatolian Fault with a reasonable resolution. In summary, we found that the anisotropy is primarily distributed in a continuous belt–like zone down to 3–5 km in depth and of 1–3 km wide along the Karadere–Düzce segment of the NAF. In the deeper region and away from the faults, the anisotropy shows isolated blocks but with comparable anisotropy percentage. The distinct anisotropy features in and outside the fault zones provide a unique opportunity to understand the anisotropy mechanisms in the upper crust of the study region.

Because of the relative movement of blocks on both sides of the fault, it generally causes the shear fabric or microfractures that are preferentially aligned parallel to fault zones. Such a preferential alignment would result in fault–parallel fast polarization. In addition, the belt–like anisotropic zone generally follows the surface fault trace (Figure 2.20), which strongly indicates a structure–controlled mechanism of crustal anisotropy in this region.

We note that the rotation of maximum horizontal compression near the fault may introduce some potential bias when using fast polarization to infer anisotropy mechanisms. For example, *Holt et al.* [2013] used the aftershock data of the Darfield earthquake to invert regional stress field in New Zealand. They found that the maximum horizontal compression rotated to be parallel to the Darfield fault, where fault–parallel fast polarizations were observed for some on–fault stations [*Syracuse et al.*, 2012]. However, this rotation has not been observed for the 1999 Izmit earthquake [*Görgün et al.,* 2010].

The width of anisotropy zone is confined within 3 km near the fault interface, which is much wider than the 100–300 m of low–velocity damage zone inferred from fault zone trapped waves [e.g., *Ben–Zion et al.*, 2003; *Peng et al.*, 2003; *Li et al.*, 2006]. It is quite possible that fault zone trapped waves required a coherent low–velocity zone that only exists in the immediate vicinity of the fault interface, while fault–zone related fractures could exist at much further distances. We also note that previous studies of fault zone trapped waves were primarily based on seismic data collected by dense fault zone arrays with a typical length of a few hundred meters. Hence, it is possible that a much wider damage zone exists, but was not detected by a relatively short array. Indeed, using a 5–km long dense array, *Cochran et al.* [2009] found a 1.5 km–wide damage zone along the Calico fault in the eastern California shear zone.

It is interesting to note that the anisotropic zone on the Karadere segment is asymmetric rather than centered with respect to the fault trace (Figures 2.21 and 2.22). The damage zone is ~3 km wide and localized to the south of the fault surface trace, while the Karadere segment is dipping approximately 80 degrees to the north [*Ben-Zion et al.*, 2003]. Such asymmetric localization of the damage zone may result from varying intensity of hydrothermal conditions and/or rock properties of both walls [*Sibson*, 2003]. Alternatively, an asymmetric damage zone is expected for dynamic ruptures propagating along a fault interface that separates different elastic media [*Ben–Zion and Shi*, 2005]. Such ruptures would propagate preferably in the direction of slip on the slower side of the fault, and produce tensile radiations and damages on the faster side of the fault [*Ben–Zion*, 2001; *Shi and Ben–Zion*, 2006; *Bulut* et al., 2012]. The Almacik block in the SE side of the fault has a higher velocity than the sedimentary basin on the other side, at

least in the top few kilometers [*Koulakov et al.*, 2010]. Such assumption is qualitatively consistent with the eastward propagation (slip direction of the slow side) of the İzmit rupture along the Karadere segment, and additional fractures and anisotropy in the faster Almacik block.

However, the pattern becomes much more complicated to the east of the town of Kadifekale, where the rupture bifurcated and finally stopped near Golyaka during the İzmit earthquake (Figures 2.17 and 2.21). 87 days after the İzmit earthquake, the November Düzce earthquake re−ruptured part of northeastern section of the Karadere segment, and the remaining segment to the city of Bulu. Such an unusual rupture process indicates strong complexity of rock properties and heterogeneity of stress field. For example, *Hurd and Bohnhoff* [2012] showed a bimodal pattern of fast polarization directions at station HEN located toward the eastern part of the İzmit rupture and close to the Karadere fault (X = −6 km and Y = 7 km), which is close to the fault−zone anisotropy body imaged in this study. Further to the east near the Düzce basin, our results indicate that the anisotropic zone might be controlled by both the Karadere segment and the Düzce segment (Figure 2.22b). *Görgün et al.* [2010] showed that the Düzce fault that bounds the Düzce Basin may represent a major asperity which was activated by the east end of İzmit rupture but not ruptured until three months later. Although the stress imparted from the İzmit rupture to the Düzce fault was complicated, the asperity that was ruptured afterwards may induce additional damage and hence contribute to the high anisotropy between two segments.

The continuous anisotropic zone is generally 3−5 km deep, which is compatible with the results implied from the distribution pattern of the delay times and event locations

[*Peng and Ben–Zion*, 2004; *Hurd and Bohnhoff*, 2012]. This is also the typical depth extent of anisotropy reported in other fault zones [e.g., Zhang and Schwartz, 1994; *Liu et al.*, 2004]. Because the cracks are expected to close and/or reduce in density due to the increase of confining pressure with depth, we would expect to observe a reduction of anisotropy with depth. It is also reported that the fault zone might change at 3 km depth from a mechanically passive zone in the shallow part to an earthquake prone zone in the deeper part [*Dieterich* 1979; *Marone and Scholz*,1988; *Blanpied et al*., 1991]. However, we note that the anisotropy belt extends as deep as 8 km in the northeast (Figure 2.22b), where the fault correspondently ruptured both during the İzmit and Düzce earthquakes. Coincidently, this region also shows the highest anisotropy in our study area, consistent with the finding that station BV recorded one of the largest delay times. Maximum afterslip was also observed in this region from GPS data after the İzmit and before the Düzce earthquake [*Burgmann et al.*, 2002]. Therefore, the fault that had been ruptured by both earthquakes may get additional damages at greater depths, resulting in stronger anisotropy.

Away from the fault, the anisotropy is generally smaller and decreases to 0–1% in the shallow part. However, in the deeper part (> ~ 4 km), there are several strong but isolated anisotropic blocks embedded in the weak anisotropic background. For example, in the Almacik block there are several highly anisotropic blocks located at the depth of 6–10 km in the immediate vicinity of the aftershock zone. This is consistent with the inference by Hurd and Bohnhoff (2012) that the anisotropy beneath the station BAL (Figure 2.18) located near the center of the Almacik block may lie close to the source region instead of right beneath the station. Note that the SWS observations on station BAL are not

included in our study, thus providing an independent support of our tomography results. As found previously, extrusive igneous and sedimentary rocks are embedded in the mafic Almacik block [*Yalmiz et al.*, 1997]. Therefore we suggest that these isolated anisotropic blocks outside the fault zone are likely due to local lithology. The candidate mechanisms for the highly anisotropic bodies outside the fault zone include the preferential aligned minerals in igneous rocks, foliation and/or saturation of fluids in sedimentary rocks. If seismic anisotropy outside the fault zone is due to stress–controlled fractures, the fast polarization direction is expected to align with the direction of maximum compressive stress. However, previous studies show fast polarization directions outside the fault zone vary with stations and some of them are neither parallel to the maximum compressive stress direction or along the fault strike. Therefore, these isolated anisotropic anomalies are more likely caused by individual igneous rock bodies with different minerals alignment directions.

2.3.5 Conclusion

I applied the 3D SWS tomography method to image the upper crustal anisotropy in the Karadere–Düzce branch of the NAF. The tomography benefited from the large dataset that sampled the study area with high coverage. The results show strong spatial heterogeneity of anisotropy on and outside the fault zone. A continuous belt–like highly anisotropic zone is identified along the fault, generally ~3 km wide and down to ~5 km, which is generally consistent with previous studies on shallow crust anisotropy in either the NAF or San Andreas Fault [e.g., *Ben–Zion et al.*, 2003; *Zhang et al.*, 2007]. The observed asymmetric pattern of anisotropy along the Karadere segment is qualitatively

consistent with asymmetric damages from the unilateral eastward propagation of the Izmit rupture. The strongest anisotropy zone in the study region is coincident with the segment ruptured twice during the İzmit and Düzce earthquakes. These results, together with fault–parallel fast polarization directions around the fault, strongly support the mechanism of the structure–controlled anisotropy due to aligned fabric related to fault damage zone. In the deeper part of the fault zone, anisotropy generally becomes very weak because of the closure of fractures, as a result of fault healing and increased confining stress with depth. However, in the deeper part outside the fault zone we found several highly anisotropic bodies in form of isolated blocks that are embedded in the low anisotropy background. Our results explain the inconsistent fast shear–wave polarization directions varying with stations outside the fault zone that was found in previous studies. The isolated anisotropy blocks outside the fault zone could be explained by individual intrusive igneous rock bodies with different mineral alignments. In summary, seismic anisotropy in upper crust of the Karadere–Düzce Branch of the North Anatolian Fault is structurally controlled.

2.3.6 Checkerboard tests

Here I present the checkerboard resolution test results for the ansiotropic models. First I construct a checkerboard anisotropy model with anomalies from 0 to 5% (Figures S 2.7, S 2.9, and S 2.11). The sizes of anomalies are the same as the grid intervals used in the inversion. Second, the synthetic delay times between the fast and slow shear waves were computed based on Equation 2 in the main text using the same event-station distribution in the inversion. Third, the obtained synthetic delay times were used for the

SWS tomography and the recovered checkerboard patterns are shown in Figures S 2.8, S 2.10, and S 2.12.

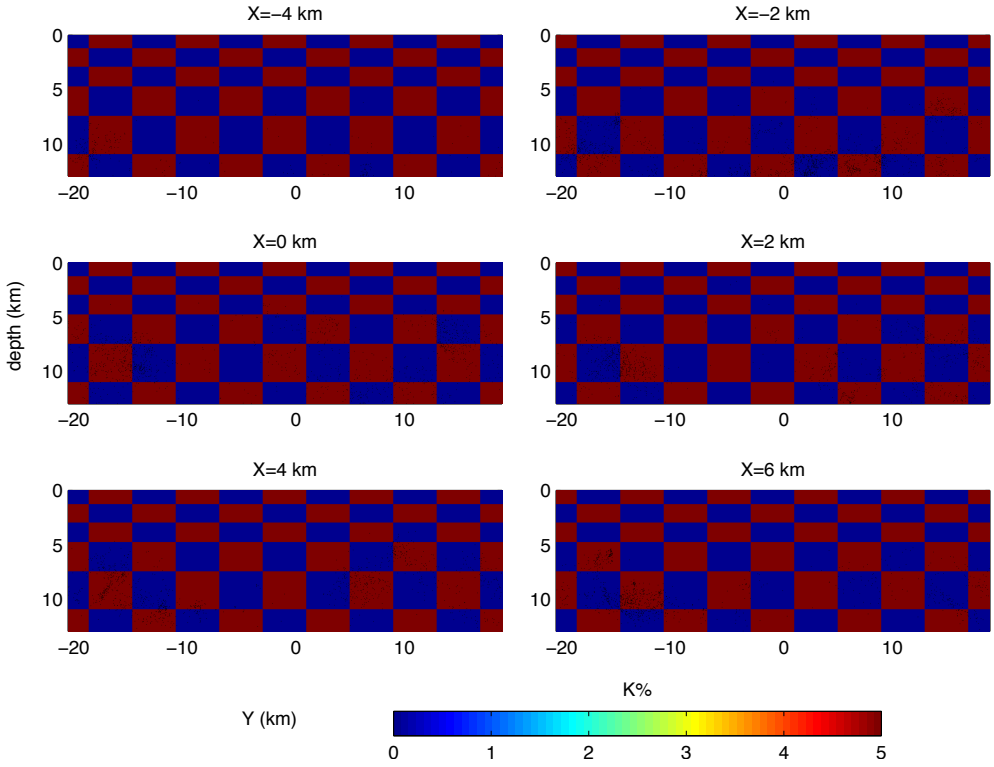

Figure S 2.7 Along-fault sections of synthetic anisotropy anomalies at X=-4, -2, 0, 2, 4 and 6km, respectively. Black dots are events within half of the grid size of each section.

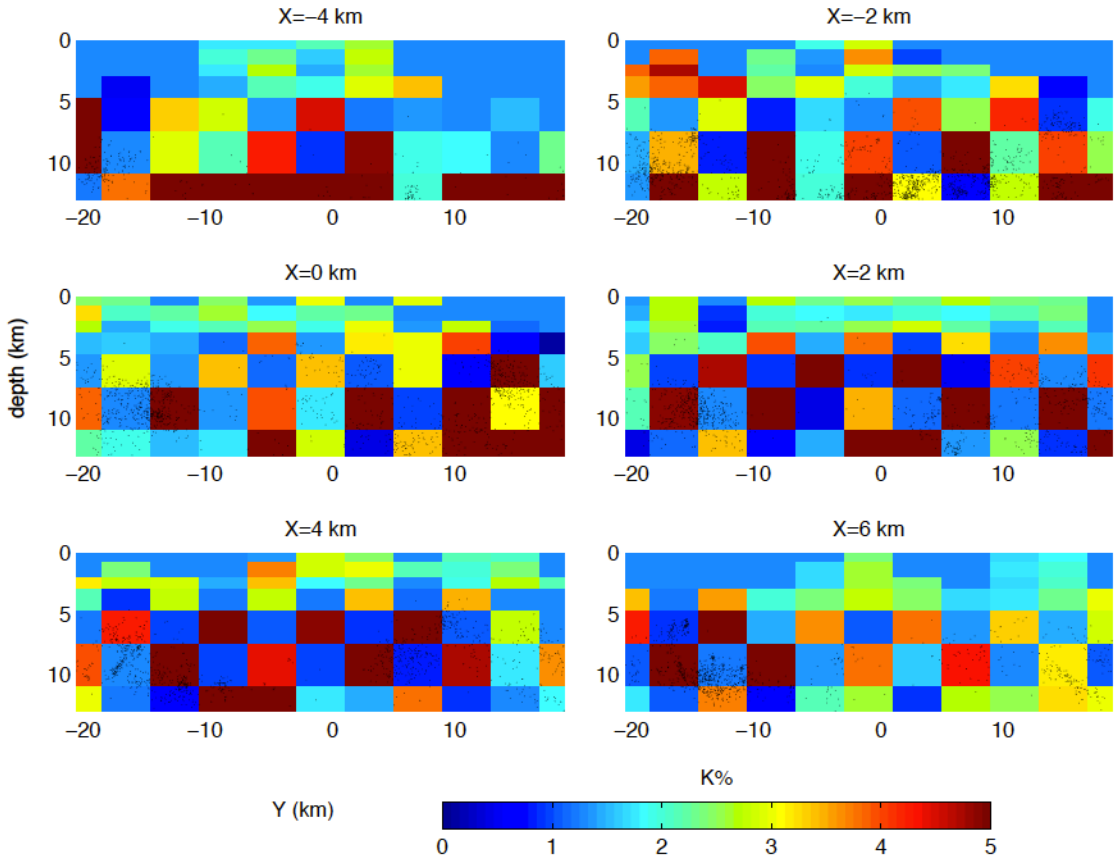

Figure S 2.8 Along-fault sections of inverted anisotropy percentage at X=-4, -2, 0, 2, 4 and 6km, respectively. White contours are DWS plotted in a logarithmic-based-10 scale. Black dots are events within half of the grid size of each section. Colors are weighted by DWS values (areas with low DWS are faded and areas with high DWS are stressed). The areas without any ray path (DWS=0) are not sampled and thus whitened.

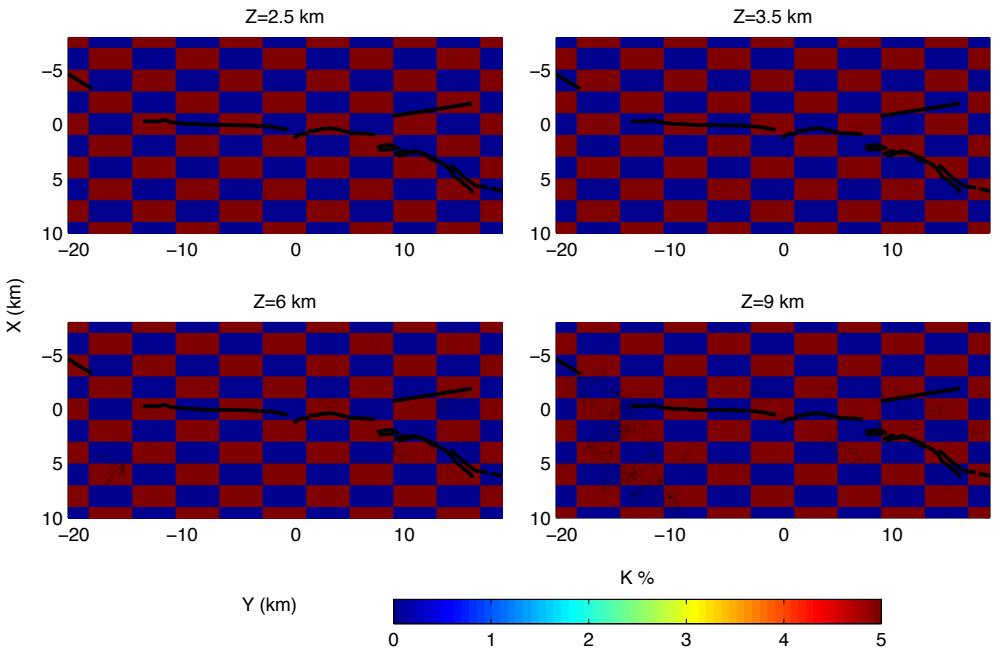

Figure S 2.9 Horizontal sections of synthetic anisotropy anomalies at Z=2.5, 3.5, 6 and 9km, respectively. Black think lines are the projected surface fault trace of Karadere and Düzce segments.

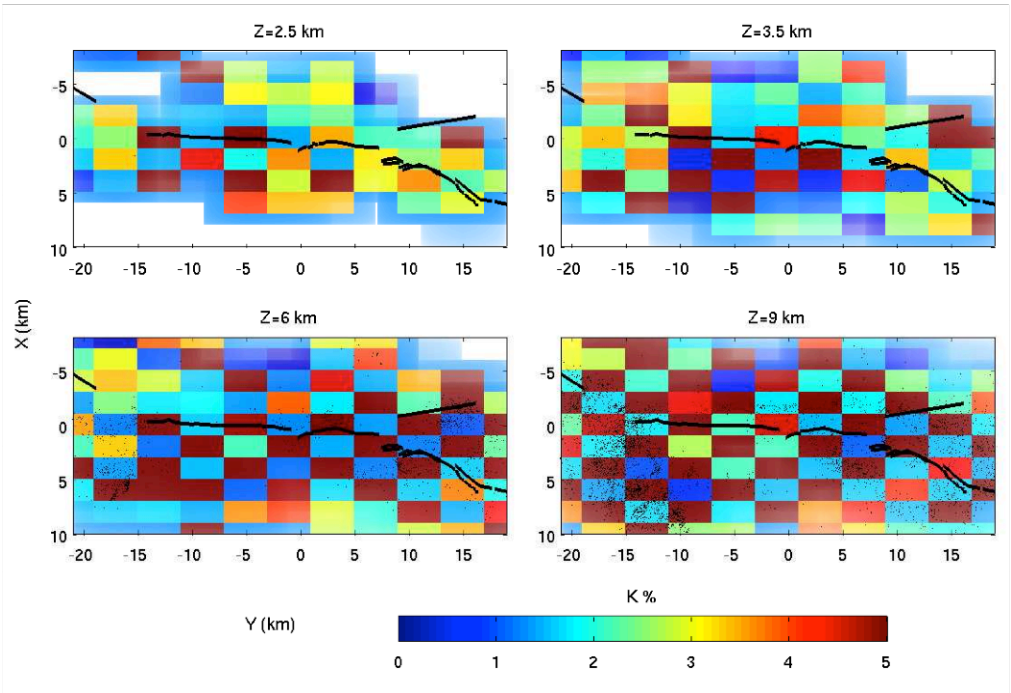

Figure S 2.10 Horizontal sections of inverted anisotropy percentage at Z=2.5, 3.5, 6 and 9km, respectively. Black think lines are the projected surface fault trace of Karadere and Düzce segments. White contours are DWS plotted in a logarithmic-based-10 scale. Black dots are events within half of the grid size of each section. Colors are weighted by DWS values (areas with low DWS are faded and areas with high DWS are stressed). The areas without any ray path (DWS=0) are not sampled and thus plotted whitened.

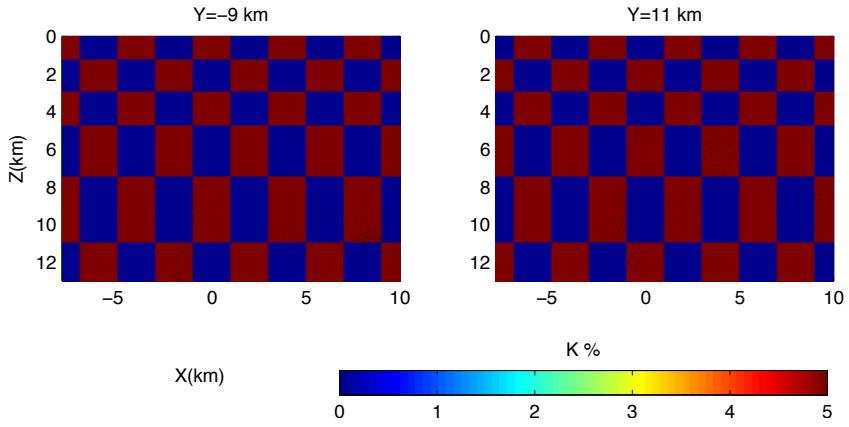

Figure S 2.11 Synthetic anisotropy anomalies at Y = -9 km and 11 km, corresponding to Figure 2.22 in the main text.

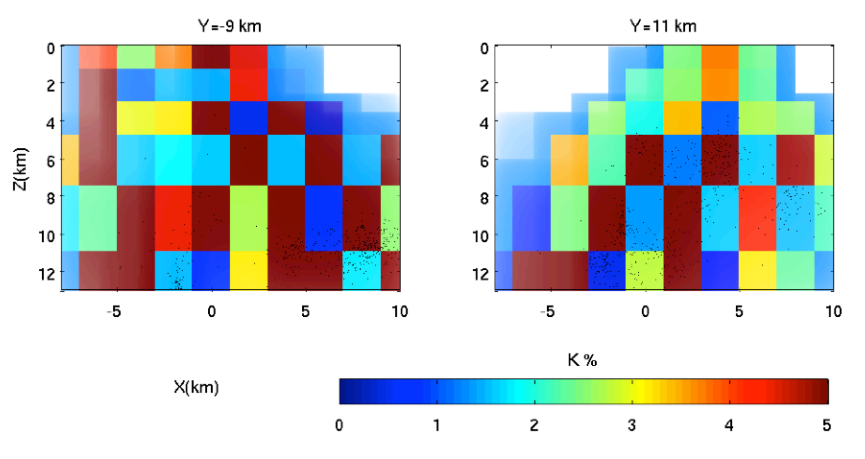

Figure S 2.12 Inverted anisotropy percentage at Y = -9 km and 11 km, corresponding to Figure 2.22 in the main text. Colors are weighted by DWS values (areas with low DWS are faded and areas with high DWS are stressed). The areas without any ray path (DWS=0) are not sampled and thus whitened.

CHAPTER 3. AUTOMATIC PICKING OF PRIMARY, SECONDARY AND FAULT ZONE HEAD WAVES

The results presented in this chapter are from *Li and Peng* [2016a, 2016b].

3.1 An Automatic Phase Picker for Local Earthquakes with Predetermined Locations: Combining An Energy Ratio Detector with 1D Velocity Model Inversion

Summary

I present a simple method to pick additional P and S phases for local earthquakes with predetermined locations. Different from conventional characteristic function techniques, our method incorporates 1D velocity inversion into phase picking. It first predicts phase arrivals using initial velocity models and available event locations, and then applies a detector function to search genuine phase arrivals around the initial predictions. Using the newest searched phase arrivals (picks), the velocity models are updated accordingly and then used to predict more accurate arrival times. Such a procedure can be iterated multiple times, during which both phase picking and velocity model are improved. I perform a test with synthetic data from a 1D velocity. The resulting phase picks are consistent with true arrivals and true velocity models can be well recovered. Another test with real data recorded by the Anza seismic network in southern California shows that the resulting velocity models agree with the average Southern California Earthquake Center (SCEC) community models in this region. Out of

23,932 event-station pairs, 23,770 P picks and 21,935 S picks are obtained from this method. After 4 iterations, 90% of our P picks and 80% of our S picks have differences within 0.15 s, from the phase picks of the Southern California Earthquake catalog. Given its simplicity and efficiency to produce robust P and S picks and 1D velocity models, the technique is particularly suitable for a wide range of seismological research where phase picks at additional stations and/or a refined 1D velocity models are needed.

3.1.1 Introduction

Automatic phase picking is a long-standing topic in observational seismology [e.g. *Allen*, 1982]. Accurate identification of seismic phase arrival times is of particular importance for determining event location and subsurface velocity structure. Although phase identification can be done manually, it is rather time consuming and subjective. As seismic data volume increases dramatically, many automatic phase picking algorithms and characteristic functions have been developed in the past few decades. Beginning with the short-term average/long term average (STA/LTA) method [*Allen*, 1978, 1982; *Earle and Shearer*, 1994], a few higher order statistical metrics have been proposed, including envelope functions [e.g., *Baer and Kradolfer*, 1987], skewness and kurtosis functions [e.g., *Saragiotis et al.*, 2002; *Kuperkoch et al.*, 2010; *Baillard et al.*, 2014]. Algorithms from the data mining community are also introduced for phase picking purpose, such as neural networks [*Dai and MacBeth*, 1997; *Zhao and Takano*, 1999; *Gentili and Michelini*, 2006], autoregressive methods [*Takanami and Kitagawa*, 1993; *Sleeman and Eck*, 1999; *Leonard and Kennett*, 1999; *Zhang et al.*, 2003], and nearest neighbors [*Rawles and Thurber*, 2015]. Some studies combine these approaches to improve the robustness of the picking procedure [*Sleeman and van Eck*, 1999; *Pantane et al.*, 2003;

Diehl et al., 2009; *Ross and Ben-Zion*, 2014]. These methods are designed to identify sharp changes in waveform amplitudes without a priori information of seismic events. Therefore, they are essential at initial stages of seismic data processing, i.e., building earthquake catalogs.

However, in some seismological studies we may encounter a different situation: start with event catalogs in hand (generally from network centers or government agencies responsible for reporting earthquakes) but without phase arrival information at certain stations. One example is seismic travel-time tomography [e.g., *Aki and Lee*, 1976], which is widely used to image the Earth's three-dimensional seismic velocity structures. Another example is using waveform template matching technique to search missing events from standard catalogs, which requires phase arrivals to select proper windows for waveform correlation [e.g., *Peng and Zhao*, 2009]. These studies mainly use earthquakes as listed in published catalogs and require reliable measurements of seismic phase arrival times for certain stations or networks. Even for the stations in which phase picks are routinely provided, certain phases, such as S picks, are usually not complete. On the other hand, with event locations in hand, simply using 1D or 3D velocity models to predict theoretical phase arrivals may not be satisfactory [e.g., *Peng and Zhao*, 2009], because of inaccurate velocity models. Another common way is to use characteristic functions, such as the aforementioned STA/LTA function, to pick phase arrivals. However, using characteristic functions alone may not be the optimal choice. For example, the performance of characteristic functions tends to decrease in presence of high-amplitude local noise or seismic phases other than the targeted phases. For this reason, characteristic

functions usually lead to low production of S picks, which are generally contaminated by P wave coda and P/S converted phases.

Here we show that additional information from event catalogs may be exploited to enhance picking accuracy. A simple algorithm is introduced to combine characteristic function search for phase arrivals and velocity model prediction, in an iterative sense. This method ensures that a detector function is applied within a time window allowed by initial velocity models, thereby avoiding erroneous picks clearly outside typical P and S windows. It also updates the velocity models and makes more accurate prediction of phase arrivals in the next iteration. The resulting velocity models derived in this way can be used for other research purposes, such as earthquake location and tomography. I test this method with both synthetic and real data sets and demonstrate its capability to produce reliable phase picks and improved 1D velocity models.

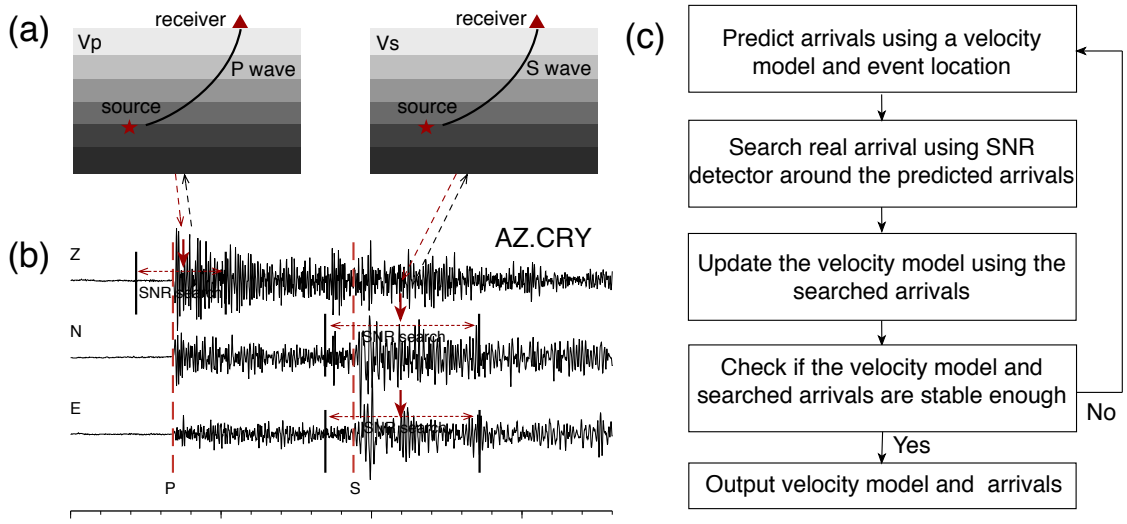

Figure 3.1 Schematic diagram and flowchart for the 'Predict-Search-Invert-Repeat' (PSIR) procedure. (a) 1D velocity models, source (star) and receiver (triangle) locations, and ray paths for P and S waves. (b) An example three-component seismogram recorded at station CRY in the Anza seismic network. Vertical dashed lines mark the P and S arrivals. Vertical arrows mark the predicted arrivals. Dashed arrows denote window ranges for searching the real P and S arrivals. Dashed arrows linking two parts suggest that the velocity model can predict arrivals

and in return can be updated by the searched picks. (c) The detailed flowchart of the PSIR procedure.

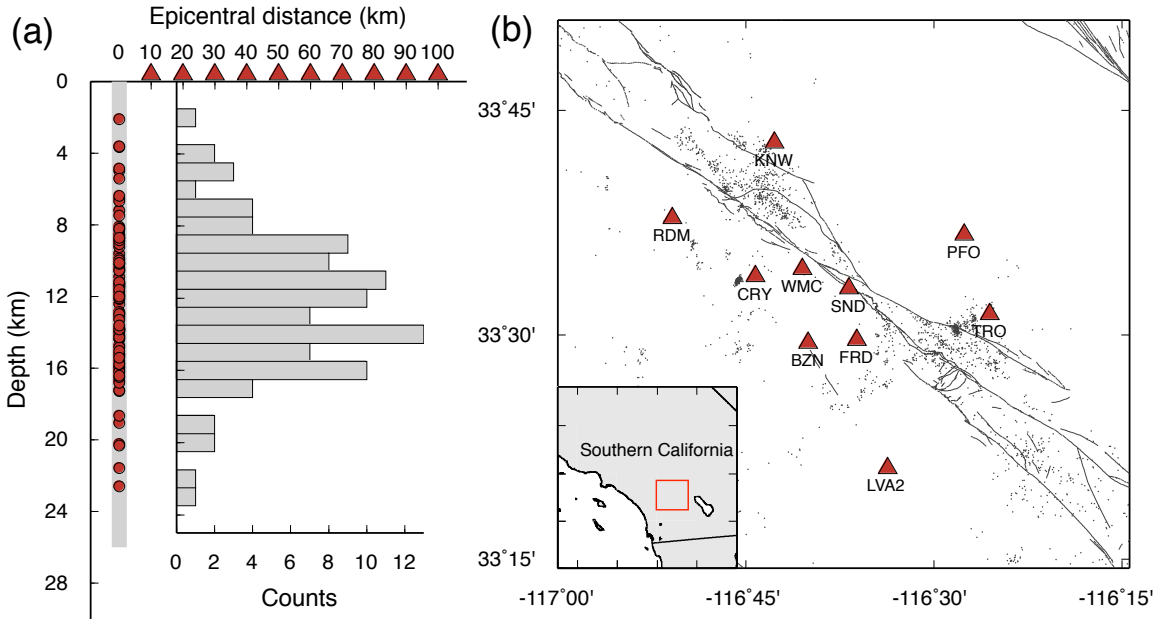

Figure 3.2 The synthetic test setup. Red triangles represent 10 surface receivers from 10 km to 100 km with 10 km spacing. Red circles represent 100 events with depths following a pseudo-Gaussian distribution and truncated at the edges of 0 and 25 km. The histogram shows the counts of events in 1 km bins in depth. (b) Map of the San Jacinto Fault zone in southern California. Red triangles represent stations in the Anza seismic network used in the test. Background seismicity is between 01/01/2014 and 06/01/2014 from the Southern California Seismic Network (SCSN) catalog. The red rectangle in the inset marks the study region in a larger map of southern California.

3.1.2 Method

Figure 3.1 shows the schematic diagram and flowchart of the method. As mentioned before, I first take event locations from a given event catalog and a preliminary velocity model as inputs. Next, given the location of an event and the preliminary velocity model, the phase arrivals are predicted at several stations. I then apply a standard forward-backward energy ratio (FBER) detector to search the actual arrival within a window around the predicted arrival. The searched picks are used as input to the velocity model inversion. The updated velocity model is used to predict

theoretical arrivals again, and thus the entire procedure can be iterated. The use of velocity models ensures that the detector function is applied within a reasonable time window, and in return the newly identified picks improve the velocity model. The above process is repeated until the picks and the velocity model become stable, which usually takes no more than three iterations. The method is essentially a joint search for the picks and the velocity model based on predetermined event locations. I term this procedure as "Predict-Search-Invert-Repeat" (PSIR) and the details of each step are described below.

The travel time calculation follows the code in the frequency-wavenumber synthetic seismogram package developed by *Zhu and Rivera* [2002], which computes the ray parameter by a shooting method. To determine the window for searching the real phase arrival, we assume that actual velocity deviates within a percentage of the velocity model

$$\epsilon = \Delta V_{max}/V \tag{3}$$

where V is a given velocity model, and ΔV_{max} is the maximal allowed difference between the true velocity structure and the given velocity model. We note that ϵ is an average perturbation of the whole velocity model, but in reality, the velocity perturbation may vary within each layer. The parameter ϵ can be preset by users, based on a rough estimate of the accuracy of the given velocity model. By propagating the velocity perturbation to arrival time perturbation, the search time window becomes

$$[t_O + \frac{t_T}{1+\epsilon}, \qquad t_O + \frac{t_T}{1-\epsilon}] \tag{4}$$

where t_O is the event origin time, and t_T is the theoretical travel time. It is worth noting that this search window may not include all true arrivals, due to underestimation of the inaccuracy of the velocity model and/or lateral heterogeneity, which is usually the case for some initial velocity models. However, as long as actual arrivals falling within the search window are sufficient for stable inversion of the velocity model, the inverted velocity model should shift toward the true one. More importantly, based on the updated velocity model, the predicted arrival and the search window are revised to be more accurate and the number of successful picks should increase in the next iteration.

To search the true picks within the window, we use the following FBER function:

$$\mathrm{FBER(t)} = \frac{\int_{\mathrm{t}}^{\mathrm{t+T}} A^2(\tau)\mathrm{d}\tau}{\int_{\mathrm{t-T}}^{\mathrm{t}} A^2(\tau)\mathrm{d}\tau}, \qquad t_O + \frac{t_T}{1+\epsilon} \leq t \leq t_O + \frac{t_T}{1-\epsilon} \tag{5}$$

where *A* is the seismic waveform amplitude and *T* is the predefined window length for SNR calculation. The true phase arrival is simply picked at the maximum of the FBER function in the window, which is different from conventional characteristic function pickers that widely use preset trigger thresholds. Note that because the maximum within a window always exists, a pick is always identified. Hence, it is important to use FBER value to control the pick quality. A pick would be discarded when the maximum is found at the window edge. This is to avoid flat/monotonously increasing/decreasing amplitude, or other erroneous data artifacts within the window. Other exceptions, such as incomplete waveform header information or missing data points, could also result in picking failure.

After obtaining arrivals from the FBER picker, we update the velocity model via 1D velocity inversion, which is a common technique in seismology. Here I follow *Shearer* [2009] to formulate the problem:

$$\delta t_i = \sum_j t_{ij} \epsilon_j \tag{6}$$

where i denotes the i^{th} travel time measurement, and j denotes the j^{th} layer. Therefore, δt_i is the residual between the i^{th} searched arrival and the i^{th} predicted arrival, t_{ij} is the travel time in the j^{th} layer of the i^{th}measurement, and ϵ_j is the fraction of velocity perturbation in the j^{th} layer. This is a linear equation and is typically ill posed, so I use zero-order Tikhonov regularization to solve it [*Aster et al.*, 2013]. The regularization parameter is chosen to be 10 for our test cases, but is available for change at users' choice.

In our procedure, P phase is picked on the vertical component, and the FBER measured at the pick is used as a quality metric. S phase can be picked on east and north horizontal components separately, and the final S pick is their FBER-weighted average. As the event location is available, alternatively, the S pick could be made simply on the transverse component. The later approach is not elaborated here, but included as a separate version in the downloadable package. Only the picks with high enough FBER are used in the velocity inversion (in the following tests I define the threshold to be FBER>5). The algorithm allows users to set the velocity perturbation ϵ, based on their evaluation of the initial velocity model accuracy. However, if ϵ is set too large, for example, $\epsilon > 0.27$ for $V_P/V_s = \sqrt{3}$, the search window for P wave overlaps with the one for S wave. If overlap does occur, the algorithm automatically sets the start of the S

window to be after the searched P arrival. Users can also set the window length *T* for FBER calculation, according to the sampling rate and noise level of a specific data set. Typically a large *T* is more noise-robust, but it is less sensitive to localized amplitude change. By default, the algorithm uses 0.1 s and 0.2 s for P and S waves, respectively.

3.1.3 Test with synthetic data

In the test, I use the frequency-wavenumber synthetic seismogram package [*Zhu and Rivera*, 2002] to compute synthetic waveforms. The setting includes 10 receivers at the surface and 100 events at depth (Figure 3.2a). The epicenters of the 100 events are placed at X=0 km, while their depths follow a pseudo Gaussian distribution with mean at 12.5 km and truncated at the edges of 0 and 25 km. The 10 receivers are located at X=10, 20, … 90, 100 km. The focal mechanism parameters (i.e., strike, dip and rake) of these events are randomly set with even chance in the parameter's allowable ranges. P and S phases are searched on vertical and horizontal components, respectively.

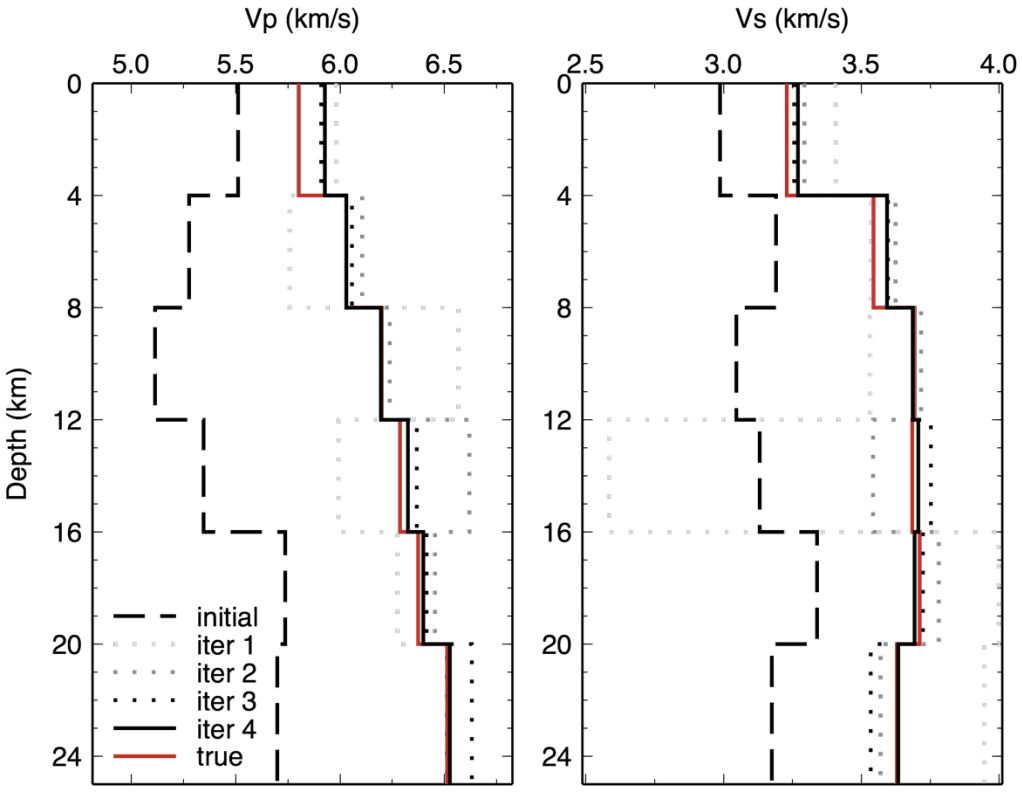

Figure 3.3 1D P and S velocity models in the synthetic test. Dashed and solid red lines represent initial and true models, respectively. The light gray, moderate gray, and dark gray dotted lines represent the inverted velocity models in the 1st, 2nd, and 3rd iteration, respectively. The solid black line is the resulting velocity model in the 4th iteration.

Using the Southern California Earthquake Center (SCEC) community velocity model [*Magistrale et al.*, 1996], I extract the velocity profiles at the locations of ten stations in the Anza seismic network (Figure 3.2b). These ten velocity profiles are then averaged into a 1D model with each layer of 4-km thickness (red lines in Figure 3.3), which is used for synthetic seismogram generation. Next, I apply 5%-20% random velocity perturbation in each layer of the true model, in order to obtain a perturbed velocity model serving as the starting model for the test (dashed lines in Figure 3.3).

While the actual maximum velocity perturbation could reach up to 20%, I set the maximum allowed perturbation $\epsilon = 15\%$ for all iterations. In the synthetic test, I perform four iterations. The resulting P and S velocity models converge well to true velocity models, with the relative inaccuracy about 1% or less in each layer (Figure 3.3). Figure 3.4a and 3.4b show the difference of the searched picks relative to the predicted arrivals based on the initial velocity models (iteration 1) and updated models (iterations 2-4). It is clear that the discrepancy between the searched picks and predicted arrivals narrows down during four iterations. Because the initial models are significantly slower than the true models, the travel time residuals are clustered at the negative sides. Although some of the picks cannot be searched because the preset maximum perturbation is less than the actual maximum perturbation, many picks within the 15% range can be still obtained. These picks are then used to update the velocity models, which help in reducing differences between the predicted arrivals and the true arrivals in the later iterations.

After four iterations, the searched picks are very consistent with the prediction from the updated velocity models (iteration 4 in Figure 3.4a and 3.4b). Figure 3.4c and 3.4d show the residuals between the searched picks and the true arrivals. In the first iteration, because the velocity inaccuracy is underestimated, a number of arrivals are excluded in the search range and thus cannot be obtained. However, as shown in Figure 3.4c and 3.4d, after the first iteration of velocity update, the number of successful picks increases significantly (P picks increase from 821 to 1,000, and S picks increase from 749 to 1,000). From iterations 2 to 4, the residual histograms do not change much. This is because after the first iteration, the velocity models converge within 15% perturbation of the true velocity models, thus most picks can be searched using the preset 15% threshold.

Figure 3.5 shows a few automatic pick examples in comparison to true arrivals. To check for the performance for noisy data, I also add zero-mean Gaussian noise with standard deviation at 20% and 50% of first arrival peak amplitude. Although there is a decrease in successful picks and greater error in the inverted velocity model, as the noise increases, the results generally agree with the true arrivals and velocity models.

3.1.4 Test with real data

I test the method using six months of seismic data recorded by the Anza seismic network in southern California (Figure 3.2a). The data set consists of 2,815 events recorded by 10 stations, resulting in 23,932 event-receiver pairs. I download the event catalog, waveforms, and phase picks from the Southern California Earthquake Data Center (SCEDC). I use the same starting velocity s as the ones in the synthetic test (Figure 3.3). Similarly, the maximum allowed velocity perturbation ϵ is set as 15%. Although the exact velocity structure in the region is not known, I use the average SCEC community velocity model as a reference for the test output.

Table 3.1 Number of Picks in the real data test

	iter 1	iter 2	iter 3	iter 4	Pick rate
P (FBER>1)	21002	23385	23784	23770	99.3%
P (FBER>5)	18207	22091	22516	22516	94.1%
P (FBER>10)	14843	19193	19643	19638	82.1%
S (FBER>1)	16785	21936	21938	21935	91.7%
S (FBER>5)	15218	21490	21498	21494	89.8%

S (FBER>10)	13274	19499	19519	19522	81.6%

I perform four iterations and check the pick and velocity model changes (Figure 3.6). Although with some minor differences, the resulting velocity models in the iterations are generally consistent with the average SCEC models, indicating the SCEC models agree well with those derived from our test data. Table 3.1 gives the number of picks in each iteration. At the beginning of the first iteration, because the initial velocity models are not accurate, many of the predicted arrivals are far from the true ones so that the true arrivals are outside the search window. Therefore, I obtain a relatively low number of high-FBER picks in this iteration. By the end of the fourth iteration, I have 22,516 FBER>5 and 19,638 FBER>10 P picks, 21,494 FBER>5 and 19,522 FBER>10 S picks. In comparison, the SCEDC provides 22,101 P picks and 18,093 S picks.

Figure 3.7a and 3.7b show the residuals between our automatic P and S picks and predicted picks. Similarly to the synthetic test, the residuals between the searched arrivals and the predicted ones are concentrated at the negative side in the first iteration, which suggests that the initial models are systematically too slow. The residuals decrease quickly and concentrate at zero in the later iterations, which is largely due to the improvement of the velocity models. Figure 3.7c and d compare the obtained picks with the SCEDC phase picks. By the 4^{th} iteration, 90% of P picks and 80% of S picks have residuals within ±0.15 s. Figure 3.8 shows a few waveform pick examples of events at different hypocentral distances with varying FBER. Even for low FBER signals, the picker still performs well. Figure 3.8b also shows that the picks are generally within 0.2 s from the phase picks obtained from SCEDC. In general, the consistency between the

automatic picks and the cataloged ones tends to decrease with decreasing FBER (Figure 3.9a and 3.9b). The picks that are made by our method but not in the catalog are also with relatively low FBER (Figure 3.9c and 3.9d). This partly demonstrates the method's picking ability in noisy data, although further selection criteria could be applied for quality control purpose.

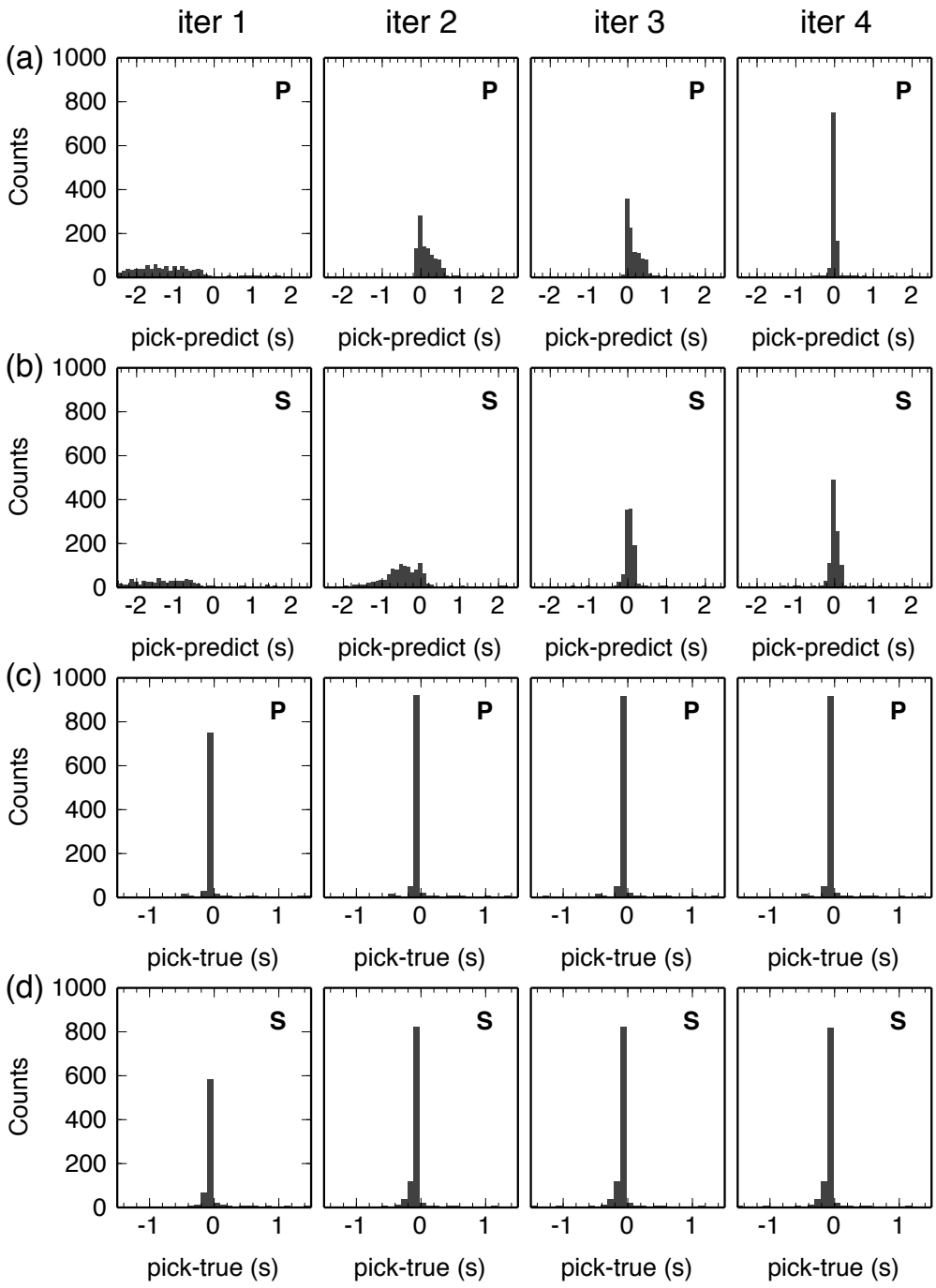

Figure 3.4 Histograms of P and S pick residuals in four iterations of the synthetic test. (a) P and (b) S arrival time residuals between searched and predicted arrivals from the initial (iter 1) and updated (iter 2, 3, 4) velocity models . (c) P and (d) S travel time residuals between the searched and true arrivals from the true velocity models. The bin size is 0.1 s.

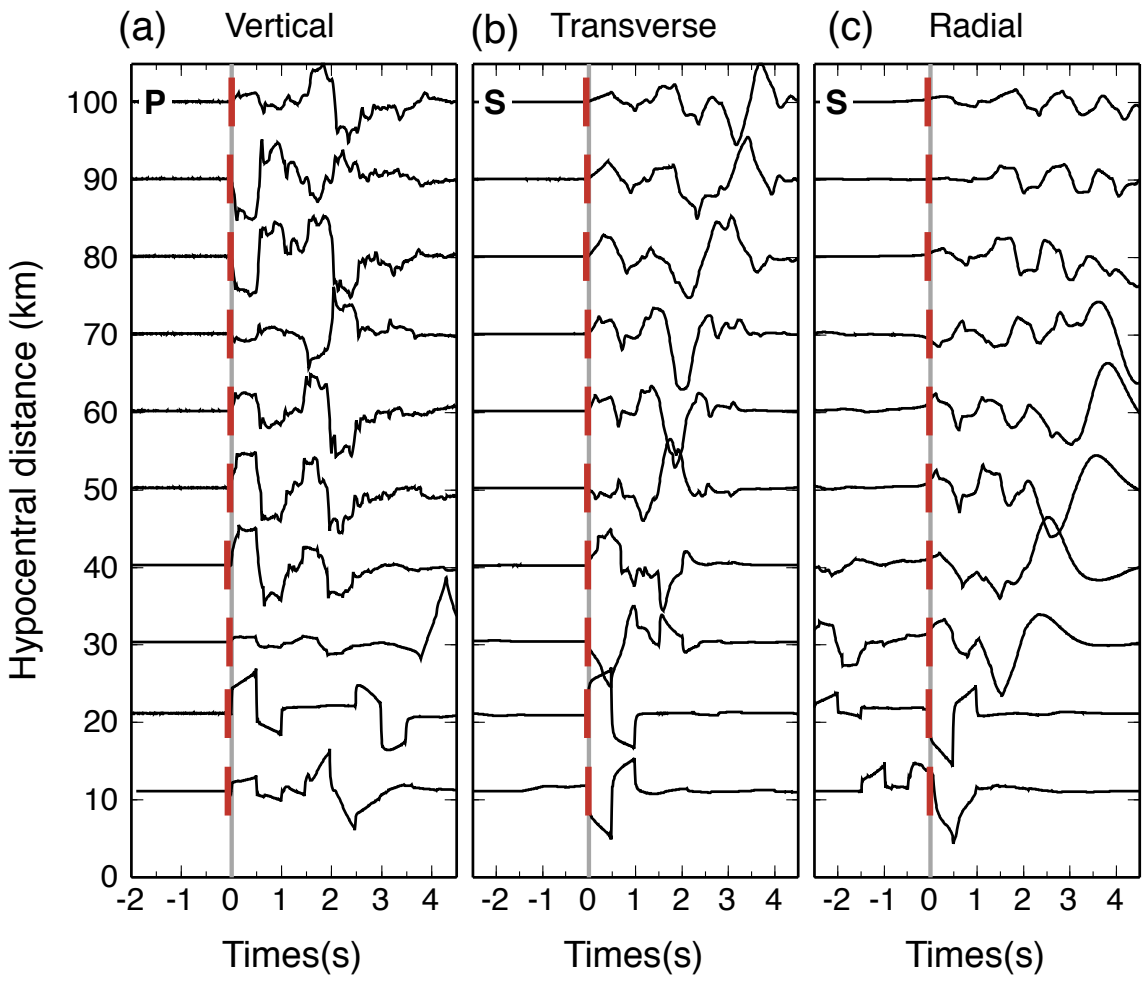

Figure 3.5 Examples of P and S picks on synthetic seismograms. (a) The vertical waveforms are aligned at true P arrivals (gray vertical line) and the automatic P picks are marked by red bars. The (b) transverse and (c) radial waveforms are aligned at true S arrivals (gray vertical lines), and red bars mark the automatic S picks.

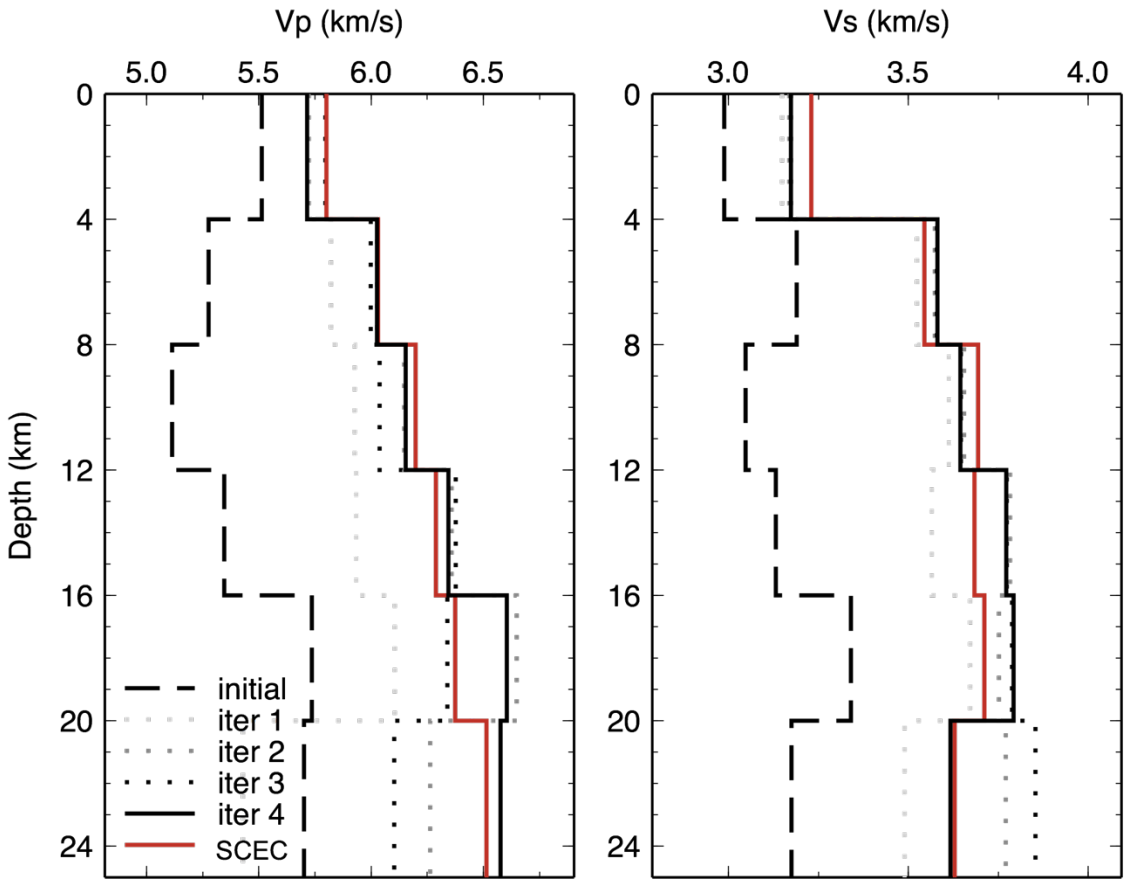

Figure 3.6 1D P and S velocity models in the real data test. Dashed lines and solid red lines represent initial and average SCEC models, respectively. The light gray, moderate gray, and dark gray dot lines represent the inverted velocity models in the 1st, 2nd, and 3rd iteration, respectively. The solid black line is the resulting velocity model in the 4th iteration.

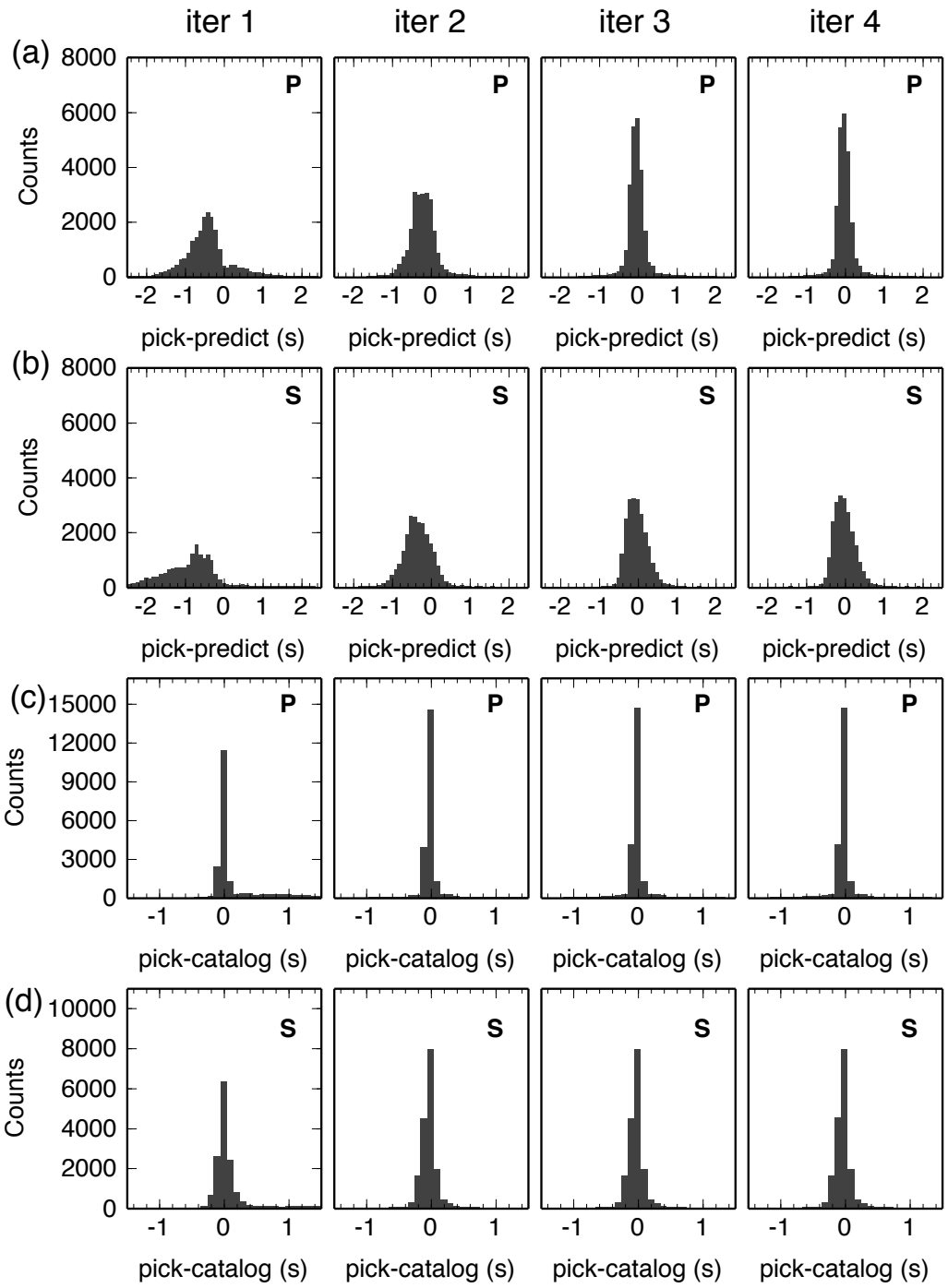

Figure 3.7 Histograms of P and S pick residuals at the end of each iteration in the real data test. (a) P and (b) S arrival time residuals between the searched and predicted arrivals from the initial (iter 1) and updated (iter 2, 3, 4) velocity models. (c) P and (d) S arrival time residuals between the searched and the referenced SCEDC phase arrivals. The bin size is 0.1 s.

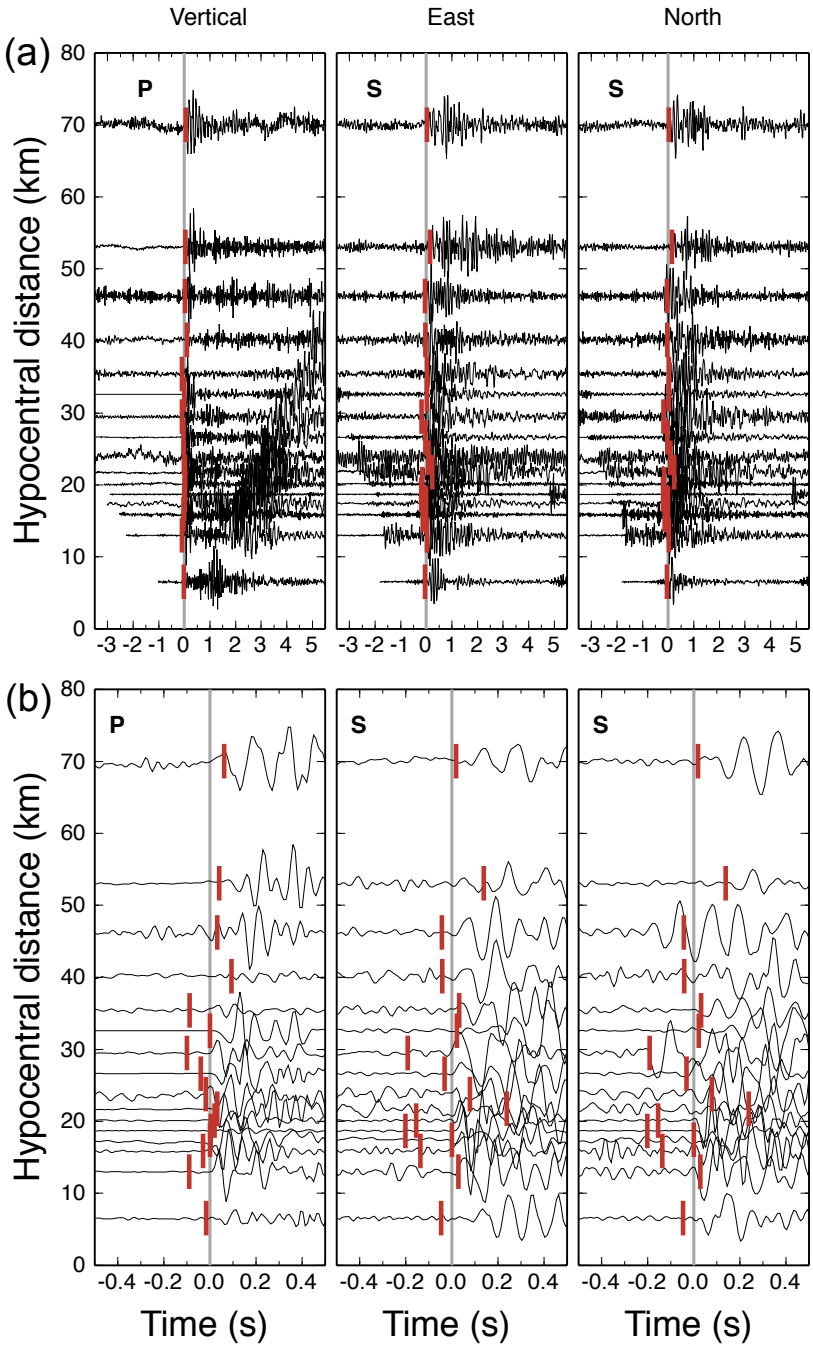

Figure 3.8 Examples of P and S picks on the Anza network data. (a) Left: the vertical waveforms are aligned at SCEDC P picks (gray vertical line), and red bars mark the automatic P picks. Middle and right: The east-component and north-component waveforms are aligned at SCEDC S picks (gray vertical lines) and the automatic S picks are marked by red bars. (b) The zoom-in plot of the same waveforms within ± 0.5 s of the SCEDC picks.

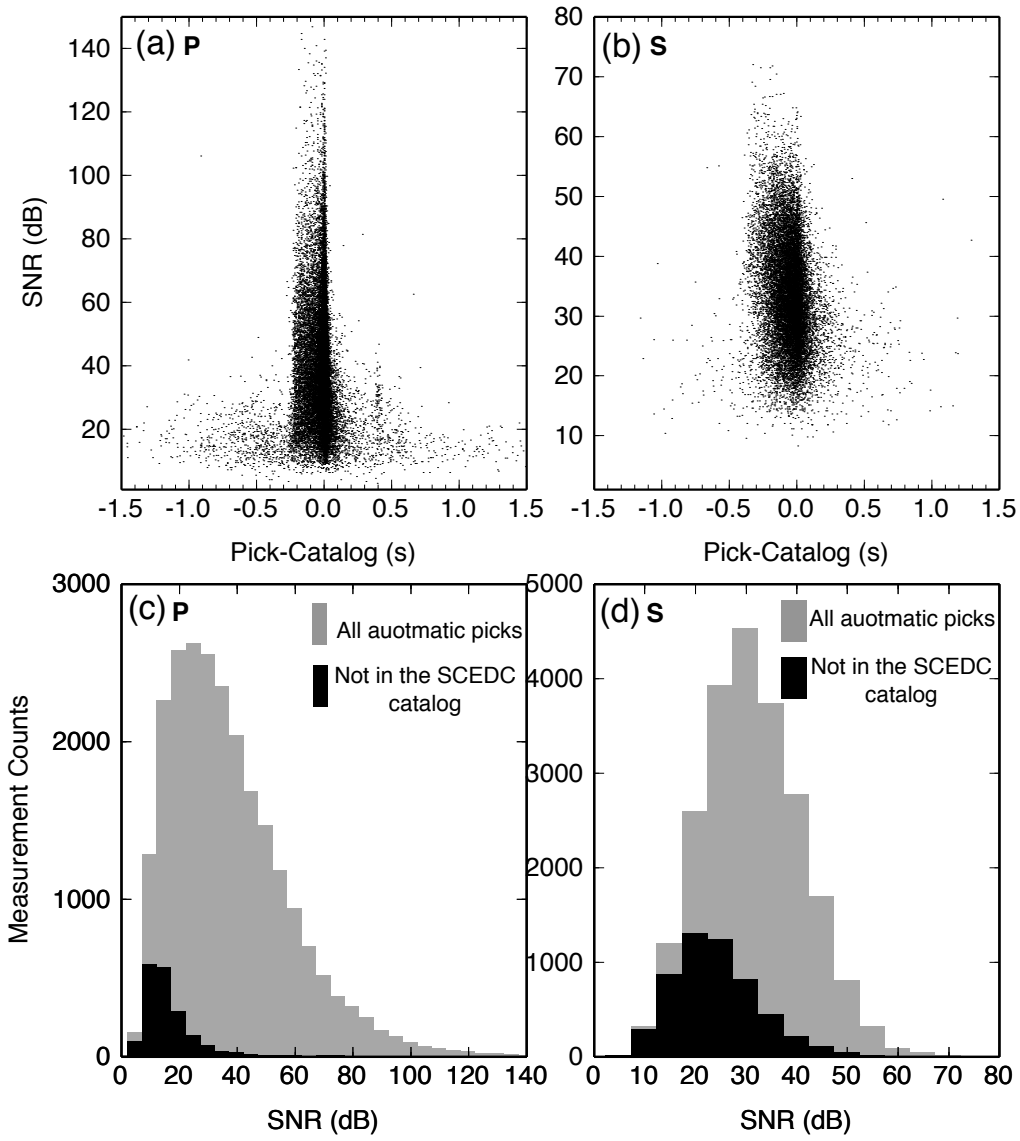

Figure 3.9 Distribution of FBERs for all the picks. (a) and (b): FBER versus time differences of automatic and cataloged picks for P and S waves, respectively. (c) and (d): Histograms of FBER distribution of all the automatic picks (gray bars) and those not in the SCEDC catalog (black bars), for P and S waves, respectively.

3.1.5 Discussions

In this study I presented a new method (termed 'Predict-Search-Invert-Repeat' or PSIR) to accurately pick the phase arrivals when preliminary earthquake locations and a 1D velocity model are available. This method essentially links a traditional characteristic

function search with simple 1D velocity model inversions. By allowing a certain degree of velocity inaccuracy, the characteristic function is confined to search within a range, thereby avoiding false picks that are far from the theoretical expectation. Our synthetic tests (Figures 3.3-3.5) demonstrate its ability to obtain accurate picks and converge from an inaccurate velocity model toward the true one. The test with Anza network data (Figures 3.6-3.8) shows a significant increase of S phase picks in comparison with existing catalog picks. The method could be useful for travel time tomography, where picks made outside reasonable P and S windows may introduce unreal velocity anomalies. In addition, the updated velocity model obtained using searched arrivals can also serve as a starting point for 3D seismic tomography.

Specially designed for the case where an event catalog is available, our method does not compete with many automatic arrival pickers for phase identification from scratch [e.g., *Ross and Ben-Zion*, 2015]. Instead, with a priori knowledge of event locations, the method increases the phase-pick success rate (especially S phases) and reduces false picks (picks that are significantly outside the typical arrival window or erroneous phases). Both are advantageous over characteristic functions alone. In addition to the tests above, this method has been applied to sizeable data sets, e.g. in the San Jacinto Fault Zone [*Li et al.*, 2015] and in the Costa Rica subduction zone [*Yao et al.*, 2016]. We find that the method generally achieves good accuracy in these data sets and can significantly reduce the workload of manual phase picking.

Our method considers the maximal FBER within the search range as the direct P and S arrivals. This may not be always true since other phases, such as P/S conversion, refracted (e.g., Pn or fault zone head waves) and/or reflected phases, may be more

impulsive than direct phases and could also occur within the search range. Therefore, if a better velocity model is available, decreasing the search range parameter ϵ could help to reduce the possibility of erroneous phase picking. In particular, a good choice of starting velocity model could be the one used for locating the events. An alternative would be to replace the STA/LTA with other characteristic functions that are capable of identifying additional phases [e.g., *Ross and Ben-Zion*, 2015; *Li and Peng*, 2016]. On the other hand, a threshold can be applied to select the picks with relatively higher FBERs, which tend to have sharper phase onset. Another assumption of the method is that event locations should be accurate enough, and that the differences between the actual arrivals and theoretical predictions are simply attributed to inaccuracy of the velocity model. For a data set with significant location errors, the proposed method inherently treats the location error as part of the velocity model error, which means the search-range parameter ϵ should be increased to reflect both event location error and velocity model error. Once the arrival search window is set large enough, the total error can be handled and picks can be still made. However, due to the coupled problem of event location and medium velocity, the inverted velocity model will be negatively impacted.

In the synthetic test, we obtained most of the picks after the first iteration (Figure 3.4c and 3.4d), while the velocity models became close to the true models at the later iterations (Figure 3.3). This is because once the velocity model differences decrease to 15%, most arrivals can be obtained, and remain unchanged, while the velocity inaccuracy is further reduced. Therefore, although the iterative process in principle can be implemented many times as necessary, based on our experience, two or three iterations are sufficient to obtain the phase picks but more iterations may be needed to update the

velocity models. Too many iterations are not recommended because of relatively low gain relative to computational expense. Another possibility is to generalize the method to 3D velocity model inversion. However, compared to 1D velocity model inversion, this does not provide further benefit for the phase picking, because the search window defined by velocity perturbation already handles a certain amount of lateral heterogeneities.

With the amount of available seismic data increasing exponentially at IRIS Data Management Centers and other data centers, we expect that our procedure could be useful for other types of seismological research in which event catalogs are already available.

3.2 Automatic Identification of Fault Zone Head Waves and Direct P Waves and Its Application in the Parkfield Section of the San Andreas Fault, California

Summary

Fault zone head waves (FZHWs) are observed along major strike-slip faults, and can provide high-resolution imaging of fault interface properties at seismogenic depth. In this paper I present a new method to automatically detect FZHWs and pick direct P waves secondary arrivals (DWSAs). The algorithm identifies FZHWs by computing the amplitude ratios between the potential FZHWs and DSWAs. The polarity, polarization and characteristic period of FZHWs and DSWAs are then used to refine the picks or evaluate the pick quality. I apply the method to the Parkfield section of the San Andreas Fault where FZHWs have been identified before by manual picks. I compare results from automatically and manually picked arrivals and find general agreement between them. The obtained velocity contrast at Parkfield is generally 5%-10% near Middle Mountain while it decreases below 5% near Gold Hill. I also find many FZHWs recorded by the stations within 1 km of the background seismicity (i.e., the Southwest Fracture Zone) that

have not been reported before. These FZHWs could be generated within a relatively wide low velocity zone sandwiched between the fast Salinian block on the southwest side and the slow Franciscan Mélange on the northeast side. Station FROB on the southwest (fast) side also recorded a small portion of weak precursory signals before sharp P waves. However, the polarities of weak signals are consistent with the right-lateral strike-slip mechanisms, suggesting that they are unlikely genuine FZHW signals.

3.2.1 Introduction

Large mature strike-slip faults tend to juxtapose blocks with clear lithological contrast [e.g., *Thurber et al.*, 2006; *Wdowinski et al.*, 2007; *Dor et al.*, 2008]. The resulting velocity contrast leads to significant differences in rupture behavior and seismic radiation from a homogeneous solid [*Ben-Zion,* 2001]. For a mode-II type rupture, the dynamic change of normal stress σ_n at the rupture tip along a bimaterial interface is opposite in two slip directions: the change of σ_n is tensile along the slip direction of the compliant solid, and compressive along the other direction [Weertman, 1980; *Andrews and Ben-Zion,* 1997; *Shi and Ben-Zion,* 2006]. This dynamic effect may result in a statistically preferred rupture direction when an earthquake initiates within a bimaterial interface [*Brietzke and Ben-Zion*, 2006; *Ampuero and Ben-Zion,* 2008; *Dalguer and Day,* 2009]. Because of drastic difference in the resulting ground motion due to directivity effect, a better understanding of bimaterial fault interface properties is important for seismic hazard assessment [e.g. *Ben-Zion*, 2006; *Brietzke et al.*, 2009; *Xu et al.*, 2012].

Bimaterial fault interface is expected to generate fault zone head waves (FZHWs), which refract along the interface with the seismic velocity of the fast side and radiate

from the fault to the slow side [*Ben-Zion*, 1989, 1990]. Beyond a critical distance, FZHWs arrive earlier than direct P waves at stations on the slow side. In such cases, direct P waves can be termed as direct wave secondary arrival (DWSA) [*Ben-Zion and Malin*, 1991; *Bennington et al.*, 2013]. The arrival time differences between the FZHWs and DWSAs can be used to estimate velocity contrast along a fault interface [*Ben-Zion et al.*, 1992; *Zhao et al.*, 2010; *Allam et al.*, 2014]. In addition, incorporating FZHWs into travel time tomography produces a sharper velocity contrast across the Parkfield section of the San Andreas Fault (SAF) than using the direct arrivals alone [*Bennington et al.*, 2013]. Furthermore, distinguishing preceding FZHWs from direct P arrivals can enhance the accuracy of focal mechanism and event location [*Ben-Zion and Malin*, 1991].

To obtain a robust estimate of velocity contrast along a fault, typically we need a large number of FZHWs and DWSAs. In most previous studies, FZHWs and DWSAs are picked manually, which is an onerous task. More importantly, visual identifications of these phases depend on personal experience and therefore are subjective. In addition, for quality control purpose, *Zhao et al.* [2010] classified the picks of FZHWs into three quality levels in terms of the sharpness of amplitude changes, which is again based on visual inspection. Recently, *Ross and Ben-Zion* [2014] developed a new algorithm for automatic picking of direct P, S phases and FZHWs. They first picked the initial phases by short-term-average/long-term-average ratio (STA/LTA) function. Next, they distinguished between FZHWs and DWSAs by calculating kurtosis and skewness functions, which are sensitive to polarity changes and other abrupt changes in waveform characteristics. In their algorithm, the arrival differences between FZHWs and DWSAs are upper bounded by the prediction of the maximum velocity contrast in the given

region.

In this paper, I present an alternative method to automatically distinguish between FZHWs and DWSAs based primarily on their amplitude differences and other characteristics. Different from the algorithm in *Ross and Ben-Zion* [2004], our method is based on preexisting first phase arrivals, and evaluates if the first arrival is a potential FZHW or simply a direct P wave. If it is a FZHW, our algorithm will pick the P wave or DSWA. To do this, I define new metrics of long-term and short-term amplitude ratios to track amplitude change. In addition, I propose a set of criteria for quality control purpose. The method is designed to fully exploit the characteristics of FZHWs and DWSAs, including amplitude, polarity, frequency, and polarization difference.

In the following sections, I first describe the method and various quality control parameters. Next, I apply our method to the Parkfield section of the SAF, where *Zhao et al.* [2010] have previously analyzed FZHWs and found clear variation of velocity contrast along the SAF strike. I systematically compare our results with manual picks by *Zhao et al.* [2010] and re-calculate the velocity contrast using the automatic picks.

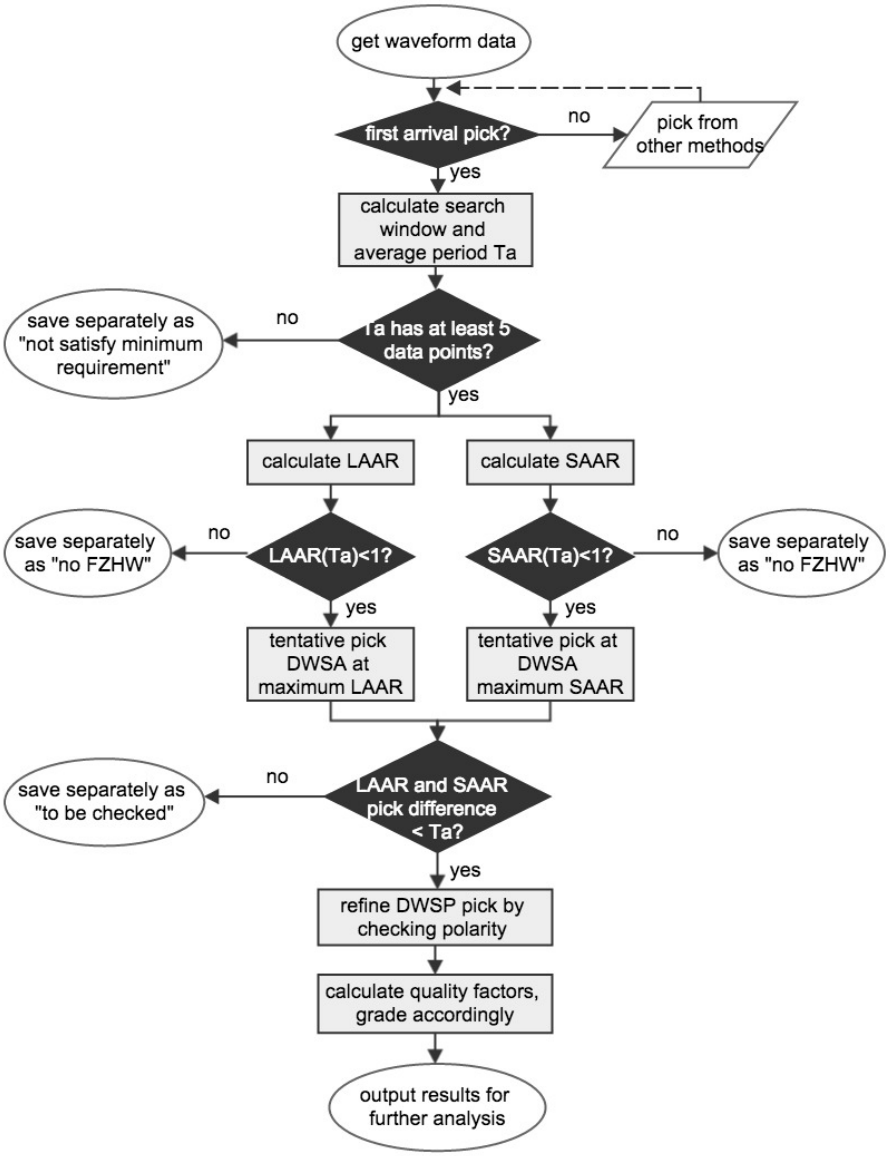

Figure 3.10 A flow chart of the algorithm for automatic detection of fault zone head waves (FZHW) and picking direct wave secondary arrival (DWSA) (i.e., the direct P wave). LAAR: long-term average amplitude ratio; SAAR: short-term average amplitude ratio.

3.2.2 Method

FZHWs are identified as emergent first arrivals and low-amplitude seismic signals with lower frequency and opposite polarities with respect to the direct P waves [e.g., *Ben-*

Zion and Malin, 1991; *McGuire and Ben-Zion*, 2005]. In addition, P waves are expected to polarize along the source-receiver direction while FZHWs are polarized in a direction controlled by the percentage of velocity contrast and local fault geometry [*Bulut et al.*, 2012]. Our automatic phase picking algorithm is based primarily on amplitude and polarity differences between these two phases. Other characteristics are used as additional quality control factors. The processing process is shown in Figure 3.10, with each step illustrated below.

Basic quantities: The velocity contrast across the bimaterial interface can be described by the degree *K*:

$$K = \frac{V_f - V_s}{V} \approx \frac{t_p - t_{hw}}{t_p - t_0} \approx \frac{t_p - t_{hw}}{t_{hw} - t_0} \tag{7}$$

where V_f, V_s and V denote the velocities of fast side, slow side and the average, respectively. t_p, t_{hw} and t_0 are the travel times of the DWSA and FZHW, and event origin time, respectively.

The approximation made in Equation 7 allows us to determine the search range for DWSA without assuming absolute velocities of both sides of the fault. If the event origin time t_0 and first arrival t_1 (either direct P waves of FZHWs) are known, the maximum search range t_2 for potential DWSA can be set by

$$t_2 = t_1 + K_{max}(t_1 - t_0) \tag{8}$$

where K_{max} is the maximum degree of velocity contrast allowed in a region. In this study we set K_{max} = 15% for the Parkfield case, above the maximum value of 10% observed by *Zhao* et al. [2010], and the maximum value of 10% used in *Ross and Ben-Zion* [2014].

Another important parameter used in the algorithm is the dominant period of the examined waveform. When the examined window is generally very short (typically less than 0.5 s), especially less than a full cycle of the dominant waveform, Fourier transform usually produces artifacts in the spectra domain due to window edge effect [*Peng et al.*, 2011]. Therefore, instead of Fourier spectrum, we use median instantaneous dominant frequency following the definition by *Barnes* [1993], which is found to be more stable for very short time window. Instantaneous dominant frequency can be calculated from instantaneous frequency $f_d(t)$, and the instantaneous amplitude or envelope R(t) as

$$f_d^2(t) = f_i^2(t) + \left(\frac{R'(t)}{2\pi R(t)}\right)^2 \quad (9)$$

The median value of the instantaneous dominant frequency trace is taken to be a counterpart of spectral dominant frequency. The dominant period T_d is reciprocal of f_d, and bounded within [0.05, 0.2] s. We use this quantity to approximate one full cycle of the early arriving waveforms.

Search parameters: To check if an initial arrival is a potential FZHW or direct P waves, the first characteristic is the sharpness of the first arrival. A FZHW generally has low amplitude and is followed by an abrupt increase of DWSA. Typically we pick its onset at a place with a sharp increase of amplitude in the displacement seismogram [*Ben-Zion*,

1989; *Zhao et al.*, 2010]. In practice, we can evaluate the amplitude change within a short segment of waveforms and compare the amplitude over a relative long window. To mimic this process, we use quantities that are named as long-term and short-term average amplitude ratios.

We define long-term average amplitude ratio (LAAR) and short-term average amplitude ratio (SAAR) by

$$LAAR(t) = \frac{\int_t^{t2} A^2(\tau)d\tau}{t2 - t} \Big/ \frac{\int_{t1}^{t} A^2(\tau)d\tau}{tp - t1} \cdot R^{\alpha}(t), \quad t \in [t_1 + T_d, t_2 - T_d] \tag{10}$$

$$SAAR(t) = \int_t^{t+Td} A^2(\tau)d\tau \Big/ \int_t^{t-Td} A^2(\tau)d\tau \cdot R^{\alpha}(t), \tag{11}$$

$$t \in [t_1 + T_d, t_2 - T_d]$$

$$R(t) = \int_t^{t+Td} A^2(\tau)d\tau \Big/ \int_{t1}^{t1+Td} A^2(\tau)d\tau \tag{12}$$

where *A(t)* is the amplitude at *t*, and *R(t)* is the amplitude ratio between the window right after *t* and the initial window. α is a small constant to modulate the effect of *R(t)*. LAAR consists of the global-sense amplitude change weighted by *R(t)*, while SAAR consists of the local-sense amplitude change weighted by *R(t)* as well. We add the term *R(t)* because we find that without this term, LAAR and SAAR are sensitive to low amplitude signal prior to real FZHW arrivals. Because we rely on the first arrival picks by other methods, and the first arrival may be sometimes picked slightly early than the real arrival. Therefore, the examined window contains a section of noise at the very beginning, and

without the term *R(t)* LAAR and SAAR will erroneously pick at the first arrival. Including the term *R(t)* can inhibit such error and helps to pick at position with more significant large amplitude. α is to fine-tune the effect of *R(t)* and cannot be too large to override other terms. In this study we set α to be a small constant 0.1. Although the α = 0.1 is somewhat subjective, we find that a small change around 0.1 does not change the results significantly.

Next we use the parameters LAAR and SAAR to judge whether the initial pick is a potential FZHW or simply a sharp direct wave. If LAAR or SAAR at t_1+ T_d is less than one, the amplitude within the first T_d is larger than the remaining waveform portion. This indicates that the initial phase has large amplitude and is sharp, and thus considered as a direct wave. Otherwise, the first arrival is treated as a potential FZHW. In this case, the second task is to pick DWSA. To do this, we take the times corresponding to the maximum of LAAR and SAAR within the search window as two tentative picks of DWSA. If the difference of these two picks is small enough, these picks are considered to be consistent in both "global" and "local" senses, which intuitively mimics manual picking consideration. The upper limit of the time difference is taken as T_d.

Next, the tentative pick of the DWSA is set to be the average times corresponding to the maximum LAAR and SAAR values. Since the polarities of FZHWs and DWSAs are opposite for a strike-slip focal mechanism and vertical faulting, we also check the polarity at the average time. If the corresponding polarity is opposite to that of the FZHW, this is set to be the final pick time. Otherwise, we search for a peak, trough or zero-crossing with opposite polarity within a window of T_d length centered at the average pick. If such position exists, the pick will be revised to the nearest one. Otherwise, the

pick will remain at the average pick, but tagged with one that does not satisfy the polarity requirement. Note that due to the existence of noise, it is generally unstable to check polarity of FZHWs using the peaks or troughs around early portion of initial phase (Ross and Ben-Zion 2014). Therefore, we check the polarity of the first phase by averaging the amplitude over a T_d /4 window after t_1 and comparing it with the value at t_1.

Quality control: *Zhao et al.* [2010] evaluated the picking quality by visually inspecting the sharpness of amplitude change. To mimic this in a more objective way, we use the following five criteria to judge the resulting quality of DWSA picks. These include polarity, period and polarization, and values of LAAR and SAAR at the final picks. As mentioned before, the polarity of DWSA is expected to be opposite to that of FZHW and thus can be used as the first quality factor. Secondly, FZHWs usually have longer periods than direct P waves [*Ben-Zion and Malin*, 1991]. The periods of FZHW and DWSA are estimated within their respective windows using the same algorithm of T_d calculation (t_1-t_p for FZHW and t_p-t_2 for DWSA). We expect that the average period T_d for FZHW to be larger than that of DWSA. Thirdly, FZHWs are polarized in a direction deviated from the source-receiver direction, and thus horizontal polarization can be used to help identify FZHWs [*Bulut et al.*, 2012; *Yang et al.*, 2015].

The polarization angles of FZHWs and P waves are computed using a covariance matrix method [*Jurkevics*, 1988]. Here we focus on horizontal polarization and thereby use a two-dimensional covariance matrix

$$\sigma = \begin{bmatrix} Cov(N,N) & Cov(N,E) \\ Cov(E,N) & Cov(E,E) \end{bmatrix} \tag{13}$$

where N and E are North and East components, respectively. Assuming the covariance matrix has two eigenvalues $\lambda_1 \geq \lambda_2$, the corresponding eigenvectors are u_1 and u_2, where the primary polarization angle is along the direction of u_1. The FZHW and DWSA window are taken as $0.8*(t_p\text{-}t_{hw})$ following the FZHW and DWSA arrivals to calculate their respective covariance matrixes. For ideal FZHW and DWSA, the polarization angle is expected to meet

$$|\phi_{hw} - \phi_0| > |\phi_p - \phi_0| \tag{14}$$

where ϕ_0 and ϕ_p are the polarization angles of FZHW and DWSA, and ϕ_0 is the back azimuth.

We evaluate the quality of FZHWs by the number of parameters satisfying pre-defined criteria, along with significant level of amplitude changes (Table 3.2). For measurements with three components, quality "A" means that the measurements satisfy all three requirements: polarity, period and polarization. Besides, peak LAAR and SAAR values at the final picks should be 5 times standard deviation above the average value. Although somewhat subjective, we find this threshold readily indicative of an abrupt amplitude change from FZHW to DWSA. Measurements that meet two requirements and have regular amplitude change are classified as "B". Measurements only satisfying one requirement have quality "C". The measurements satisfy none of the above criteria are discarded. For the measurements with only vertical components, we follow a similar grading scheme, with a difference that horizontal polarization is excluded (Table 3.2).

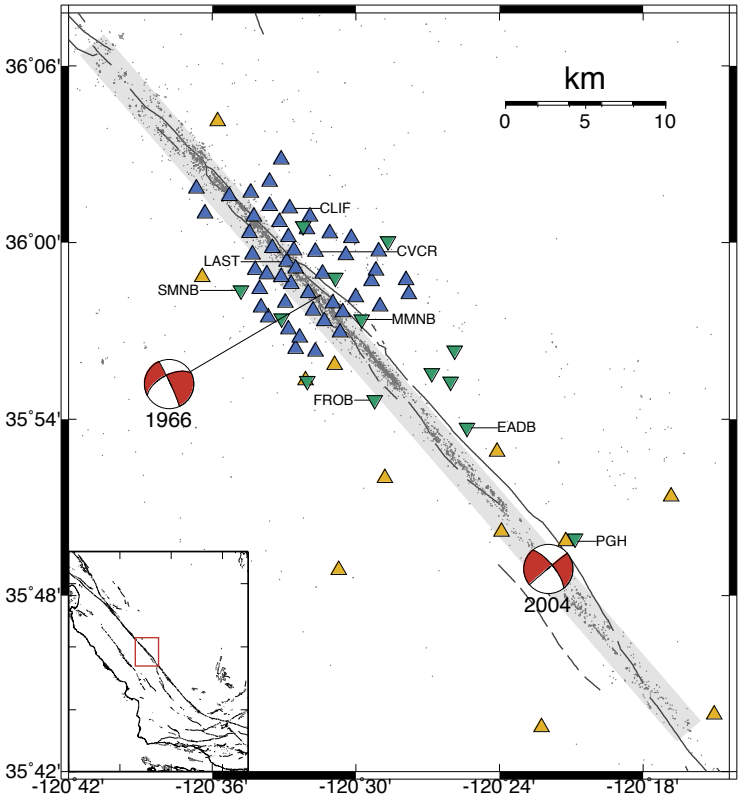

Figure 3.11 A map of the Parkfield section of the San Andreas Fault. Blue and yellow triangles are surface station in the PASO and NCSN, respectively. Green inverse triangles are borehole stations in the HRSN. Selected station names are labeled. Two beach balls represent the focal mechanisms of the 1966 and 2004 M6-type Parkfield earthquakes. The background seismicity from 1984-2005 (Thurber et al., 2006) are marked with dots. The light gray boxes mark the region (along-strike distance: -15 to 45 km, fault-perpedicular distance: -1 to 1 km) where events are used in this study and stations are considered as the FZ group. The inset shows the active faults in California and the red box marks our study area.

3.2.3 Parkfield data

We apply the method to seismic data around the Parkfield section of the SAF, where *Zhao et al.* [2010] have manual picked FZHWs and DWSAs and found clear along-strike variations of velocity contrast (Figure 3.11). We use the same seismic data from the borehole High Resolution Seismic Network (HRSN) in 2001-2005, the

temporary Parkfield Area Seismic Observatory (PASO) in 2001-2002, and the surface permanent North California Seismic Network (NCSN) in 1984-2005.

The preprocessing steps basically follow *Zhao et al.* [2010], and are briefly described here. We first select events that are confined within 1 km from the fault interface (approximated by a line with 139.2^{o} clockwise from north passing through 120.366W 35.815N, the epicenter of the 2004 M6 Parkfield earthquake). Next we remove the mean value of each velocity seismogram and apply a 1 Hz high pass filter to the data, and select high-quality waveforms with signal-to-noise ratio (SNR) > 5 for the HRSN data and SNR > 10 for the PASO and NCSN data. The PASO data is recorded by three components while the most NCSN data is recorded on vertical component only. Although HRSN data is recorded by three components, the horizontal orientations are not well constrained (T. Taira, personal communication, 01/2011). Hence, we use the vertical component only for stations in the NCSN and HRSN.

Next, we select station-event pairs which manual phase picks (either P wave only, or with both FZHWs and DWSAs) by *Zhao et al.* [2010]. The resulting data consists of 31648 waveforms from HRSN, 6386 from PASO, and 3393 from NCSN. Among these waveforms, there are 6271, 805 and 277 manual FZHW picks in the HRSN, PASO and NCSN data, respectively. We use the first arrival picks by *Zhao et al.* [2010] as an input, which also enable us to make a direct comparison with their results.

We divide the stations into three groups according to their relative locations to the fault. The fault-zone (FZ) group consists of stations that are located less than 1 km within the fault surface trace (approximated by a straight line same as the one for event selection). The remaining stations are classified as NE or SW groups relative to the fault.

As a result, there are 16, 36, and 22 stations belonging to the FZ, NE and SW groups, respectively.

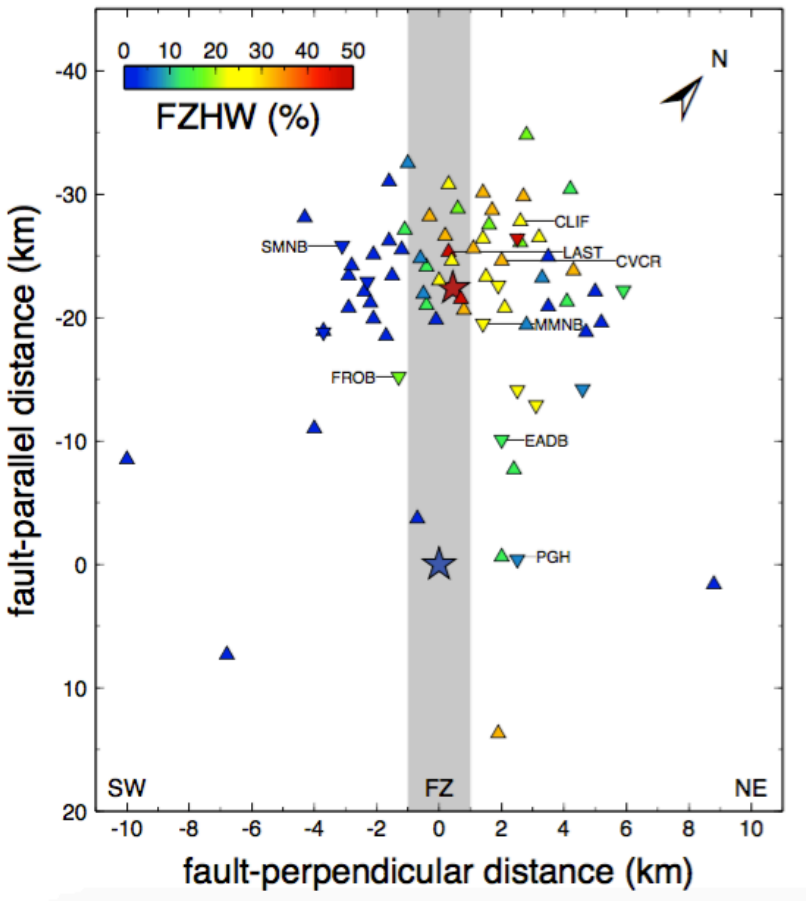

Figure 3.12 Percentage of FZHW observation on each station from the automatic detection. We rotate the station coordinate into fault-parallel (139.2° clockwise from north) and fault-perpendicular direction. Triangles and inverse triangles are surface and borehole stations, respectively. Selected stations are labeled. The percentage of FZHW observation at each station is color coded. Note that the stations on the SW (fast) side generally have a very small percentage of FZHW observation. The red and blue stars mark the epicenters of the 1966 and 2004 M6-type Parkfield earthquakes, respectively. The gray shaded area marks the ± 1 km around the majority of seismicity and approximate low-velocity zone.

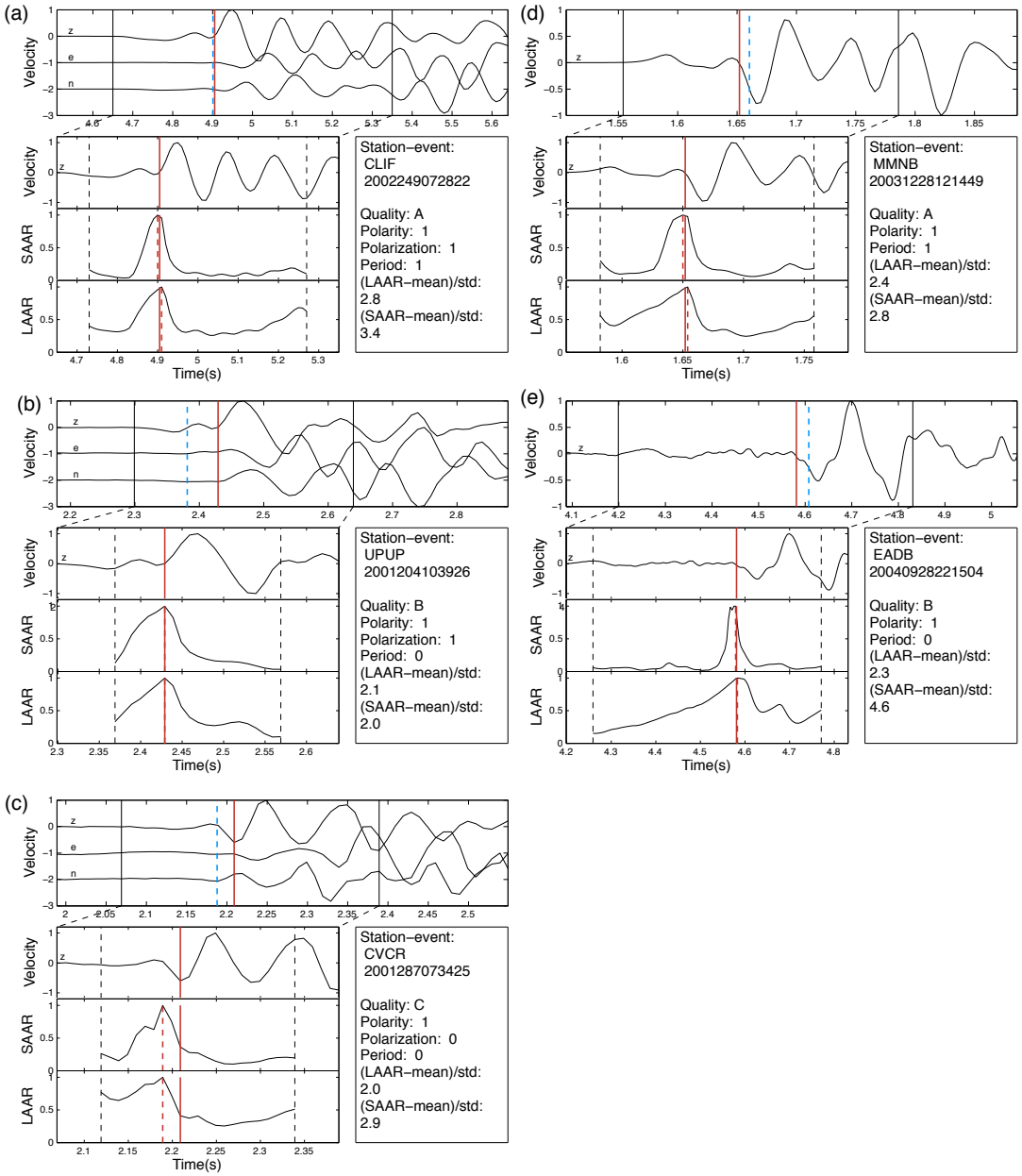

Figure 3.13 Pick examples with different qualities for measurements on three components at the PASO stations. (a) An example of quality A picks on three components at station CLIF. The top panel is normalized three-component velocity seismogram. The left and right solid black vertical bars mark the first arrival and the end of search window. The left and right dashed black vertical bars mark one average period length that is used as minimal window of FZHW and DWSA when calculating LAAR and SAAR, respectively. The red bar marks the final pick. Note that red and blue bars may overlap. The left bottom three panels are the vertical waveform, LAAR, and SAAR curve within the search window. The blue bars mark the tentative pick at the LAAR or SAAR maximum, and the red bar marks the final pick. The information and quality factors are listed in the right panel. Panels (b)

and (c) are examples for B and C quality using three-component grade scheme, respectively. The symbols are the same as (a). Panels (d) and (e) are examples of A, B quality for vertical-component grade scheme, respectively.

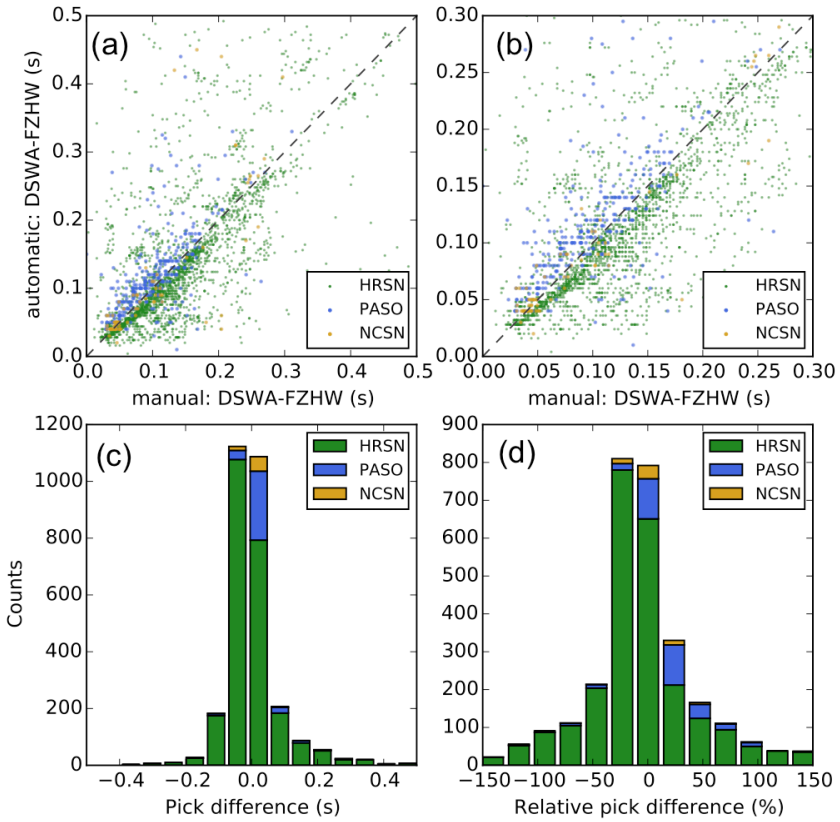

Figure 3.14 Comparison between automatically and manually picked time differences between the DWSAs and FZHWs. (a) Green, blue and yellow dots represent the time differences between DWSA and FZHW picks on HRSN, PASO and NCSN, respectively. The thick black line is the one to one line. (b) A zoom-in plot of (a) in the 0-0.3 s window. (c) Histogram of the automaticly and manually picked time differences with 0.05 s bin width. Green, blue and yellow bars mark the results for the HRSN, PASO and NCSN, respectively. (d) Histogram of pick differences relative to the time average differences between FZHW and DWSAs.

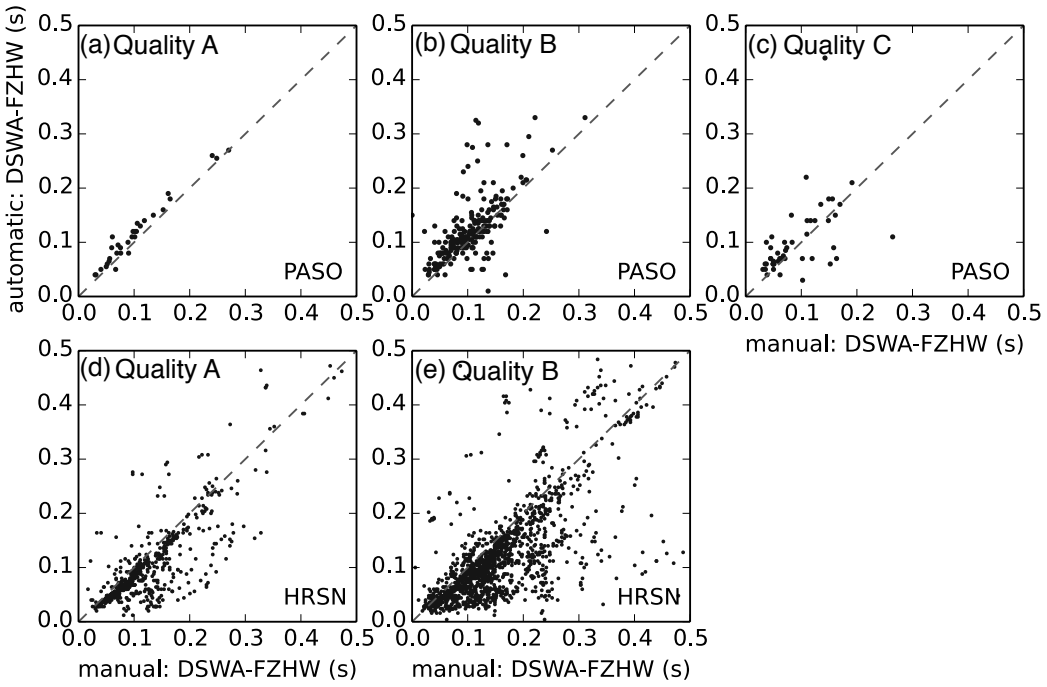

Figure 3.15 (a-c) Comparison of picks with different quality (A-C) and manual picks on the PASO network. (d-e) Same comparison on the HRSN network (Quality A and B).

3.2.4 Results

General Patterns: Overall we obtain 4612 automatic DWSA picks in HRSN, 973 in PASO and 262 in NCSN, which are comparable with manual picked arrivals (6271, 805 and 277 in HRSN, PASO, and NCSN). Figure 3.12 shows the percentage of identified FZHWs among the first arrivals on each station. Overall, the NE and FZ stations have 19.0% and 19.3% events that produce FZHWs, respectively. Some stations (e.g., the PASO station LAST and the HRSN station SCYB) have FZHW observations higher than 40%. In comparison, the SW stations have only 4.7% and most SW stations have few or no FZHW recordings. The only exception is the FROB station, which has 18.5% of

FZHW observation. Figure 3.13 shows pick examples on three-component data for quality grade A, B, and C (Figure 3.13a-3.13c), and A, B for vertical-component only (Figure 3.13c-3.13d). In general, quality A, B and C corresponds excellent, good and fair picks, respectively. And as shown below, higher quality picks show generally better consistency with manual picks.

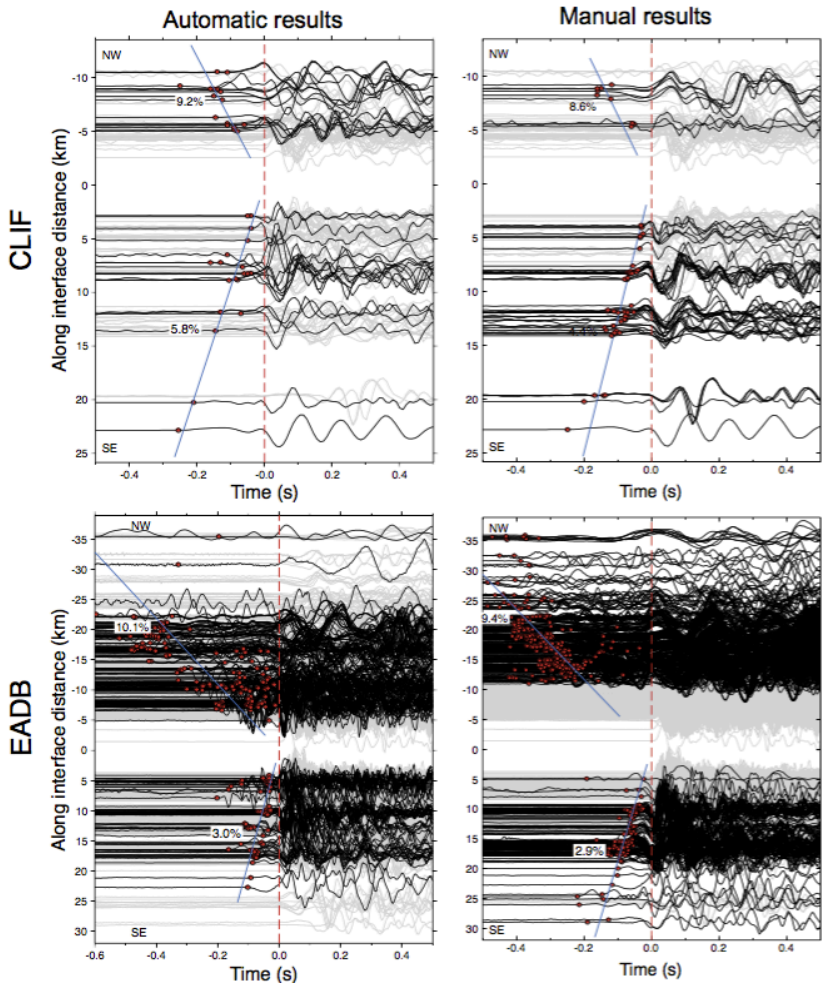

Figure 3.16 Comparison of automatically and manually picked DWSA at the PASO station CLIF and the HRSN station EADB. (a) Velocity seismograms recorded at the PASO station CLIF showing the moveout between FZHW and DWSA picked automatically (left) and manually (right). Black ones are waveforms with FZHW and gray ones are only with direct P waves. The red dots are the FZHW arrivals and the waveforms are aligned at the picked DWSA (red dash line). The blue lines are the linear regression without intercept term. The corresponding velocity

contrast estimated from the slope is labeled. (b) Comparison on the HRSN station EADB. Symbols are the same as (a).

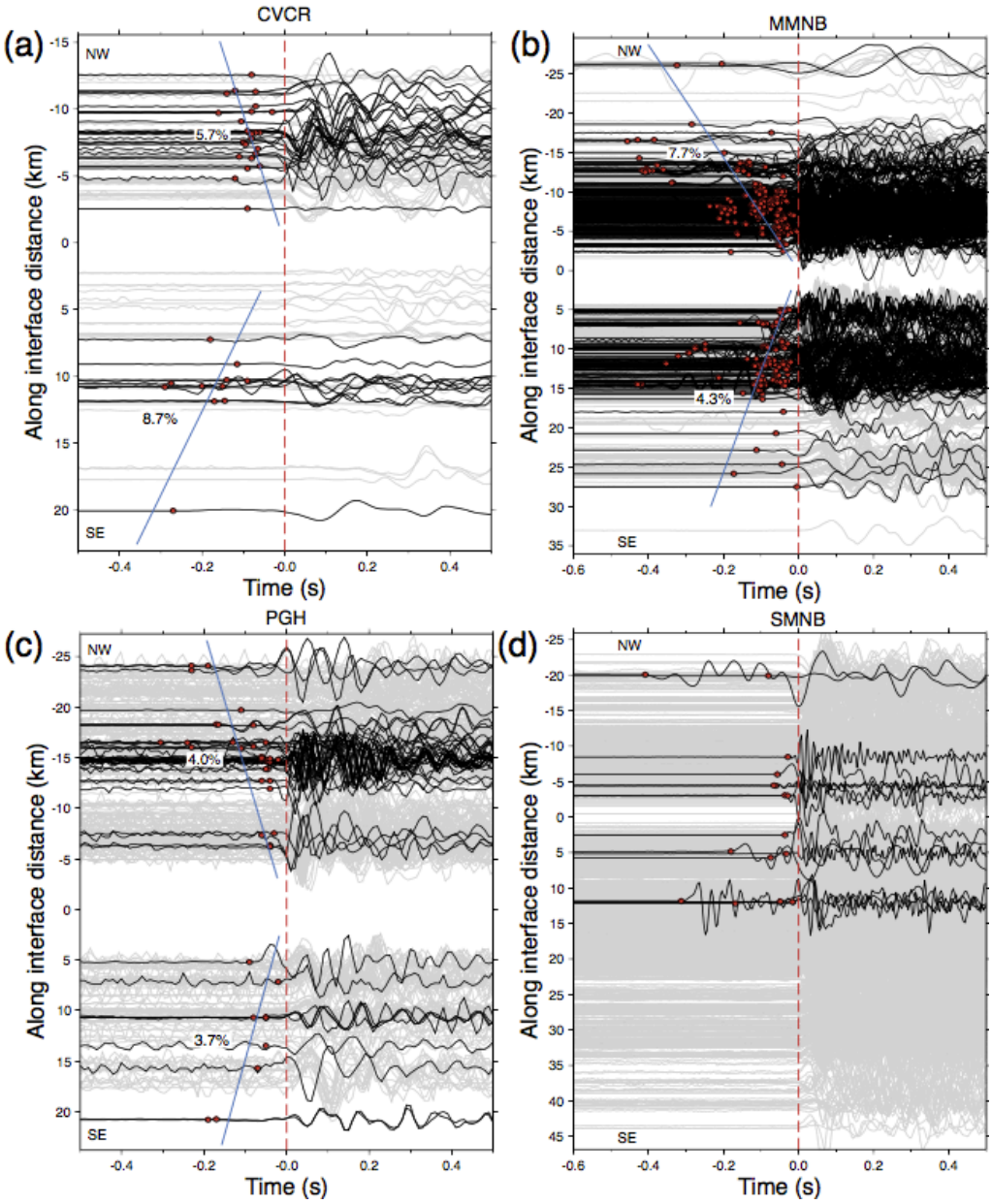

Figure 3.17 Examples of velocity seismograms showing the FZHW and automaically picked DWSA arrivlas (see station locations in Figure 3.11). (a-c) velocity seismograms recorded at the PASO station CVCR, the HRSN station EADB, the NCSN station PGH, respectively. Among them, CVCR is considered to be within the FZ group, and the other two are on the NE side. (d) velocity seismograms recorded at HRSN station SMNB on the SW side showing sparse FZHW and random moveout between FZHW and DWSA. Other symbols are the same as Figure 3.16.

Comparison with manual picks: In this section we compare the automatic and manual picks for all analyzed events. Figure 3.14a and 3.14b show the time differences between DWSAs and FZHWs between the automatically and manually picked phases. Although with some scatters, the majority of them cluster near the 1:1 line. The histogram (Figure 3.14c) of residuals between automatic and manual picks is concentrated around zero, and 60% of them are within 0.03 s, i.e. three data samples. The mean residual is -0.01 s, suggesting a minimal systematic picking difference between the manual and automatic picks. The relative pick difference, which is defined as the difference over their mean, shows a relative wide spread (Figure 3.14d). Although some of the automatic picks change by more than 100%, most of them are concentrated within 25% of change. In addition, Figure 3.15 shows comparisons between automatic and manual picks in different quality grades. Generally automatic picks with higher qualities are more consistent with manual picks, which reflects their quality grades to certain extents.

If the bimaterial interface is coherent along the interface, the differences of DWSA and FZHW are expected to systematically increase with fault interface distance [*Ben-Zion and Malin,* 1991]. Hence the average velocity contrast can be estimated the following equation:

$$dt \sim r\left(\frac{1}{V_s} - \frac{1}{V_f}\right) \sim r\left(\frac{V_f - V_s}{V^2}\right) \tag{15}$$

where *dt* is arrival difference between DWSA and FZHW, *r* is along-interface distance, and *V* is the average velocity which is assumed to be 5.5 km s^{-1} in this region [*Zhao et al.,* 2010]. Here we obtain the slope and its uncertainty using linear regression without the intercept term, which is slightly different from *Zhao et al.* [2010]. We exclude the

intercept term because it has no clear physical meaning according to Equation 15. In other words, we force arrival time difference *dt* to be zero with zero along-strike distance.

Next we calculate velocity contrast on the stations that have at least 50 input waveforms and the FZHW percentage higher than 10%. For comparison, we also recalculate the velocity contrast from the manual picks of *Zhao et al.* [2010] using the fitting function without intercept term (Equation 15). Figure 3.16 shows examples of FZHWs at the PASO station CLIF and the HRSN station EADB using automatic and manual DWSA picks, respectively. At station CLIF, velocity contrasts at the NW side measured from automatic and manual picks are ~9%, although the difference at the SE side is slightly greater than 1%. The velocity contrasts at station EADB for events at both the NW and SE side are consistent.

Figure 3.17a-3.17c shows additional examples of FZHWs at stations CVCR, MMNB and PGH that are located on the NE (slow) side from NW to SE along the SAF (Figure 3.11). They record substantial FZHWs and show systematic moveout between FZHWs and DWSAs. In comparison, the stations on the SW (fast) side have very few FZHWs, and do not have clear systematic moveout with along-strike distances (e.g., SMNB, Figure 3.17d).

We summarize the obtained velocity contrasts for sections to the NW and SE centered at the stations in the Parkfield area (Figure 3.18a). A general pattern is that the velocity contrast is high near the Middle Mountain and diminishes toward Gold Hill. The velocity contrast is below 5% near the epicenter of the 2004 Parkfield earthquake. This is consistent with *Zhao et al.* [2010], although we have 11 more stations in the FZ group. A direct comparison of the velocity contrasts between the automatic and manual picks

shows that they generally follow the 1-1 line, despite a few outliers (9b). Nevertheless, the velocity contrasts to the NW tend to have high values (5%-10%), while the velocity contrasts to the SE are significantly clustered at the low values (<5%).

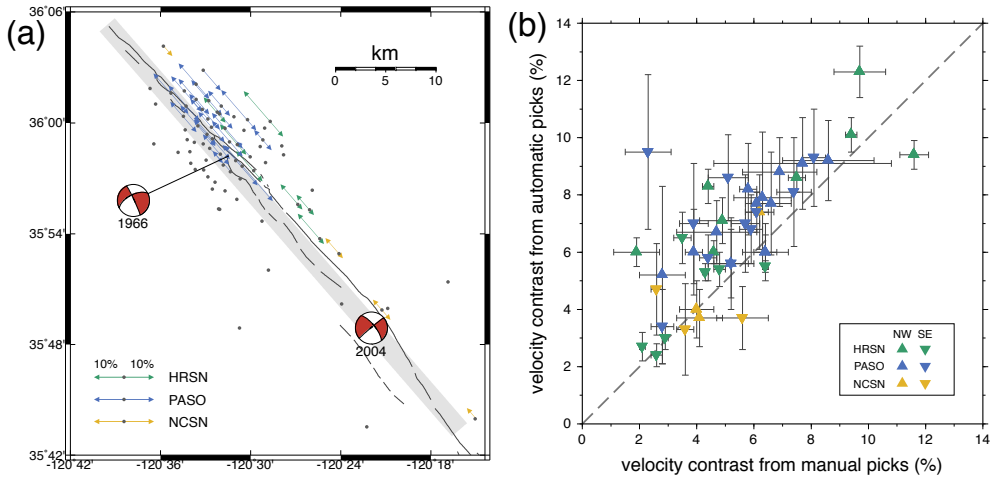

Figure 3.18 A summary of the obtained velocity contrasts across the Parkfield section of the SAF. Arrow length represents the velocity contrast value, and arrow direction represents the obtained velocit contrast using events from either NW or SE direction. Blue dots are stations. Other symbols are the same as in Figure 3.10. (b) Comparison of velocity contrasts measured from automatically and manually picked DWSAs. Blue, green and yellow symbols represent results for the PASO, HRSN and NCSN network, respectively. Triangles and inverse triangles are measurements using events from NW and SE directions, respectively. The dashed line marks the one to one relationship. Horizontal and vertical error bars are for manual and automatic results, respectively.

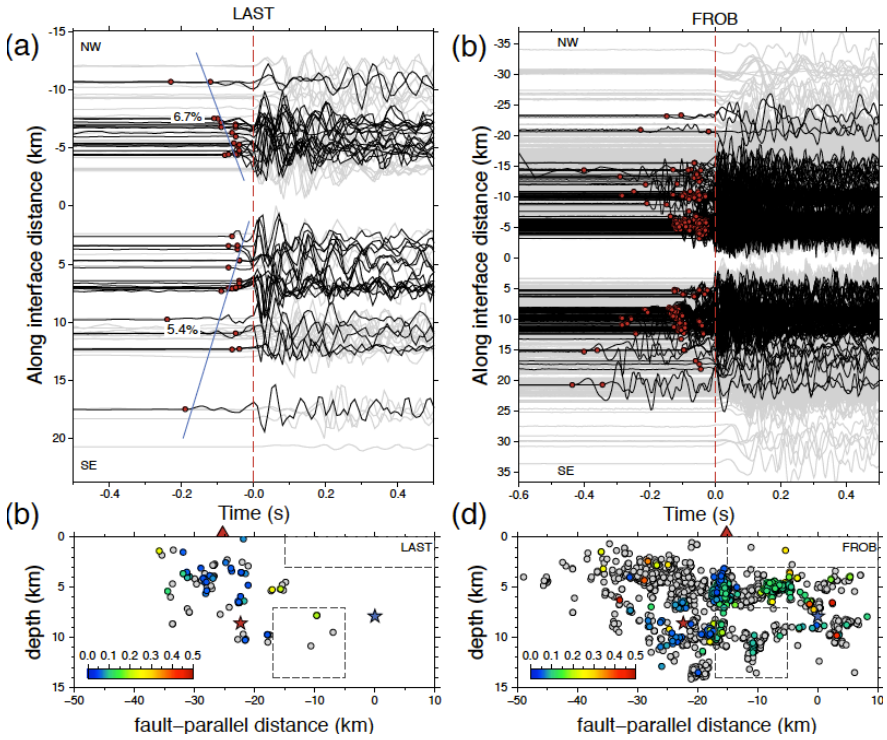

Figure 3.19 Examples of FZHWs and/or FZHW-like signals recorded by the FZ station LAST and station FROB in the SW side (see station locations in Figure 3.11). (a) Moveout of FZHWs with along-strike distances at FZ station LAST. The bottom panel shows the cross-section of events with and without FZHW generation. The events with FZHWs are colored by the time differences between the DWSA and FZHW arrivals. Gray earthquakes, respectively. Dashed boxes mark the approximated location of reverse velocity contrast patches observed by Thurber et al. (2006). (b) Moveout of FZHWs (top) and cross-section of events recorded at station FROB in the SW side. Other symbols are the same as in (a).

False and missed identification of FZHWs: It is possible that some early arrivals other than FZHWs may share some common features with FZHWs, which may be caused by site effect, surface reflection, horizontal interfaces, and/or source effects. Our method and quality control scheme is designed to look for phases that have consistent FZHW characteristics, which is expected to reduce the picks of phases induced by other effects. However, false picks are still inevitable due to waveform complexity. Therefore, it is important to check the rate of false picks, in order to properly evaluate the effectiveness of our automatic method. FROB station is of particular interest because it is on the SW side but has 18.7% FZHW detection rate. One possible explanation is that these FZHWs are produced by a local reversal of velocity contrast (Figure 3.19b) between Middle Mountain and Gold Hill that was imaged by P-wave and joint P-FZHW tomography [*Thurber et al.*, 2006; *Bennington et al.*, 2013]. However, most picks on FROB show no clear systematic moveout with increasing along-fault interface distance (Figure 3.19b). Given that FZHWs should have reverse polarity predicted by the focal mechanism, we inspect some of the detections and indeed find a significant portion of dubious picks, as shown in Figure 20. The waveforms of these early arrivals all have weak amplitudes, which is one of the important characteristics of FZHW. However, a systematic inspection of waveforms on FROB reveals that 94% of the identified "FZHW" phases have first

motion consistent with the predictions for the direct P waves with right-lateral strike-slip radiation patterns, which is inconsistent with opposite polarity of FZHW and direct P wave associated with a shear slip on the bi-material interface. A similar result is observed on SMNB. One possible explanation could be that FZHW and direct P wave take off in the same quadrant, resulting in similar polarity. In other words, their focal mechanisms are not purely strike-slip on the SAF. However, this phenomenon is only observed at a few stations on the SW side. For example, for MMNB and EADB, we find only a 5~10% of identifications are suspicious (i.e., same polarities between the P and FZHWs). These observations are also consistent with the systematic moveout observed at stations EADB and MMNB, and lack of moveout at stations FROB and SMNB. For now we tentatively classify those observed at stations FROB and SMNB as 'false picks'. A detailed study is needed to further identify the cause of these weak amplitude phases at stations on the SW side of the SAF.

In addition to 'false picks', the method also missed some picks present in manual results. This could be due to the requirement of mutual agreement between LAAR and SAAR picks, which is meant to minimize the number of false picks rather maximize detection rate. Besides, manual inspection has flexibility to adjust and reconsider the picks based on the general profiles and moveout [*Allam et al.*, 2014], while the automatic method follows more objective criteria without human interference. Another piece of uncertainty results from possible multiple phases present in the search window. In this case, the LAAR and SAAR curves may have different maxima, and hence is either dropped out or flagged with low qualities. But this issue is also not avoidable for manual

picking. It inherently lies in the difficulty in recognizing the real ray path for multiple phases using a single waveform.

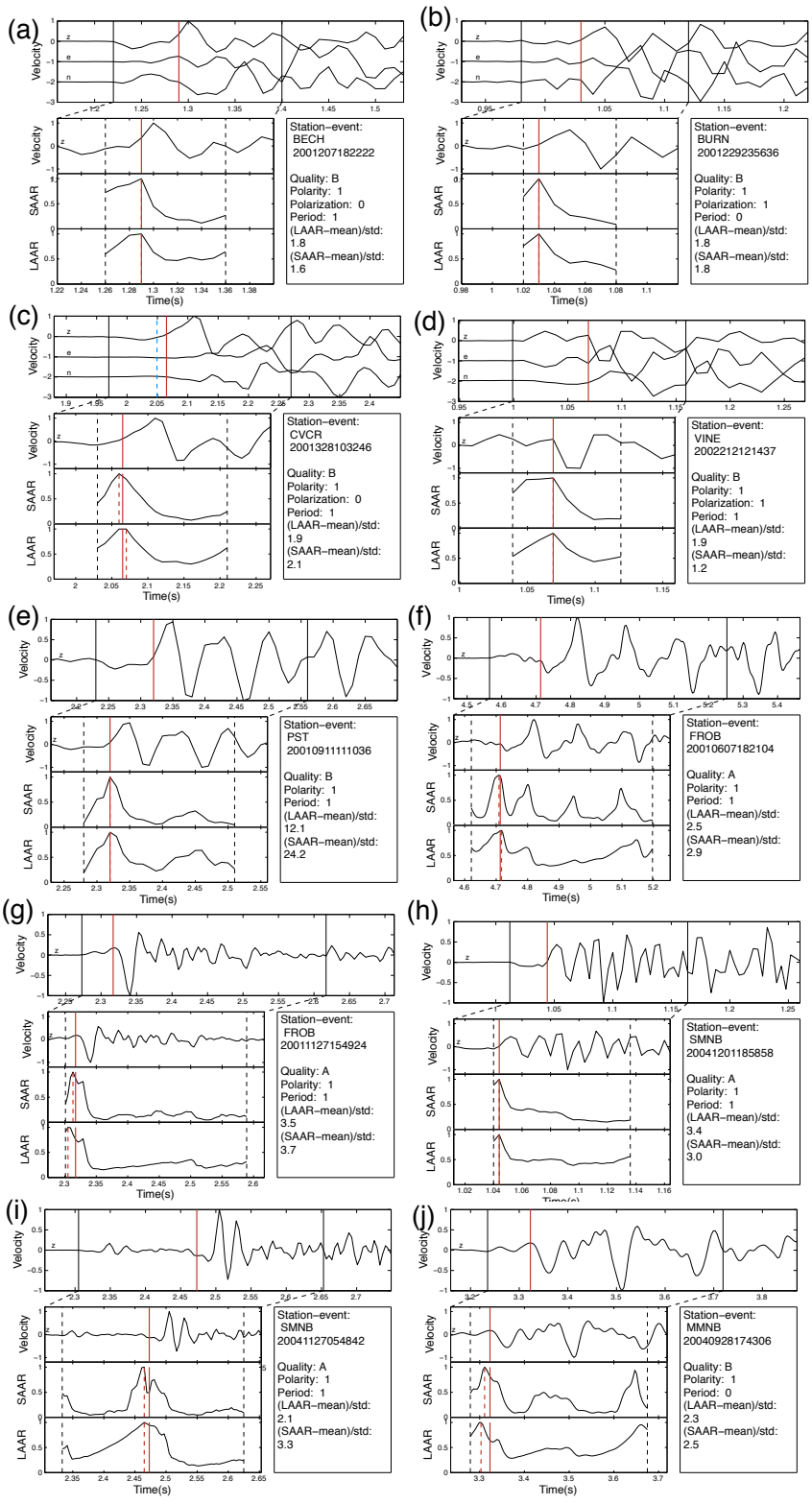

Figure 3.20 Examples of false detections of FZHW. Symbols are the same as in Figure 3.13.

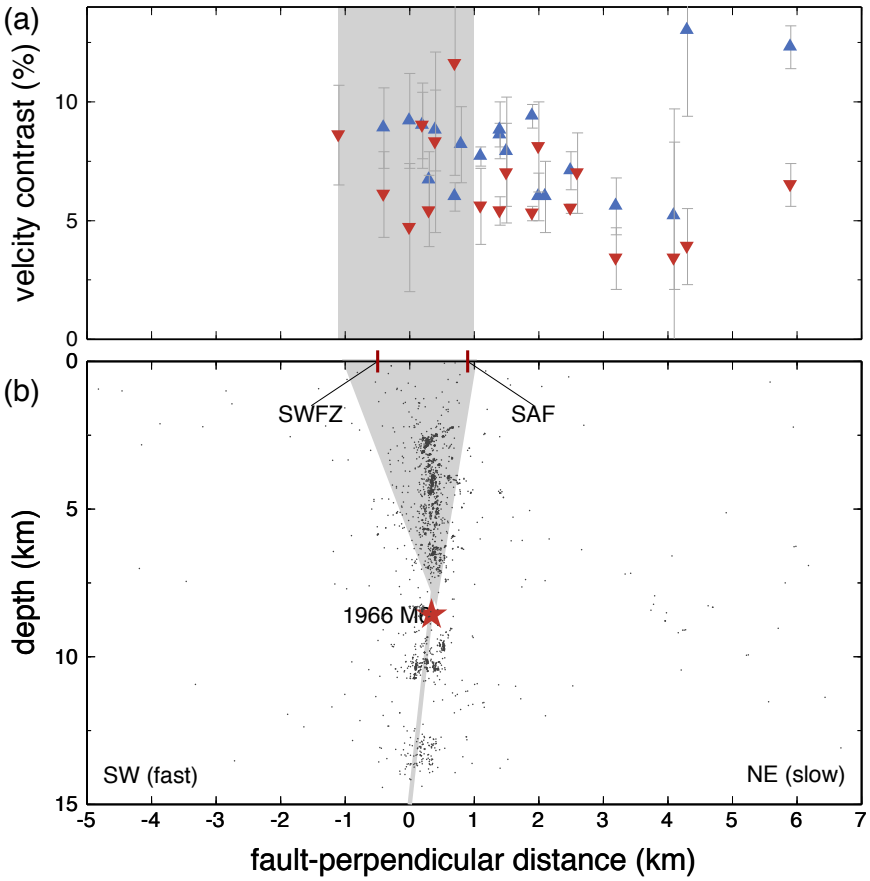

Figure 3.21 Velocity contrast values across the fault around the 1966 M6 epicenter. Blue triangles and red inverse triangles are measurements using events from NW and SE sides of the stations, respectively. (b) A schematic fault model. The gray area represents the approximate location of the low velocity damage zone and the primary fault interface. The red triangles mark the surface expression of the Southwest Fracture Zone (SWFZ) and the main trace of the San Andreas Fault (SAF). The red star represents the hypocenter of the 1966 M6 earthquake. The background seismicity are events in 1984~2006 within 5 km from the 1966 M6 epicenter along the fault strike [*Thurber et al.*, 2006].

3.2.5 Discussion

In this study we presented an automatic method to detect FZHWs and DWSAs, which allowed us to systematically re-analyze bimaterial fault properties in the Parkfield of the SAF. The obtained velocity contrast shows clear along fault-strike variations, which agreed well with the results from manual picks [*Zhao et al.*, 2010]. The overall

patterns of velocity contrast are also compatible with both geological and geophysical observations that the NE block has slower velocity than the SW block [e.g., *Eberhart-Phillips and Michel*, 1993; *Thurber et al.*, 2006].

One notable difference is that our automatic search method identifies a large number of FZHWs at FZ stations, which has not been reported by *Zhao et al.* [2010] For example, we found 45.5% FZHW rate on the LAST station, while *Zhao et al.* [2010] did not report any FZHW on this station at all (Figure 3.12). The FZ stations have comparable percentage of FZHW observations with the stations on the NW side and also show systematic moveout (e.g., station LAST, Figure 3.19a). The velocity contrasts at FZ stations are comparable those at stations on the NW side (Figure 3.21). Note that our approximated fault line mainly follow the aftershocks of the 2004 Parkfield event, which is close to the surface expression of the South West Fracture Zone (SWFZ), rather than the main trace of the SAF [*Thurber et al.*, 2006]. In this case, our observations contradict a fault model that is simply composed of a fast and slow block on both sides of the fault interface [e.g., *Ben-Zion and Malin*, 1991; *Peng et al.*, 2010].

Instead, our observation could be qualitatively explained by a wide low-velocity zone (LVZ) sandwiched between two quarter-spaces (Figure 2.21). In this case, the LVZ would produce two velocity contrast interfaces against two blocks, resulting in FZHWs observed at most stations within the LVZ. At Parkfield, features of LVZ have been observed, based on fault zone trapped waves (FZTW) that propagate within narrow LVZ [*Li et al.*, 2004; *Lewis and Ben-Zion*, 2010], as well as wider zones from travel time inversions at regional scale [e.g., *Zhang et al.*, 2009], attenuation [*Bennington et al.*, 2008], and magnetotelluric observations [*Unsworth and Bedrosian*, 2004]. The width of

LVZ inferred from FZTWs are generally 200-300 m, while the width from other studies are generally on the order of 1-2 km, bounded by the SWFZ and the main trace of the SAF. This suggests that large major fault zones like the SAF likely have hierarchical structures [e.g. *Ben-Zion and Sammis*, 2003] so that large-scale LVZs can be detected only by the regional-scale geophysical inversions, while FZTW observations have higher resolution but are based on short cross-fault arrays (a few hundred meters) and hence are able to see at finer-scale local FZ structures. It is also possible is that regional-scale geophysical inversions do not have the resolution to image the few-hundred-meter wide trapping structures, while the dense cross-fault arrays are not long enough to reveal the 1-2 km wide less-damaged FZ structures [e.g., *Cochran et al.*, 2009].

Nevertheless, our observation of FZHWs for stations on both sides of FZs is generally consistent with the existence of a wider LVZ at Parkfield. Interestingly, *Yang et al.* [2015] also found clear FZHWs on both sides of the faults that ruptured during the 2010 Mw6.9 Yushu earthquake sequence, and they suggested an existence of a 5-km wide LVZ beneath a pull-apart basin. Simulations of in-plane rupture show that, in such type of sandwich structure, rupture tends to migrate spontaneously to both bimaterial interfaces, with each interface having opposite preferred propagation direction [Brietzke and Ben-Zion, 2006].

Horizontal polarization has been used to distinguish FZHW and DWSA [*Bulut et al.*, 2012; *Allam et al.*, 2014; *Yang et al.*, 2015], because DWSA is expected to be radial while FZHW is radiated from the fault with a certain angle to the radial direction. We include this in our algorithm as a quality factor (Equation 14). However, it is somewhat surprising that only 56.4% automatic measurements meet this requirement, which is

barely above the 50-50% chance. This is not only observed in the automatic results, but also in the manual picks from *Zhao et al.* [2010], whose value is 53.1%. Figure 2.22 show the polarization angles of FZHWs and DWSAs against the event back azimuths, and the difference between them. We do not observe clear deviation of FZHW polarizations from back azimuths. Instead, they have large scatters similar to these of DWSAs.

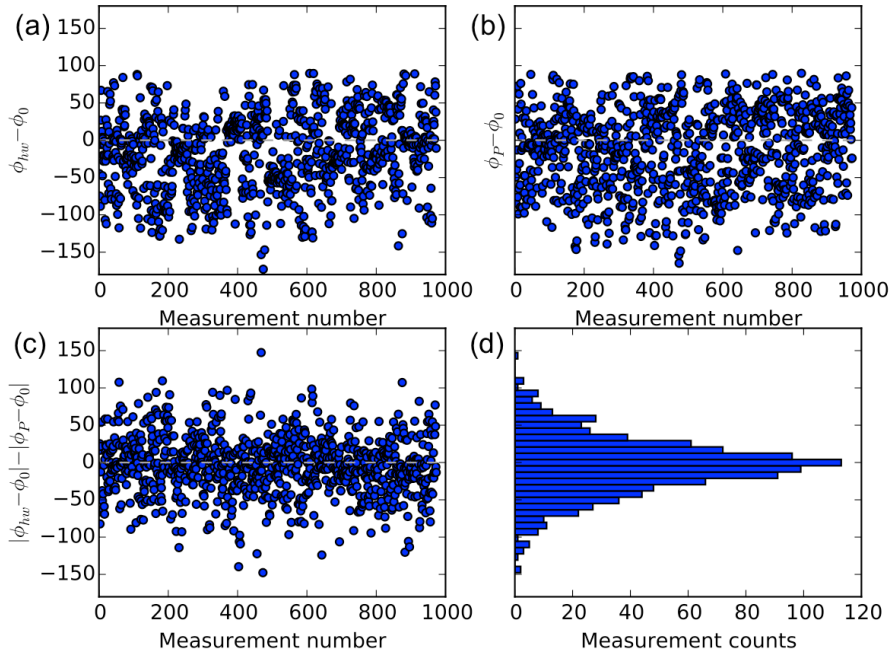

Figure 3.22 Statistical analysis of FZHW and DWSA polarization using automatic picks. (a) Polarization angle difference between FZHW and back azimuths for all measurements. (b) Polarization angle difference between DWSA and back azimuths for all measurements. (c) Comparison of deviation from back azimuth between FZHW and DWSA (see also Equation 14). (d) Histogram of (c).

Several possible factors may account for these observations. First, the amplitudes of FZHW and direct P waves on horizontal components are relatively low. Hence they

are likely contaminated by the pre-event noises. Secondly, assuming 10% average velocity contrast, the difference of polarization angles of FZHW and direct P waves is ~30 degrees theoretically. When projected to horizontal plane, this angle could become even smaller. Such a difference may not be resolvable with the presence of noise and other complex phases. Thirdly, fault zones are strongly heterogeneous and the structures are usually complicated than a two half spaces or sandwiched fault zone model [e.g., *Ben-Zion*, 1998]. In addition, depending on the frequency content, polarizations of FZHW and direct P waves may be sensitive to local structural complexities rather than the average velocity contrasts.

While individual picks, seismic profiles and velocity contrast pattern between automatic and manual results show general agreements, there are several notable issues that are worth discussing further. First, in the algorithm we used one average period T_d following the initial pick to check whether the first phase is sharp or not. This in fact sets a minimal value of velocity contrast below which we cannot resolve. Therefore, the use of T_d may reduce the resolution of the method. The obtained average value of T_d in our data set is ~0.06 s (6 samples), which corresponds to a minimal step of velocity contrast of 1-3%, depending on the P wave travel time. However, in practice it is always difficult to distinguish two phases if they are a few centiseconds apart. *Ross and Ben-Zion* [2014] also set a minimum allowed time difference between the initial and second pick to be 0.065 s in order to approximate the length of two wiggles of a direct P wave. Decreasing this value will increase the resolution of smaller velocity contrast but may introduce more false picks.

In addition to Parkfield, we also applied it in the Yushu region in northern Tibet

following the 2010 Mw6.9 Yushu earthquake, and we found general agreement between manual and automatic picks (figure S6 in *Yang et al.*, 2015). Therefore, we expect our method can be applied to identify FZHWs in large local earthquake data set with one or three component recordings. While in present FZHWs have been identified only in vertical strike-slip environment, it can be also applied to thrust or other tectonic environments [e.g., *Fukao et al.*, 1983].

Finally we list a few parameters that need be treated with precaution in the application of other regions. Firstly, T_d is calculated using the waveform within the search window. However, to avoid unfeasibly large value of T_d, it is useful to set an upper limit (e.g., 0.08 s to 0.1 s), depending somewhat on the sampling rate and dominant frequency content of the actual data. Secondly, the maximum allowed velocity contrast K_{max} also needs to be modified. In Parkfield, we use 15% based on previous observations. But this value could be different in other regions. One should note that a higher threshold might lead to detection of other phases that arrives at later times. If the priori estimate is unavailable, we recommend setting a relatively high value (e.g., 20%) in the initial stage. After obtaining the preliminary DWSA picks, one can estimate the velocity contrast for each single measurement using Equation 7. By checking the overall velocity contrast values, a proper value of K_{max} can be set to exclude outliers or other phases in the second run. The inaccuracy of first arrival picks will affect the DWSA picks and also lead to erroneous estimate of velocity contrast. This requires the input first arrivals to have relatively high quality. Hence, it is recommended to check the accuracy of first arrival picks whether they are from manual or automatic methods.

Table 3.2 Criteria for quality grade

Quality	Criteria for three-component measurement	Criteria for vertical component measurement
A	Satisfy polarity, period and polarization requirements. Peak LAAR and SAAR have the significant level greater five times standard deviation.	Satisfy polarity and period requirements. Peak LAAR and SAAR have the significant level greater five times standard deviation.
B	Not in A quality, but satisfy two of polarity, period and polarization requirements.	Not in A quality, but satisfy one of polarity and period requirements.
C	Not in A or B quality, but satisfy one of polarity, period and polarization requirements.	

CHAPTER 4. HIGH-RESOLUTION SEISMIC EVENT DETECTION WITH LARGE-N ARRAYS

The results presented in this chapter are from *Li et al.* [in prep].

Summary

We develop a novel method for seismic event detection that can be applied to large-N arrays. The method is based on a new detection function named local similarity, which quantifies the signal consistency between the examined station and its nearest neighbors. Using the 5200-station Long Beach nodal array, I demonstrate that stacked local similarity functions can be used to detect seismic events with amplitudes near or below noise levels, which is uncommon for regular detection methods and seismic arrays. I apply the method to one-week continuous data around the 03/11/2011 Mw 9.1 Tohoku-Oki earthquake, to detect local and distant events. In the 5-10 Hz range, I detect various events of natural and anthropogenic origins, but without a clear increase in local seismicity during and following the surface waves of the Tohoku-Oki mainshock. In the 1-Hz low-pass-filtered range, I detect hundreds of events, likely representing aftershocks from the Tohoku-Oki mainshock region. This new technique can be applied to both ultra-dense and regular array recordings for monitoring ultra-weak micro-seismicity and detecting unusual seismic events in noisy environments.

4.1 Introduction

Seismic arrays have provided important data for studying the Earth's structures and earthquake processes since the 1960s [*Rost and Thomas*, 2002]. Based on recordings from closely spaced uniform seismometers, various array methods can effectively enhance signal-to-noise ratios and significantly lower the detection threshold. Dense

regional networks such as the Japanese Hi-net array and the Southern California Seismic Network, as well as the recent US-Array, have been increasingly used to monitor regional seismicity in real time and provide high-quality earthquake catalogs. Dense arrays are also useful for detecting new types of seismic events such as deep tectonic tremor [*Obara*, 2002]. With advances in instrumentation technology, the density of seismometers in a given array has increased dramatically in the past decades. In the recent years, ultra-dense arrays with hundreds to thousands of sensors and tens- to hundred-meter interstation spacing have been deployed in several regions. One of the notable examples is the Long Beach 3D array, which contains 5200 sensors with 100 m spacing covering the urban area of the City of Long Beach [*Lin et al.*, 2013]. Such arrays, sometimes called large-N arrays, provide unprecedented detection capability for small magnitude earthquakes and other unconventional sources [*Inbal et al.*, 2015, 2016; *Riahi and Gerstoft*, 2015].

Apart from instrumentation technology, data processing methods also influence the resolution of seismic event detection. Traditional earthquake detection workflow includes phase picking (identifying impulsive arrivals of seismic phases) and phase association (grouping these phases into an individual event) [*Allen*, 1982]. Phase picking is commonly done by an energy detector such as short-term average over long-term average (STA/LTA) ratio [*Allen*, 1978; *Earle and Shearer*, 1994]. As computer power increases, many sophisticated detection algorithms have been proposed. Most of these algorithms continuously search over possible source locations by shifting and stacking waveforms or their variants (e.g., envelope, STA/LTA, normalized waveform). Notable examples include the source scanning algorithm [*Kao and Shan*, 2004], coalescence

microseismic mapping [*Drew et al.*, 2013], and backprojection [*Ishii et al.*, 2005; *Kiser and Ishii*, 2013].

Different from this category, template matching, or matched filter, takes advantage of predetermined events and cross-correlates them with continuous recordings to detect events with high waveform similarities [*Gibbons and Ringdal*, 2006]. This is based on the fact that nearby seismic events may have similar source mechanisms and ray paths, and hence similar waveforms. Template matching techniques have been widely applied to detect emergent tremors and small earthquakes, and usually detect new events at a factor of 5-10 times the original catalog [e.g., *Shelly et al.*, 2007; *Peng and Zhao*, 2009; *Yang et al.*, 2009]. However, template matching requires predetermined templates as inputs, which are not always available. In addition, it tends to detect events that are similar to templates, which may bias the detection results. An auto-detection technique could be used to build template events from scratch [*Brown et al.*, 2008]. However, with N^2 type scaling, this is computationally very intensive and hence cannot be applied to longer time series. Other approaches, such as finger-printing [*Yoon et al.*, 2015] or earthquake search-engines [*Zhang et al.*, 2014] have also been proposed for fast and robust detection of seismic events.

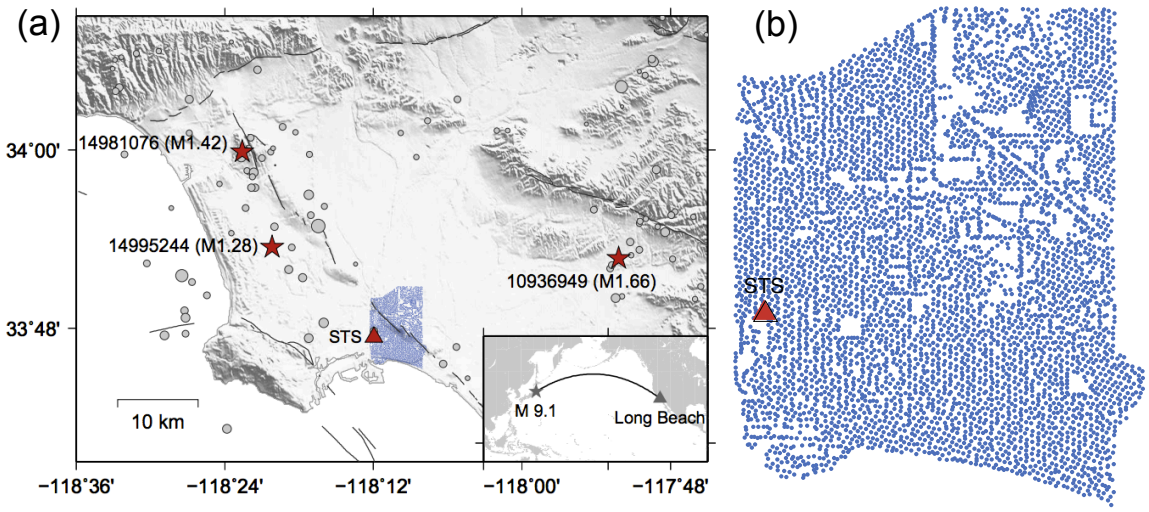

Figure 4.1 Map of study region, the Long Beach nodal array and local seismicity. (a) Blue dots are the 5200-sensor nodal array. A red triangle mark the broadband station STS belonging to Southern California Seismic Network (SCSN). Black curves denote the surface trace of mapped faults. Gray solid circles are seismicity listed in the SCSN catalog between January and June 2011, whose sizes are proportional to magnitude. Red stars mark three selected cataloged events used for tests. The inset map shows locations of the M 9.1 Tohoku-Oki earthquake and its ray path to Long Beach. (b) A zoom-in plot of the Long Beach array and the STS station.

The emergence of Large-N arrays provides unprecedented opportunities for resolving small events, but meanwhile poses new challenges for processing methods. Recent studies attempted to use advanced signal processing techniques, such as subarray analysis and graph clustering, to detect and locate sources within dense arrays [*de Groot-Hedlin*, 2015; *Riahi and Gerstoft*, 2017]. Here I introduce a new method that takes advantage of the primary features of emerging large-N arrays, i.e. a large number of sensors and short station spacing. The method involves a new metric termed local similarity. It evaluates the similarity on a given station with respect to its nearest neighbors. This is different from conventional metrics considering each station individually, or standard array processing methods that consider all stations together with

some general assumptions (e.g., plane waves; or wavefront with predicted arrivals) [*Rost and Thomas*, 2002].

I apply this method to one-week continuous data between 03/06/2011 and 03/12/2011 recorded by the 5200-station Long Beach array [*Lin et al.*, 2013]. The Long Beach array was deployed from January to June 2011 as part of a petroleum exploration survey, which contained 5200 geophones with 10-Hz corner frequency (Figure 4.1). This array covers 7×10 km in the city of Long Beach, with a nominal interstation distance of 100 m. Several segments of the Newport-Inglewood fault pass through this area. The 1933 Mw 6.4 Long Beach earthquake occurred about 10 km to the southeast of the array. Because the area is densely populated and the sensors were simply buried very close to the surface, the recordings are heavily contaminated by large-amplitude anthropogenic noise, which poses a challenge for seismic detection [*Inbal et al.*, 2015].

We choose this time period mainly because of the occurrence of the Mw 9.1 Tohoku-Oki earthquake on 03/11/2011. This event has triggered numerous microearthquakes and deep tectonic tremor around the world [*Gonzalez-Huizar et al.*, 2012], including the San Jacinto Fault in southern California [*Chao et al.*, 2013]. Systematical examination of remote triggering potential in California found that in addition to geothermal/volcanic regions, the Los Angeles basin has an unusually high triggering susceptibility compared to surrounding regions [*Van der Elst and Brodsky*, 2010]. Hence, it is reasonable to assume that the Tohoku-Oki mainshock may have triggered some microseismicity in this region, although these events may not be detected with conventional methods/arrays.

In the following sections, I first show that detecting events below noise level is feasible via direct stacking of local similarity. Then I perform a systematic comparison with template matching and STA/LTA. Finally I apply it to one week of continuous data of the Long Beach array to detect local and distant events, and examine whether the Tohoku-Oki mainshock may have triggered any significant increase of microseismicity in this region.

4.2 Methods

For a pair of two spatially close stations, the waveforms from any seismic source are nearly identical as the ray paths are very similar, while random noise at these sites remains sufficiently different. Hence in principle we can distinguish a signal from noise by measuring the waveform similarity on neighboring stations, which is termed local similarity (Figure 4.2a and 4.2b). Note that here we do not require waveform similarity across the whole network [e.g., *Rost and Thomas, 2002*; *Frank and Shapiro*, 2014]. Mathematically, local similarity at a master station is defined as the average of sliding-window normalized cross-correlations with its nearest neighbors. Each sliding time window is allowed to shift within a time lag relative to its neighbor recordings, in order to account for arrival time differences between neighboring stations. The peak cross-correlation function between a master station and a neighboring station is defined as

$$s_{ij}(t) = \max_{-L\le l\le L} \frac{\sum_{m=-M}^{M} u_i(t+m\delta)u_{ij}(t+m\delta+l\delta)}{\sqrt{\sum_{m=-M}^{M} u_i^2(t+m\delta)\sum_{m=-M}^{M} u_{ij}^2(t+m\delta+l\delta)}} \tag{16}$$

where u_i is the recording of the i^{th} master station, and u_{ij} is the recording of the j^{th} neighbor of the i^{th} master station, δ is the sampling interval, $(2M+1)\delta$ is the sliding window length, and $L\delta$ is the maximal time lag, which is determined by the upper limit of wave slowness and distance from the j^{th} neighboring station to the maser station i. In this study I set the sliding window length as 1 s and 3 s for the high-frequency (5-10 Hz) and long-period (< 1 Hz) signal, respectively. The peak correlation value within the time range is taken as the value for that sliding window. The resulting correlations between the master and its neighboring stations are averaged into a single one, termed the local similarity S_i (Equation 17):

$$S_i(t) = \frac{1}{K}\sum_{j=1}^{K} s_{ij}(t), \quad i = 1, 2, \dots, N; j = 1, 2, \dots, K \tag{17}$$

where K is the number of nearest neighbors, which is set by the user. Typically, I use four neighbors for a 2D array and two neighbors for a 1D array (Figure 4.2a).

The resulting average trace represents the signal resemblance of between the master station with respect to its neighbors in continuous time. After obtaining local similarity traces for all the stations, I directly stack them without any shifts to obtain a representative network trace, and perform event detection (Figure 4.2c). Direct stacking enables us to perform a general-purpose detection without knowing any wave types and velocity models in the study region.

Event detection in template matching is done by applying a common threshold to the network-stacked cross-correlation trace, which is generally defined as the median plus several times the median absolute deviation (MAD). Such thresholding is not suitable for

local similarity, because local similarity tends to have a fluctuating trend due to temporal drift in the similarity of background noise. To remove the long period trend, I first fit the trace with a tenth-order polynomial and subtract the fitting curve from the trace. After that, I apply a 1-minute sliding time window to select the outstanding peaks. For every window, the threshold is defined by the MAD and median calculated for that window. Statistically, a higher significance level suggests more stable detection and potentially fewer false alarms. I use the median plus 10 times MAD as the threshold for event detection in this study (Figure 4.2d).

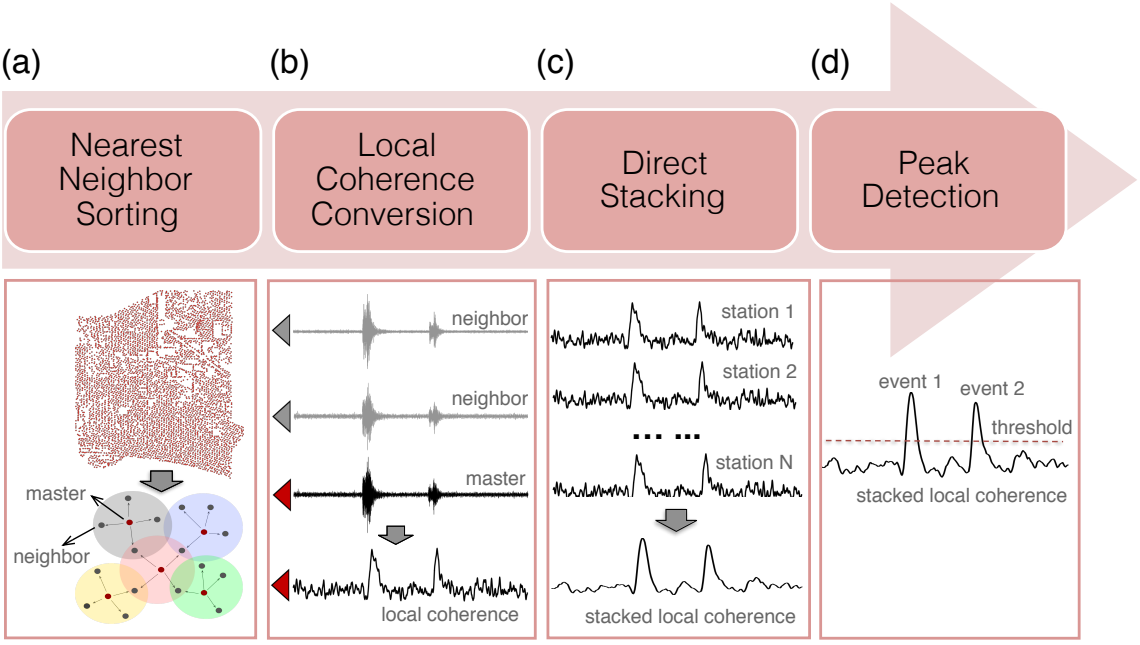

Figure 4.2 Flowchart and schematic diagrams of local similarity detection. (a) For each master station, find its nearest neighbors for local similarity computation. (b) Convert the seismic waveforms on the master station into local similarity by cross-correlation and averaging of those of its neighbors. (c) Stack local similarity of all stations. (d) Apply sliding-window threshold to select positive detections.

4.3 Results

4.3.1 Comparisons with STA/LTA, envelope function and template matching

I use three local events listed in the SCSN catalog (SCEC ID: 14995244, 10936949 and 14981076) to evaluate the performance of local similarity. I select these events because they are 20-50 km from the network (Figure 4.1) and have magnitude less than 2, so the waveforms recorded by the Long Beach array have very weak amplitudes. Figure 4.3a-c shows that the recordings are heavily contaminated by noise. I then examine how these events are manifested by local similarity, STA/LTA and envelope functions, respectively. For each method, I first convert the waveforms of individual stations into a metric function, and stack them into a network representative trace. For STA/LTA, I use 10 s for LTA and 1 s for STA. On the stacked trace, I measure the peak significance of the target event relative to the background level, which is defined as how many times the MAD above the median.

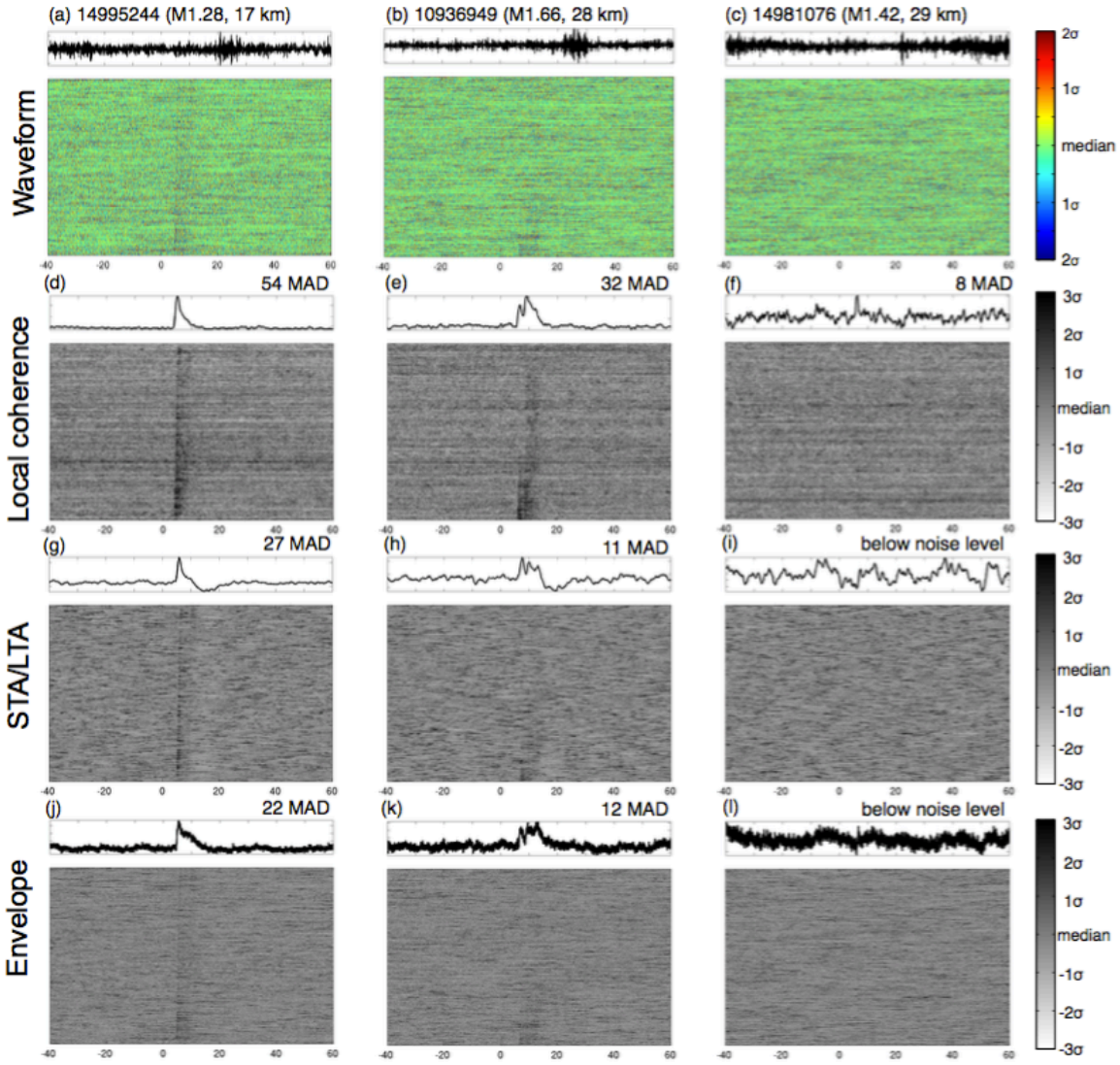

Figure 4.3 Performance tests of local similarity, short-term-average/long-term-average (STA/LTA), and envelope for three catalogued weak events. Traces along Y-axis are sorted by their epicentral distances. (a)-(c): raw waveforms of the events plotted in color for the Long Beach array. The upper curves in the box are raw recordings at station STS. Magnitude and distance from the array center are listed beside the event IDs. The waveforms are plotted according to their normalized amplitudes relative to the median. (d)-(g): local similarity corresponding the waveforms in (a)-(c). The black curves at the top are the stacked local similarity of the whole network. The significance levels of the peaks are marked. (g)-(i) and (j)-(l): for STA/LTA and envelope, respectively.

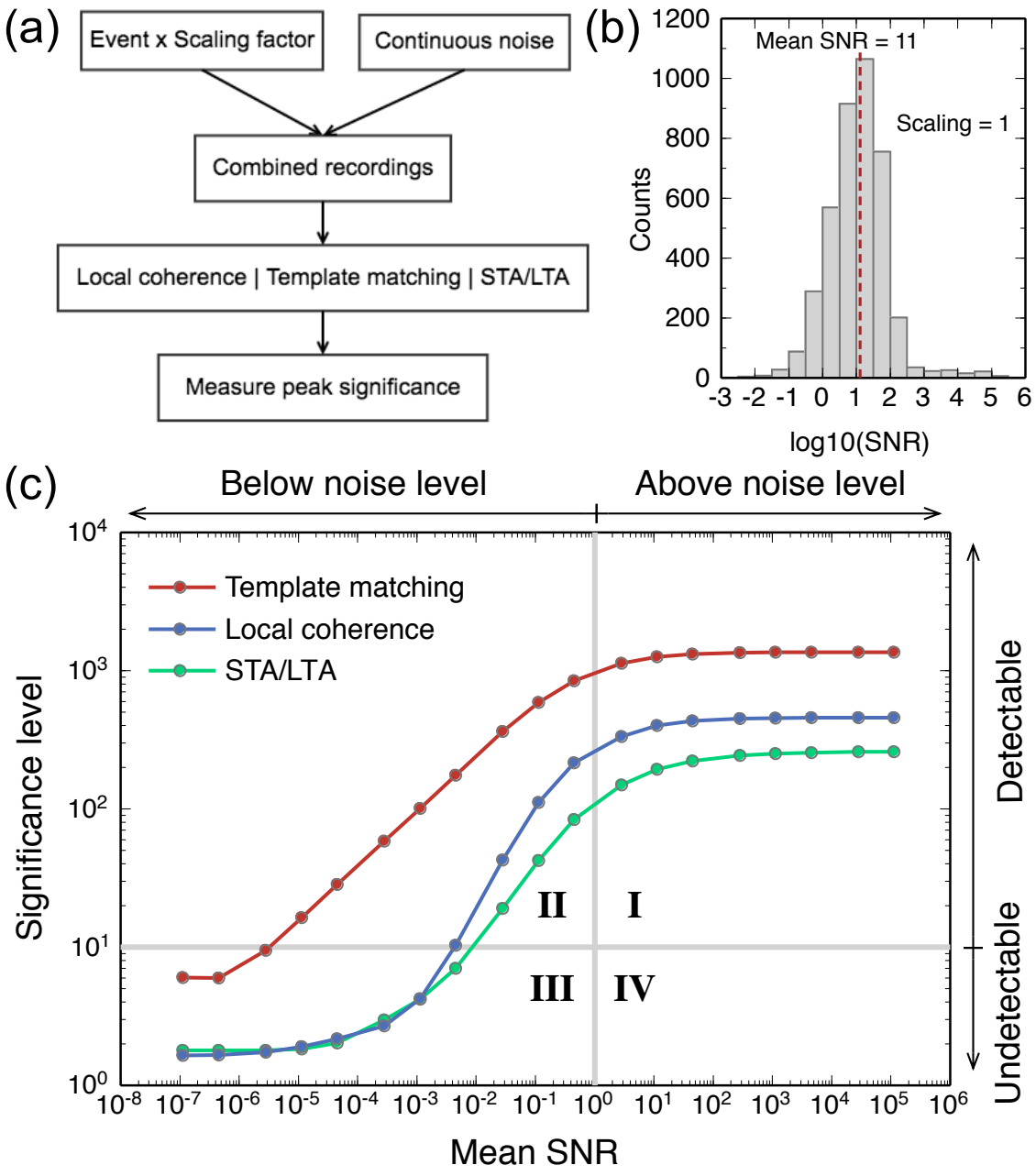

Figure 4.4 Synthetic test of detection performance of local similarity, template matching, and STA/LTA as a function of signal-to-noise ratio (SNR). (a) Flowchart of the synthetic test. Note event waveform is scaled by different factors to create recordings with different SNRs. (b) Histogram of SNR for 4000 stations when the scaling factor is 1. (c) Significance level versus SNR from local similarity, template matching, and STA/LTA. The vertical and horizontal gray lines mark SNR=1, and detection threshold=10 MAD, respectively.

Figure 4.3 shows that for the three target events, the results from STA/LTA are comparable to those from the envelope function. They both have reasonable peaks for events 14995244, 10936949, but do not show any patterns for event 14981076. In comparison, local similarity shows significant peaks for all three events, and has peak significance twice or more than that of STA/LTA and envelope. Thus local similarity produces more reliable detection than the other two metrics.

To further quantify their performances, I carry out synthetic tests with different signal-to-noise ratios (SNRs) for local similarity, STA/LTA, and template matching. Here I remove the envelope due to its comparable performance with STA/LTA and include template matching in the comparison. We note that because template matching uses prior information, i.e. known target waveforms, it should be treated as an optimal benchmark for the other two methods.

I generate synthetic data by following the below steps [*Li et al.*, 2015]: 1) select a local event with good SNR (ID 14930284, M 2.24), and multiply the waveforms by a scaling factor; 2) add the waveform on top of a randomly selected continuous noise at each station; 3) apply local similarity, STA/LTA and template matching method to the data obtained in step 2), resulting in a stacked trace; 4) measure the peak significance on the stacked trace at the time when the event is added. This process is outlined in Figure 4.4a. Note that the scaling factor is changed for every test to generate data with different SNRs. Here SNR is defined as the energy ratio between the added event waveforms and the continuous noise waveform. When the scaling factor is 1, the SNR distribution of 4053 stations has a mean SNR at 11, with a dominant range from 1 to 100 (Figure 4.4b). Different scaling factors can shift the SNR histogram systematically with different

amounts. Hence, the peak significance for each method is controlled mainly by the mean SNR (Figure 4.4c). As expected, template matching outperforms the other two methods. In this particular case, template matching has a detection capability down to SNR~10^{-5} if the threshold of positive detection is set at 10 MAD above the median. Local similarity, without requirement of any prior knowledge, can detect events down to SNR~0.01. It ranks the second and generally has the detection significance level twice above that of STA/LTA (except at very low SNRs), which is consistent with the tests using three catalog events (Figure 4.3). These results show that, our Large-N based method can well detect events far below noise level without prior information, which is significantly different from traditional methods and traditional arrays. Therefore I call such type of detection as high-resolution detection.

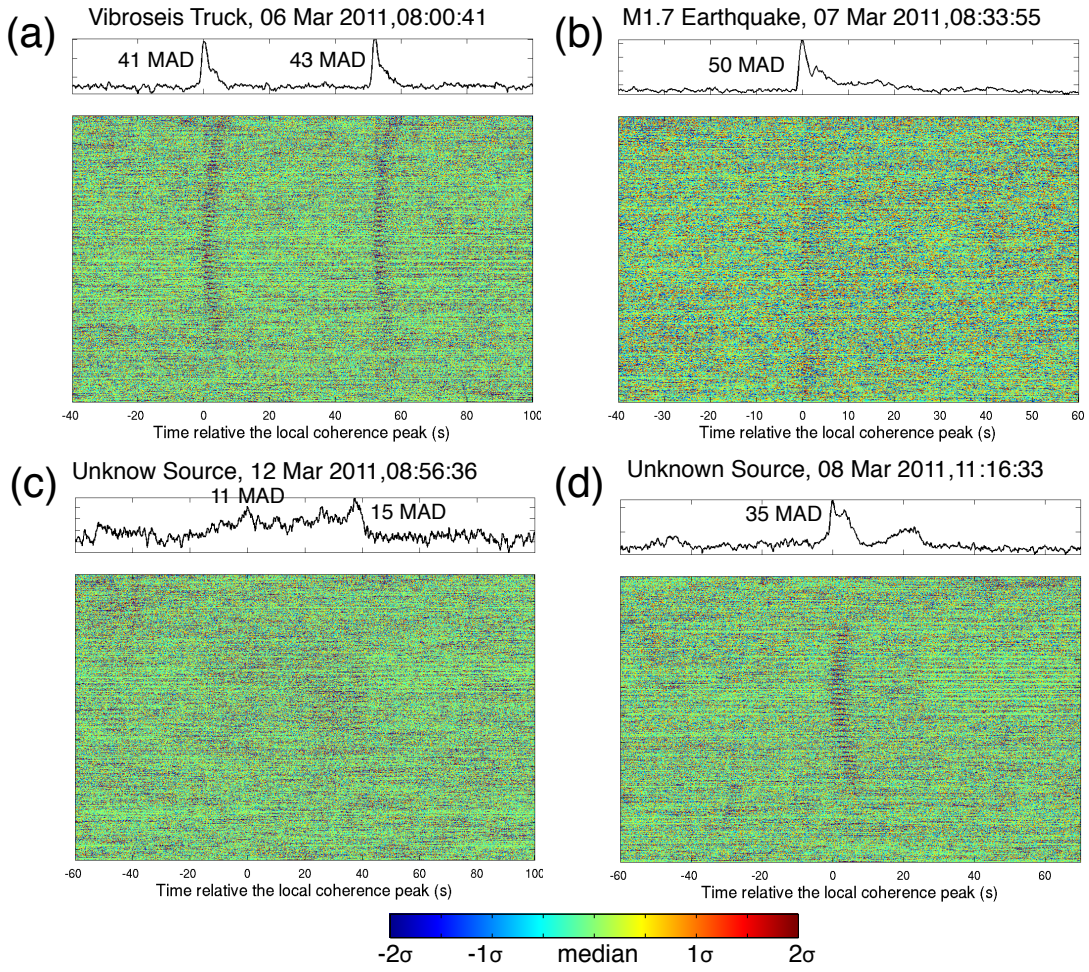

Figure 4.5 Detected examples of local events in 5-10 Hz filtered data. (a) Stacked local similarity trace and colormap of waveforms for two vibroseismic truck experiments. Denoted time on the title corresponds zero in time axis. (b) Detected nearby earthquake. (c) Unknown event, possibly associated with well injection. (d) Unknown event. The animations of these events can be found in the online supplementary material.

4.3.2 Detection of local and distant seismicity

I apply the method to the Long Beach data between 6 March 2011 and 12 March 2011, covering the 11 March 2011 Mw 9.1 Tohoku-Oki sequence. I examine two frequency ranges, 5-10 Hz and <1 Hz, in order to detect local and distant events, respectively. The detection threshold is set as 10 MAD above the median. In the 5-10 Hz range, I detect

451 events, whereas 401 are vibroseis truck signals from the petroleum survey. The vibroseis truck signals appear as sharp peaks in stacked local similarity with nearly every one-minute interval between 6 March and 9 March (Figure 4.5a, S 4.1). In the remaining 50 events, three are nearby earthquakes listed in the SCEC catalog, one of which is an M 1.7 event from ~200 km away (Figure 4.5b).

I also detect some weak but long-duration events up to a few minutes. One such event is very close to a possible injection well identified from Google map (Figure S 4.2; Personal communication with Philip Maechling). Although their waveform amplitudes were weak, we are able to observe the wavefield propagation in the animation and pinpoint the epicenter (Figure 4.5c). Apart from these events, many others are un-interpretable due to lack of additional information at this stage. Figure 4.5d shows an event with a sharp onset and a secondary phase, and then followed by an emergent wavetrain.

On the other hand, I detect 183 distant events in the < 1-Hz frequency range. 125 events occurred after the M 9.1 Tohoku earthquake and 101 matched with the earthquakes listed in the Japan Meteorological Agency (JMA) catalog. The events not matching the JMA catalog could be possibly missing aftershocks [*Kiser and Ishii*, 2013] or triggered seismicity elsewhere around the world [*Gonzalez-Huizar et al.*, 2012]. Figure 4.6 shows the detection of the aftershocks within two hours after the occurrence of the mainshock. From the recordings I observe three main events, corresponding to the M 9.1, M 7.6 and M 7.5 events in the JMA catalog and a few other weak events (Figure 4.6a). The stacked local similarity shows clear evidence of them and also many other smaller

events (Figure 4.6b). Our sliding-window threshold method detects 56 events from the stacked local similarity, including those buried in the coda of large events.

Finally, I also examine the number of local detection (in the frequency range of 5-10 Hz) 6 hours before and after the Tohoku-Oki mainshock, and find two and three events, respectively. However, none of them occurred during the passing surface waves of the mainshock. Hence, with our local similarity method, we are unable to observe any statistically significant change in local seismicity (Figure 4.6c-d) associated with the Tohoku-Oki mainshock.

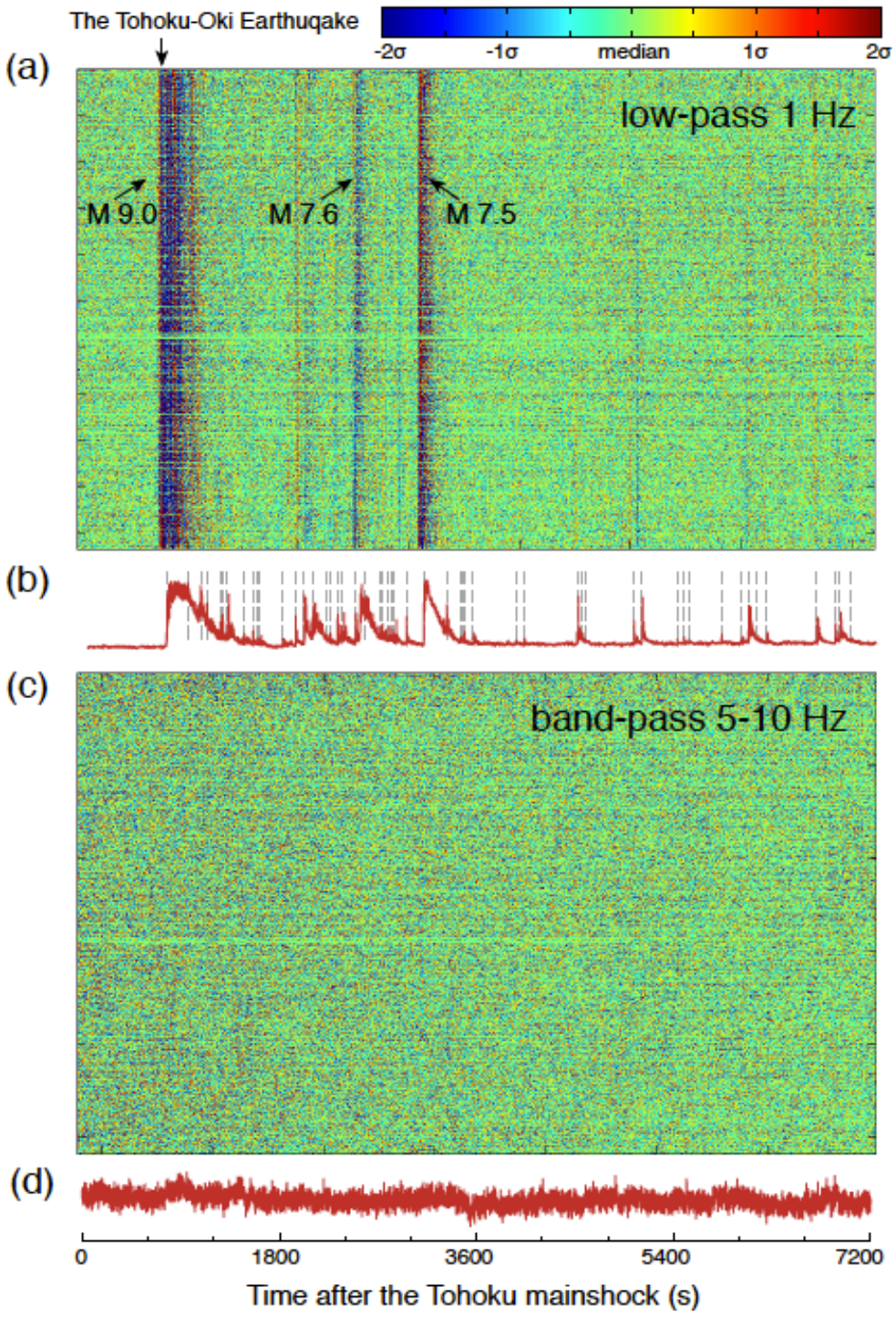

Figure 4.6 Waveforms and detection of two-hour Long Beach data after the Mw 9.1 Tohoku-Oki mainshock. (a) Lowpass 1 Hz waveforms recorded by the Long Beach array. (b) Stacked local similarity for lowpass 1 Hz data. The dashed gray lines mark the detected events. (c) Bandpass 5-10 Hz waveforms recorded by the Long

Beach array. (d) Stacked local similarity for bandpass 5-10 Hz data. Note that no significant peaks are observed on the trace.

4.4 Discussion

In this study I introduced a new metric named local similarity based on waveform similarity on spatially close stations for large-N arrays. By comparing a trace with those of neighboring stations, local similarity can effectively eliminate localized spikes that likely contaminate conventional amplitude-based metrics (e.g., envelope or STA/LTA). This feature enables us to detect very weak events (up to 0.01 SNR in this case) with data recorded in noisy environments. I applied this method to one week of continuous data during the 2011 Mw9.1 Tohoku-Oki mainshock. While I detected many distant events in the frequency range of < 1 Hz (most likely aftershocks), I did not observe any statistically significant change in events in the 5-10 Hz frequency range following the mainshock.

As shown in Figure 4.5, local similarity can identify both impulsive and emergent events, which renders broad applicability, e.g. short-duration regular earthquakes and long-duration tectonic/volcanic tremor. In addition, direct stacking removes any wave type assumption or velocity model dependence, making it useful for detecting both local and distant events. Hence, our method could be used for detecting new types of events, as demonstrated by those interesting local events detected in the 5-10 Hz range (Figure 4.5). However, direct stacking does not provide any locations or focal mechanisms. So additional methods are needed to further locate and classify event types. I note that when a certain type of events is targeted, a shift-stacking scheme can be applied to local similarity, such as used in the source-scanning algorithm [*Kao and Shan*, 2004]. With proper time shifts predicted by an assumed location and 1D velocity model [e.g., *Frank*

and Shapiro, 2014], stacking of local similarity is expected to be more constructive. For example, to detect local earthquake, I can apply theoretical travel time shifts of P (or S) waves to stack local similarity. This could result in a source-scanning-like or backprojection-like algorithm, but with local similarity rather than envelope or normalized waveforms.

Figure 4.4 shows an interesting relationship between SNR and detection significance. Traditional seismology mainly focuses on the events above the noise level, which falls in quadrant I (Figure 4.4c). Some studies using template matching have achieved the capability to detect events below noise level [*Schaff*, 2008]. However, it is unclear if events below noise level are detectable without known templates. Using local similarity applied to ultra-dense arrays, we are able to detect events in a wide range below noise levels with high confidence (quadrant II in Figure 4.4c).

Inbal et al. [2015, 2016] applied a backprojection method to 6-month recordings of the Long Beach array, and detected many seismic events in the midlower crust and upper mantle. To suppress local noise, they used downward continuation to back propagate the wavefield from surface to 5 km depth. In comparison, in this study I tested on one-week data only and used the original data without downward continuation. Our method at this point does not include a location module, and hence I do not have the accurate information on the depths of those detected events. However, by visually inspecting the animations (e.g., animations S1-S4), I find most of them likely have shallow origins instead of from low crust or upper mantle. I have checked and found that none of our detections matched with Inbal et al.'s [2016] in the examined one-week window. The difference may be mostly due to the aforementioned downward

continuation, which enhances detections of events at larger depths, but suppress detections of events less than 5 km.

Recent years have seen the exciting emergence of other dense nodal arrays like the Long Beach 3D array. Examples include the San Jacinto Fault in California [*Ben-Zion et al.*, 2015], Sweetwater in Texas, Mount St Helens in Washington [*Hansen and Schmandt*, 2015] and Piton de la Fournaise volcano in La Reunion [*Brenguier et al.*, 2016]. Our local similarity method could be potentially applied to these large-N datasets to detect weak and unknown seismic events. I note that the only requirement of this method is that the targeting signals on neighboring stations are more correlated than the background noise. Thus it does not require ultra-dense arrays with hundreds or thousands of stations. As long as the station spacing is comparable to or less than its wavelength, it can be applied to either 1D linear array or 2D array with only a few tens of stations. In fact, I have applied this method to the 1D Hi-CLIMB array across Himalaya and Southern Tibet, and the 2D PASO array (~60 stations) near Parkfield, and have detected many interesting local signals. Hence, this method could be applied for event detections with traditional arrays as well.

4.5 Supplementary figures

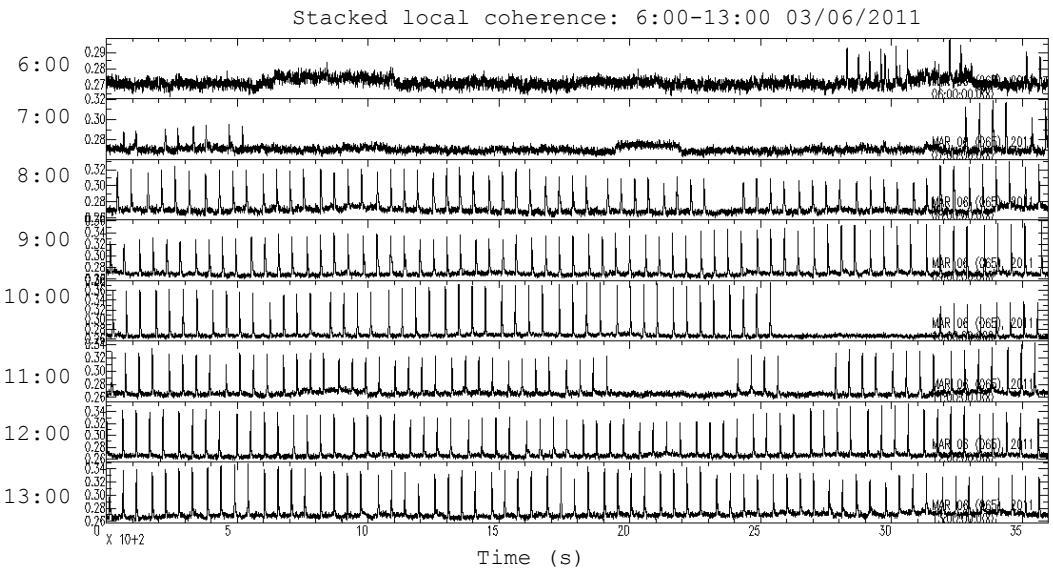

Figure S 4.1 Stacked local coherence for the hours with vibroseis truck experiments.

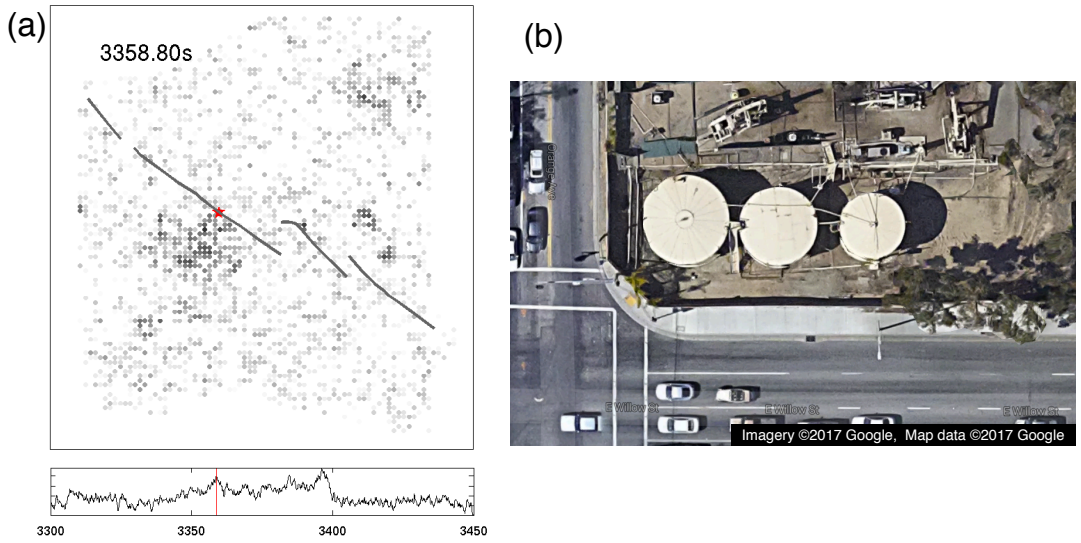

Figure S 4.2 Injection wells like facility possibly related with the detected event in Figure 4.4c. (a) A snapshot of the local coherence movie of the detected event. Red star mark the well location (33.80456, -118.17605) read in Google map. The gray line shows the Newport-Inglewood fault. Note the signal initiated near the well but then propagated southward. (b) Injection wells like facility observed from Google map.

CHAPTER 5. CONCLUSIONS

This thesis investigates three subjects in observational seismology, i.e., fault zone imaging, seismic event detection, and seismic phase picking. They all share the same feature, i.e., using automatic techniques to extract earthquake and structure information from big seismic data recorded by dense arrays. The work results in six publications, addressing specific topics in each paper.

In seismic anisotropy, I studied SWS phenomena using seismic arrays at multiple scales. In the SJFZ [*Li et al.*, 2015], I used five dense linear arrays crossing the SJFZ at different locations. Significant variations of fast directions observed on these arrays suggest that shallow fault structures and near-surface layers play important roles in controlling the SWS parameters. The other stations near the fault show clear contrast of fast directions between the SW and NE sides of the SJFZ. Stations on the SW side have fast directions consistent overall with SHmax, while stations on the NE side show mixed patterns likely reflecting lithological/topographic variations combined with fault zone damage.

The SWS work in the SJFZ successfully established a fully automatic flowchart to measure SWS parameters. Given that previous SWS results in southern California were rather the heterogeneous, I expanded SWS measurement to the entire SCSN in a two-decade period, in order to provide a uniform and complete database of SWS [*Li and Peng*, in prep]. The results show generally consistency of fast direction with SHmax in the region. However, I identified clear localized patterns of fast directions at tens-of-km scale. Specifically, fast directions within the same geological bodies tend to have a similar trend, indicating that localized structure and/or stress control shear anisotropy. Besides, I identified several regimes that have fast direction inconsistent with SHmax, including the SAF and other geological blocks. This work possibly provides the first map of structure- and stress- controlled anisotropy in southern California.

The SWS parameters are measured for station-event pairs and conventionally presented as average over individual stations. However, actual subsurface region of

shear-anisotropy remains unknown. In the NAF, I utilized a tomography method to map delay times into different depths [*Li et al.*, 2014]. Using the aftershock data from the 1999 Mw 7.4 İzmit and Mw 7.1 Düzce earthquakes, I observed a continuous belt–like highly anisotropic zone along the Karadere–Düzce branch of NAF, ~3 km wide and down to ~5 km deep. This observation provides strong evidence of shallow fault-zone shear-wave anisotropy caused by intense damage of rock materials from large earthquakes. However, this work is limited by simplified assumptions of anisotropy model and lack of consideration in fast directions. Better mapping of SWS parameters should take fast direction and complex anisotropy models into account, which remains a challenging topic in this area.

In addition to shear-wave anisotropy, I studied velocity contrast across fault wall using FZHWs. As mentioned before, velocity contrast plays a critical role in dynamic rupture, which may result in preferred rupture direction. In addition to traditional P/S-wave tomography methods that are sensitive to regional-scale structures, FZHWs provide high-resolution imaging of the immediate vicinity at a fault interface. However, in practice FZHWs are manually picked, which is not only laborious but also subjective. Therefore, I developed a method to automatically detect FZHWs [*Li and Peng*, 2016b]. I applied it to the Parkfield section of the San Andreas Fault and found many new FZHWs recorded by the stations near the Southwest Fracture Zone. These FZHWs could be generated within a relatively wide low-velocity zone sandwiched between the fast Salinian block on the southwest side and the slow Franciscan Mélange on the NE side.

I developed another automatic method to pick P and S phases of local earthquakes [*Li and Peng*, 2016a], which is a common task in seismological research. This new method incorporates 1D velocity inversion into phase picking. It first predicts phase arrivals using initial velocity models and available event locations, and then applies a detector function to search genuine phase arrivals around the initial predictions. This

strategy was proved successfully on both synthetic and real data sets. A Matlab package of this method has been released to the public and applied in several projects.

One of the emerging fields in seismology is the study of Large-N arrays, which can be considered as an extreme case of dense arrays. This new type of arrays provides an exceptional chance to study natural phenomena with resolution comparable to that in oil and gas exploration. However, we note that traditional techniques are no longer the most effective ways for processing these new data. Hence I developed a novel method for seismic event detection that fully takes advantage of large-N arrays. I proposed a new detection function named local similarity and demonstrated that stacked local similarity functions can detect seismic events with amplitudes near or below noise levels [*Li et al.*, in revision]. This new technique has great potential for monitoring ultra-weak micro-seismicity and detecting unusual seismic events in noisy environments.

REFERENCES

Abt, D., and K. Fischer (2008), Resolving Three-Dimensional Anisotropic Structure With Shear Wave Splitting Tomography, *Geophys. J. Int.*, 173, 859-886.

Aki, K., and W. Lee (1976), Determination of three-dimensional velocity anomalies under a seismic array using first P arrival times from local earthquakes: 1. A homogeneous initial model, *J. Geophys. Res.*, 81, 4381-4399, 1976.

Allam, A. A., and Y. Ben-Zion (2012), Seismic velocity structures in the southern California plate-boundary environment from double-difference tomography, *Geophys. J. Int.*, 190, 1181–1196.

Allam, A. A., Y. Ben-Zion, I. Kurzon, and F. Vernon (2014), Seismic velocity structure in the Hot Springs and trifurcation areas of the San Jacinto Fault Zone, California, from double-difference tomography, *Geophys. J. Int.*, 198(2), 978–999.

Allam, A. A., Y. Ben-Zion, and Z. Peng (2014), Seismic imaging of a bimaterial interface along the Hayward fault, CA, with fault zone head waves and direct P arrivals, *Pure App. Geophys.*, 171.

Allen, R. (1978), Automatic earthquake recognition and timing from single traces, *Bull. Seismol. Soc. Am.*, 68, 1521-1532.

Allen, R. (1982), Automatic phase pickers: their present use and future prospects, *Bull. Seism. Soc. Am.,* 72, S225-S242.

Alford, R. M. (1986), Shear data in presence of azimuthal anisotropy: *56th Ann. Internat. Mtg., Soc. Explor. Geophys.*, Expanded Abstract, 476-479.

Ampuero, J. P., and Y. Ben-Zion (2008), Cracks, pulses and macroscopic asymmetry of dynamic rupture on a bimaterial interface with velocity-weakening friction, Geophys. J. Int., 173, 674-692.

Aster, R. C., B. Borchers, and C. Thurber (2013). Parameter estimation and inverse problems (second edition). Boston: Elsevier, ISBN: 978-0-12-385048-5.

Aster, R. C. and P. M. Shearer (1992), Initial shear wave particle motions and stress constraints at the Anza Seismic Network, *Geophys. J. Int.*, 108, 740–748.

Aster, R. C., P. M. Shearer, and J. Berger (1990), Quantitative measurements of shear wave polarizations at the Anza seismic network, southern California: Implications for shear wave splitting and earthquake prediction, *J. Geophys. Res.*, 95, 12,449–12,473.

Aster, R., P. Shearer, P., and J. Berger (1991), Comment On Quantitative Measurements Of Shear-Wave Polarizations At The Anza Seismic Network, Southern California - Implications For Shear-Wave Splitting And Earthquake Prediction By Aster, Richard, C., Shearer, Peter, M., Berger, John - Reply, *J. Geophys. Res.,* 96, 6415-6419.

Audoine, E., M. Savage, K. Gledhill (2004), Anisotropic Structure Under A Back Arc Spreading Region, The Taupo Volcanic Zone, New Zealand, *J. Geophys. Res.-Solid Earth,* 109.

Audet, P. (2014), Layered crustal anisotropy aroung the San Andreas Faul near Parkfield, California, *J. Geophys. Res.*, 120(5), 3527–3543.

Baer, M., and U. Kradolfer (1987), An automatic phase picker for local and teleseismic events, *Bull. Seismol. Soc. Am.*, 77, 1437-1445.

Baillard, C., W. Crawford, V. Ballu, C. Hibert, and A. Mangeney (2014), An Automatic Kurtosis-Based P- and S-Phase Picker Designed for Local Seismic Networks, *Bull. Seismol. Soc. Am.*, 104Ro.

Balfour N.J., M. K. Savage, and J. Townend (2005), Stress and crustal anisotropy in Marlborough, New Zealand: evidence for low fault strength and structure-controlled anisotropy, *Geophys. J. Int.*, 163, 1073-1086.

Barruol, G., A. Deschamps, and O. Coutant (2004), Mapping upper mantle anisotropy beneath se france by sks splitting indicates neogene asthenospheric flow induced by apenninic slab roll-back and deflected by the deep alpine roots, *Tectonophysics*, 394, 125-138

Bellier, O., S. Over, A. Poisson, J. Andrieux (1997), Recent Temporal Change In The Stress State And Modern Stress Field Along The North Anatolian Fault Zone (Turkey), *Geophys. J. Int.,* 131, 61-86.

Ben-Zion, Y. (2001), Dynamic Ruptures In Recent Models Of Earthquake Faults, *Journal Of The Mechanics And Physics Of Solids*, 49, 2209-2244.

Ben-Zion, Y. (2006), Comment on "material contrast does not predict earthquake rupture propagation direction" by R. A. Harris and S. M. Day, *Geophys. Res. Lett.*, 33(13).

Ben-Zion, Y. (2008), Collective behavior of earthquakes and faults: Continuum-discrete transitions, progressive evolutionary changes, and different dynamic regimes, *Rev. Geophys.*, 46, RG4006.

Ben-Zion Y., and K. Aki (1990), Seismic radiation from an SH line source in a laterally heterogeneous planar fault zone, *Bull. Seism. Soc. Am.*, 80 971–994.

Ben-Zion, Y., S. Katz, and P. Leary (1992), Joint inversion of fault zone head waves and direct-P arrivals for crustal structure near major faults, *J. Geophys. Res.*, 97, 1943-1951.

Ben-Zion, Y., and P. Malin (1991), San-Andreas fault zone head waves near Parkfield, California, *Science*, 251, 1592-1594.

Ben-Zion, Y., Z. Peng, D. Okaya, L. Seeber, J. Armbruster, N. Ozer, A. Michael, S. Baris, M. Aktar, Y. Kuwahara, H. Ito (2003), A shallow fault-zone structure illuminated by trapped waves in the Karadere-Düzce branch of the North Anatolian Fault, western Turkey, *Geophys. J. Int.*, 152, 699-717.

Ben-Zion, Y. and CSammis, C (2003). Characteristics of fault zones, *Pure appl. geophys.*, 160, 677.

Ben-Zion, Y., Z. Shi (2005), Dynamic rupture on a material interface with spontaneous generation of plastic strain in the bulk, *Earth Planet. Sci. Lett*., 236, 486-496.

Ben-Zion, Y., F. Vernon, Y. Ozakin, D. Zigone, Z. Ross, H. Meng, M. White, J. Reyes, D. Hollis, and M. Barklage (2015), Basic data features and results from a spatially dense seismic array on the San Jacinto fault zone, *Geophys. J. Int.,* 202, 370–380.

Bennington, N., C. Thurber, and S. Roecker (2008), Three-dimensional seismic attenuation structure around the SAFOD site, Parkfield, California, *Bull. Seismol. Soc. Am.*, 98(6), 2934-2947.

Bennington, N. L., C. Thurber, Z. G. Peng, H. J. Zhang, and P. Zhao (2013), Incorporating fault zone head wave and direct wave secondary arrival times into seismic tomography: Application at Parkfield, California, *J. Geophys. Res.*, 118(3), 1008-1014.

Blanpied, M., D. Lockner, J. Byerlee (1991), Fault stability inferred from granite sliding experiments at hydrothermal conditions, *Geophys. Res. Lett.,* 18, 609-612.

Boness, N., and M. Zoback (2006), Mapping stress and structurally controlled crustal shear velocity anisotropy in California, *Geology*, 34, 825-828.

Booth, D.C., and S. Crampin (1985), Shear-wave polarizations on a curved wavefront at an isotropic free-surface, *Geophys. J. R. Astron. Soc.*, 83, 31-45.

Brenguier, F., P. Kowalski, N. Ackerley, N. Nakata, P. Boué, M. Campillo, E. Larose, S. Rambaud, C. Pequegnat, T. Lecocq, P. Roux, V. Ferrazzini, N. Villeneuve, N. M. Shapiro, J. Chaput (2016), Toward 4D Noise-Based Seismic Probing of Volcanoes: Perspectives from a Large-N Experiment on Piton de la Fournaise Volcano, *Seismol. Res. Lett.*, 87(1), 15-25.

Brown, J. R., G. C. Beroza, and D. R. Shelly (2008), An autocorrelation method to detect low frequency earthquakes within tremor, *Geophys. Res. Lett.*, 35, L16305, doi:10.1029/2008GL034560.

Bulut, F., Y. Ben-Zion, M. Bohnhoff (2012), Evidence for a bimaterial interface along the Mudurnu segment of the North Anatolian Fault Zone from polarization analysis of P waves, *Earth Planet. Sci. Lett.*, 327, 17-22.

Burgmann, R., S. Ergintav, P. Segall, E. Hearn, S. McClusky, R. Reilinger, H. Woith, J. Zschau (2002) Time-dependent distributed afterslip on and deep below the Izmit earthquake rupture, *Bull. Seismol. Soc. Am.*, 92, 126-137.

Chao, K., Z. Peng, H. Gonzalez-Huizar, C. Aiken, B. Enescu, H. Kao, A. A. Velasco, K. Obara and T. Matsuzawa (2013), A global search of triggered tremor following the 2011 Mw9.0 Tohoku-Oki earthquake, *Bull. Seismol. Soc. Am.*, 103(2b), 1551-1570.

Cochran, E., Y. Li, P. Shearer, S. Barbot, Y. Fialko, J. Vidale (2009), Seismic and geodetic evidence for extensive, long-lived fault damage zones, *Geology*, 37, 315-318.

Cochran, E.S., Y.-G. Li, and J.E. Vidale (2006), Anisotropy in the shallow crust observed around the San Andreas Fault before and after the 2004 M6 Parkfield earthquake, *Bull. Seism. Soc. Am.*, 96(4B), S364–S375.

Cochran, E. S., J. E. Vidale, and Y.-G. Li (2003), Near-fault anisotropy following the Hector Mine earthquake, *J. Geophys. Res.*, 108(B9), 2436.

Crampin, S. (1987), A review of extensive-dilatancy anisotropy (EDA) in hydrocarbon reservoirs, *Geophysical Journal of the Royal Astronomical Society*, 89, 463-463.

Crampin, S. (1990), Seismic Anisotropy In The Earths Crust - A Citation-Classic Commentary On A Review Of Wave Motion In Anisotropic And Cracked Elastic-Media By Crampin,S., Current Contents. *Physical Chemical and Earth Sciences*, 18-18.

Crampin, S., (1991), Seismic Anisotropy Due To Preferred Mineral Orientation Observed In Shallow Crustal Rocks In Southern Alaska - Comment, *Geology*,19, 859-859.

Crampin, S., D. Bamford, and R. Mcgonigle (1978), Estimating Crack Parameters By Inversion Of P Wave Velocity-Anisotropy, *Geophysical Journal of the Royal Astronomical Society*, 53, 173-173.

Crampin, S., D. C. Booth, R. Evans, S. Peacock, and J. B. Fletcher (1990), Change in shear wave splitting at Anza near the time of the North Palm Springs earthquake, *J. Geophys. Res.*, 95, 11, 197–11, 212.

Crampin, S., and D. Booth (1985), Shear-Wave Polarizations Near The North Anatolian Fault .2. Interpretation In Terms Of Crack-Induced Anisotropy, *Geophysical Journal of the Royal Astronomical Society*, 83, 75-92.

Crampin, S., D. Booth, R. Evans, S. Peacock, and J. Fletcher (1991), Comment on quantitative measurements of shear-wave polarizations at the Anza seismic network, southern California - implications for shear-wave splitting and earthquake prediction by

Aster, Richard, C., Shearer, Peter, M., And Berger, John. *J. Geophys. Res.-Solid Earth and Planets*, 96, 6403-6414.

Crampin, S. and Y., Gao (2004), Comment on "Systematic Analysis of Shear-Wave Splitting in the Aftershock Zone of the 1999 Chi-Chi, Taiwan, Earthquake: Shallow Crustal Anisotropy and Lack of Precursory Variations " by Liu, Teng and Ben-Zion, *Bull. Seism. Soc. Am*.

Dieterich, J. (1979), Modeling of rock friction .1. Experimental results and constitutive equations, *J. Geophys. Res.*, 84, 2161-2168.

Dai, H., and C. MacBeth (1997), The application of back-propagation neural network to automatic picking seismic arrivals from single-component recordings, *J. Geophys. Res.*, 102.

Dalguer, L. A., and S. M. Day (2007), Staggered-grid split-node method for spontaneous rupture simulation, *J. Geophys. Res.*, 112.

Diehl, T., E. Kissling, S. Husen, and A. Aldersons (2009), Consistent phase picking for regional tomography models: application to the greater Alpine region, *Geophys. J. Int.,* 176, 542-554.

Dieterich, J. H. (1979), Modeling of rock friction .1. Experimental results and constitutive equations, *J. Geophys. Res.*, 84, 2161-2168

Dor, O., T. K. Rockwell, and Y. Ben-Zion (2006), Geologic observations of damage asymmetry in the structure of the San Jacinto, San Andreas and Punchbowl faults in southern California: A possible indicator for preferred rupture propagation direction, *Pure Appl. Geophys.*, 163, 301–349.

Drew, J., White, R. S., Tilmann, F., and Tarasewicz, J. (2013), Coalescence microseismic mapping, *Geophys. J. Int.*, 195, 1773–1785.

Earle, P. S., and P. M. Shearer (1994), Characterization of global seismo- grams using an automatic picking algorithm, *Bull. Seismol. Soc. Am.,* 84, 366–376.

Earle, P. S., S. Rost, P. M. Shearer, and C. Thomas (2011), Scattered P'P' waves observed at short distances, *Bull. Seismol. Soc. Am.*, 101, 2843-2854.

Eberhart-Phillips, D. M., A.J. (1993), Three-dimensional velocity structure, seismicity, and fault structure in the Parkfield region, central California, *J. Geophys. Res.*, 98, 15737-15758.

Eken, T., M. Bohnhoff, F. Bulut, B. Can, and M. Aktar (2013), Crustal Anisotropy in the Eastern Sea of Marmara Region in Northwestern Turkey, *Bull. Seism. Soc. Am.*, 103, 911-924.

Evans, R., S. Crampin, and D. Booth (1985), Shear-wave polarizations .1. Observations Near The North Anatolian Fault (NAF), *Geophysical Journal of the Royal Astronomical Society*, 81, 340-341.

Finzi, Y., E. H. Hearn, Y. Ben-Zion and V. Lyakhovsky (2009), Structural properties and deformation patterns of evolving strike-slip faults: Numerical simulations incorporating damage rheology, *Pure Appl. Geophys.*, 166, 1537–1573.

Fischer, K., E. Parmentier, A. Stine, and E. Wolf (2000), Modeling anisotropy and plate-driven flow in the Tonga subduction zone back arc, *J. Geophys. Res.-Solid Earth* 105, 16181-16191.

Fialko, Y. (2006), Interseismic strain accumulation and the earthquake potential on the southern San Andreas Fault System, *Nature*, 441, 968–971.

Filson, J. (1975), Array seismology, *Ann. Rev. Earth Planet. Sci.*, 3, 157-181.

Fouch, M., K. Fischer, E. Parmentier, M. Wysession, and T. Clarke (2000), Shear wave splitting, continental keels, and patterns of mantle flow, *Journal of Geophysical Research-Solid Earth*, 105, 6255-6275.

Frank, W. B., and N. M. Shapiro (2014), Automatic detection of low-frequency earthquakes (LFEs) based on a beamformed network response, *Geophys. J. Int.*, 197, 1215–1223.

Fukao, Y., S. Hori, and M. Ukawa (1983), A seismological constraint on the depth of the basalt-eclogite transition in a subducting oceanic crust, *Nature*, 303, 413-415.

Fukao, Y. (1984), Evidence from core-reflected shear-waves for anisotropy in the earth's mantle, *Nature*, 309, 695-698.

Gentili, S., and A. Michelini (2006), Automatic picking of P and S phases using a neural tree, *J. Seismol.*, 10, 39-63.

Gerst, A., and M. Savage (2004), Seismic anisotropy beneath Ruapehu volcano: a possible eruption forecasting tool, *Science*, 306 (2004), pp. 1543–1547.

Gibbons, S. J., and F. Ringdal (2006), The detection of low magnitude seismic events using array-based waveform correlation, *Geophys. J. Int.*, 165, 149–166.

Godfrey, H. J., A. Shelley, and M. K. Savage (2014), Search for Temporal Changes in Shear-Wave Splitting Associated with the 2012 Te Maari Eruptions at Mount Tongariro, New Zealand, *Journal of Volcanology and Geothermal Research*, 286: 277-93.

Gonzalez-Huizar, H., A. A. Velasco, Z. Peng and R. Castro (2012), Remote triggered seismicity caused by the 2011, M9.0 Tohoku-Oki, Japan earthquake, *Geophys. Res. Lett.*, 39, L10302.

Görgün, E., M. Bohnhoff, F. Bulut, and G. Dresen (2010), Seismotectonic setting of the Karadere-Düzce branch of the North Anatolian Fault Zone between the 1999 Izmit and Düzce ruptures from analysis of Izmit aftershock focal mechanisms, *Tectonophysics*, 482, 170-181.

Gulen, L., A. Pinar, D. Kalafat, N. Ozel, G. Horasan, M. Yilmazer, A. Isikara (2002), Surface fault breaks, aftershock distribution, and rupture process of the 17 August 1999 Izmit, Turkey, earthquake, *Bull. Seismol. Soc. Am.*, 92, 230-244.

Hamiel, Y, V. Lyakhovsky, S. Stanchits, G. Dresen, and Y. Ben-Zion (2009), Brittle Deformation and Damage-Induced Seismic Wave Anisotropy in Rocks, *Geophys. J. Int.*, 178, 901–909.

Hansen, S. M. and B. Schmandt (2015), Automated detection and location of microseismicity at Mount St. Helens with a large-N geophone array, *Geophys. Res. Lett.*, 42, 7390–7397.

Harris, R. A., and S. M. Day (2005), Material contrast does not predict earthquake rupture propagation direction, *Geophys. Res. Lett.*, 32.

Hauksson, E., W. Yang, and P. M. Shearer (2012), Waveform relocated earthquake catalog for Southern California (1981 to June 2011), *Bull. Seismol. Soc. Am.*, 102(5), 2239–2244.

Hillers, G., Y. Ben-Zion, M. Landès and M. Campillo (2013), Interaction of microseisms with crustal heterogeneity: A case study from the San Jacinto fault zone area, *Geochem. Geophys. Geosyst.*, 14, 2063–2545.

Hartleb, R., J. Dolan, H. Akyuz, T. Dawson, A. Tucker, B. Yerli, T. Rockwell, E. Toraman, Z. Cakir, A. Dikbas, and E. Altunel (2002), Surface rupture and slip distribution along the Karadere segment of the 17 August 1999 Izmit and the western section of the 12 November 1999 Düzce, Turkey, earthquakes, *Bull. Seismol. Soc. Am.*, 92, 67-78.

Haslinger, F., E. Kissling, J. Ansorge, D. Hatzfeld, E. Papadimitriou, V. Karakostas, K. Makropoulos, H. Kahle, and Y. Peter (1999), 3D crustal structure from local earthquake tomography around the Gulf of Arta (Ionian region, NW Greece), *Tectonophysics*, 304, 201-218.

Holt, R., M. Savage, J. Townend, E. Syracuse, and C. Thurber (2013), Crustal stress and fault strength in the Canterbury Plains, New Zealand, *Earth Planet. Sci. Lett.*, 383, 173-181.

Hong, T.-K. and W. Menke (2006), Tomographic investigation of the wear along the San Jacinto fault, southern California, *Phys. Earth Planet. In.*, 155, 236-248.

Hurd, O., M. Bohnhoff (2012), Stress- and Structure-Induced Shear-Wave Anisotropy along the 1999 Izmit Rupture, Northwest Turkey, *Bull. Seismol. Soc. Am.*, 102, 2177-2188.

Husen, S., E. Kissling, E. Flueh (2000), Local earthquake tomography of shallow subduction in north Chile: A combined onshore and offshore study, *Journal of Geophysical Research-Solid Earth*, 105, 28183-28198.

Inbal, A., R. W. Clayton, and J. P. Ampuero (2015), Imaging widespread seismicity at midlower crustal depths beneath Long Beach, CA, with a dense seismic array: Evidence for a depth-dependent earthquake size distribution, *Geophys. Res. Lett.,* 42, 6314–6323.

Inbal, A., J. P. Ampuero, and R. W. Clayton (2016), Localized seismic deformation in the upper mantle revealed by dense seismic arrays, *Science*, 354 (6308), pp. 88–92.

Ishii, M., P.M. Shearer, H. Houston, and J. E. Vidale (2005), Extent, duration and speed of the 2004 Sumatra-Andaman earthquake imaged by the Hi-Net array, *Nature*, 435, 933–936.

Jurkevic, A. (1988), Polarization analysis of three-component array data, *Bull. Seismol. Soc. Am.*, 78, 871-884.

Kao, H., and S. J. Shan (2004), The Source-Scanning Algorithm: Mapping the distribution of seismic sources in time and space, *Geophys. J. Int.*, 157, 589–594.

Kiser, E., and Ishii, M. (2013), Hidden aftershocks of the 2011 Mw 9.0 Tohoku, Japan earthquake imaged with the backprojection method, *J. Geophys. Res. Solid Earth,* 118, 5564–5576.

Koulakov, I., D. Bindi, S. Parolai, H. Grosser, C. Milkereit (2010), Distribution of Seismic Velocities and Attenuation in the Crust beneath the North Anatolian Fault (Turkey) from Local Earthquake Tomography, *Bull. Seismol. Soc. Am.*, 100, 207-224.

Kuperkoch, L., T. Meier, J. Lee, W. Friederich, and EGELADOS Working Group (2010). Automated determination of P-phase arrival times at regional and local distances using higher order statistics, *Geophys. J. Int.*, 181, 1159-1170.

Kurzon, I., F. L. Vernon, Y. Ben-Zion, and G. Atkinson (2014), Ground motion prediction equations in the San Jacinto Fault Zone— significant effects of rupture directivity and fault zone amplification, *Pure Appl. Geophys.*, 171, 3045–3081.

Leary, P., S. Crampin, T. McEvilly (1990), Seismic fracture anisotropy in the earth's crust - an overview, *Journal of Geophysical Research - Solid Earth and Planets*, 95, 11105-11114.

Leonard, M., and B.L.N. Kennett (1999), Multi-component autoregressive techniques for the analysis of seismograms, *Phys. Earth. Planet. Int.,* 113, 247-263.

Lewis, M. A., and Y. Ben-Zion (2010), Diversity of fault zone damage and trapping structures in the Parkfield section of the San Andreas fault from comprehensive analysis of near fault seismograms, *Geophys. J. Int.*, 183(3), 1579-1595.

Lewis, M. A., Z. G. Peng, Y. Ben-Zion, and F. L. Vernon (2005), Shallow seismic trapping structure in the San Jacinto Fault Zone near Anza, California, *Geophys. J. Int.*, 162, 867–881.

Li, Y., P. Chen, E. Cochran, J. Vidale, T. Burdette (2006), Seismic evidence for rock damage and healing on the San Andreas fault associated with the 2004 M 6.0 Parkfield earthquake, *Bull. Seismol. Soc. Am.*, 96, S349-S363.

Li, Y. G., T. L. Teng, and T. L. Henyey, (1994), Shear-wave splitting observations in the northern Los Angeles basin, California, *Bull. Seismol. Soc. Am.*, 84, 307–323.

Li, Y. G., J. E. Vidale, and E. S. Cochran (2004), Low-velocity damaged structure of the San Andreas fault at Parkfield from fault zone trapped waves, *Geophys. Res. Lett.*, 31(12).

Li, Z., and Z. Peng, Two decades of shear-wave splitting measurements in southern California, *in prep*.

Li, Z., Z. Peng, and D. Hollis, High-resolution seismic event detection using local similarity for ultra-dense arrays, *Sci. Rep.*, in revision.

Li, Z., and Z. Peng, (2016a), A predict-and-search strategy for picking P and S phases: signal-to-noise ratio detector joint with one-dimensional velocity model inversion, *Seismol. Res. Lett.*, 86(2B), 731.

Li, Z., and Z. Peng (2016b), Automatic identification of fault zone head waves and direct P waves and its application in the Parkfield section of the San Andreas Fault, California, *Geophys. J. Int.*, 250, 1326-1341.

Li, Z., Z. Peng, Y. Ben-Zion, and F. Vernon (2015), Spatial variations of shear-wave anisotropy near the San Jacinto Fault Zone in southern California, *J. Geophys. Res. Solid Earth*, 120.

Li, Z., Z. Peng, X. Meng, A. Inbal, Y. Xie, D. Hollis, and J.-P. Ampuero (2015), Matched Filter Detection of Microseismicity in Long Beach with a 5200-station Dense Array. *SEG Technical Program Expanded Abstracts 2015*: pp. 2615-2619.

Li, Z., H. Zhang, and Z. Peng (2014), Structure-controlled seismic anisotropy along the Karadere–Düzce branch of the North Anatolian Fault revealed by shear-wave splitting tomography, *Earth Planet. Sci. Lett.*, 391 (2014), pp. 319–326.

Lin, F.-C., D. Li, R. W. Clayton, and D. Hollis (2013), High-resolution 3D shallow crustal structure in Long Beach, California: Application of ambient noise tomography on a dense seismic array, *Geophysics*, 78(4), Q45–Q56.

Liu, E., J. Queen, X. Li, M. Chapman, S. Maultzsch, H. Lynn, E. Chesnokov (2003), Observation and analysis of frequency-dependent anisotropy from a multicomponent VSP at Bluebell-Altamont Field, Utah, *Journal of Applied Geophysics*, 54, 319-333.

Liu, Y., T. Teng, and Y. Ben-Zion (2004), Systematic analysis of shear-wave splitting in the aftershock zone of the 1999 Chi-Chi, Taiwan, earthquake: Shallow crustal anisotropy and lack of precursory variations, *Bull. Seismol. Soc. Am.*, 94, 2330-2347.

Liu, Y., Y. Ben-Zion, and T. L. Teng (2005), Reply to Comment of Crampin and Gao on "Systematic Analysis of Shear-Wave Splitting in the Aftershock Zone of the 1999 Chi-Chi, Taiwan, Earthquake: Shallow Crustal Anisotropy and Lack of Precursory Variations "by Liu, Teng and Ben-Zion, *Bull. Seismol. Soc. Am.*, 95, 361-366.

Liu Y., H. Zhang, C. Thurber (2008), Roecker S. Shear wave anisotropy in the crust around the San Andreas fault near Parkfield: spatial and temporal analysis, *Geophys. J. Int.*, 172, 957-970.

Long, M.D., and P. G. Silver (2009), Shear wave splitting and mantle anisotropy: measurements, interpretations, and new directions, *Surv. Geophys.*, 30, 407.

Magistrale, H., K. McLaughlin, and S. Day (1996), A geology based 3-D velocity model of the Los Angeles basin sediments, *Bull. Seismol. Soc. Am.*, 86, 1161-1166.

Marone, C., C. Scholz (1988), The depth of seismic faulting and the upper transition from stable to unstable slip regimes, *Geophys. Res. Lett.*, 15, 621-624.

McGuire, J., and Y. Ben-Zion (2005), High-resolution imaging of the bear valley section of the San Andreas fault at seismogenic depths with fault-zone head waves and relocated seismicity, *Geophys. J. Int.*, 163, 152-164.

McNamara, D. E., L. Gee, H. M. Benz, and M. Chapman (2014), Frequency-dependent seismic attenuation in the eastern united states as observed from the 2011 central virginia earthquake and aftershock sequence edited, *Bull. Seismol. Soc. Am.*, 102, 55-72.

Meng, L., J.-P. Ampuero, J. Stock, Z. Duputel, Y. Luo, V. C. Tsai (2012), Earthquake in a maze: compressional rupture branching during the 2012 Mw 8.6 Sumatra Earthquake, *Science*, 337, 724.

Michael and Eberhart-Phillips (1991), Relations among fault behavior, subsurface geology, and three-dimensional velocity models, Science, 253, 5020.

Najdahmadi, B., M. Bohnhoff, and Y. Ben-Zion (2016), Bimaterial interfaces at the Karadere segment of the North Anatolian Fault, northwestern Turkey, *J. Geophys. Res. Solid Earth*, 121, 931–950

Nur, A. and G. Simmons (1969), Stress-induced velocity anisotropy in rock: An experimental study, *J. Geophys. Res.*, 74(27), 6667–6674.

Obara, K. (2002), Nonvolcanic deep tremor associated with subduction in southwest Japan, *Science*, 296, 1679–81.

Olsen, K. B., S. M. Day, J. B. Minster, Y. Cui, A. Chourasia, M. Faerman, R. Moore, P. Maechling, and T. Jordan (2006), Strong shaking in Los Angeles expected from southern San Andreas earthquake, *Geophys. Res. Lett.*, 33, L07305,

Patane, D., F. Ferrari, E. Giampiccolo, and S. Gresta (2003), A PC-based computer package for automatic detection and location of earthquakes: application to a seismic network in eastern Sicily (Italy), methods and applications of signal processing in seismic network operations, in *Lecture Notes in Earth Sciences,* 98, 89-129.

Peacock, S., S. Crampin, D. C. Booth, and J. B. Fletcher (1988), Shear-wave splitting in the Anza seismic gap southern California: temporal variations as possible precursors, *J. Geophys. Res.*, 93, 3339–3356.

Peng, Z., and Y. Ben-Zion (2004), Systematic analysis of crustal anisotropy along the Karadere-Düzce branch of the North Anatolian fault, *Geophys. J. Int.*,159, 253-274.

Peng, Z., and Y. Ben-Zion (2005), Spatiotemporal variations of crustal anisotropy from similar events in aftershocks of the 1999 M7.4 İzmit and M7.1 Düzce, Turkey, earthquake sequences, *Geophys. J. Int.*, 160, 1027-1043.

Peng, Z., Y. Ben-Zion, A. Michael, L. Zhu (2003), Quantitative analysis of seismic fault zone waves in the rupture zone of the 1992 Landers, California, earthquake: evidence for a shallow trapping structure, *Geophys. J. Int.*, 155, 1021-1041.

Peng, Z., L. T. Long, and P. Zhao (2011), The relevance of high-frequency analysis artifacts to remote triggering, *Seismol. Res. Lett.*, 82(5), 654-660.

Peng, Z., and P. Zhao (2009). Migration of early aftershocks following the 2004 Parkfield earthquake, *Nature Geosci.*, 2, 877-881.

Pischiutta, M., F. Salvini, J. Fletcher, A. Rovelli, Y. Ben-Zion (2012), Horizontal polarization of ground motion in the Hayward fault zone at Fremont, California: dominant fault-high-angle polarization and fault-induced cracks, *Geophys. J. Int.*, 188 (3), 1255–1272.

Pischiutta, M., A. Rovelli, F. Salvini, G. Di Giulio, Y. Ben-Zion (2013), Directional resonance variations across the Pernicana fault, Mt. Etna, in relation to brittle deformation fields, *Geophys. J. Int.*, 193 (2), 986–996.

Rasendra, N., M. Bonnin, S. Mazzotti, and C. Tiberi. (2014), Crustal and upper mantle anisotropy related to fossilized transpression fabric along the Denali Fault, northern Canadian Cordillera, *Bull. Seismol. Soc. Am.*, 104(4):1964–1975.

Rastin, S., C. Unsworth, R. Benites, and K. Gledhill (2013). Using real and synthetic waveforms of the Matata swarm to assess the performance of New Zealand GeoNet

phase pickers, *Bull. Seismol. Soc. Am.*, 103, 2173-2187.

Rawles C., and C. Thurber (2015), A non-parametric method for automatic determination of *P*-wave and *S*-wave arrival times: application to local micro earthquakes, *Geophys. J. Int.,* 202, 1164-1179.

Restivo, A., and G. Helffrich (2006), Core-mantle boundary structure investigated using sks and skks polarization anomalies, *Geophys. J. Int.*, 165, 288-302

Riahi, N., and P. Gerstoft (2015), The seismic traffic footprint: Tracking trains, aircraft, and cars seismically, *Geophys. Res. Lett.*, 42, 2674–2681.

Rockwell T.K., T.E. Dawson, J.Y. Ben-Horin, G. Seitz (2015), A 21-event, 4000-year history of surface ruptures in the Anza Seismic Gap, San Jacinto Fault, and implications for long-term earthquake production on a major plate boundary fault, *Pure appl. Geophys*, 172:1143.

Rost, S., and C. Thomas (2002), Array seismology: Methods and applications, *Rev. Geophys.,* 40 (3), 1008.

Ross, Z.E., and Y. Ben-Zion (2014). Automatic picking of direct P, S seismic phases and fault zone head waves, *Geophys. J. Int.,* 199, 368-381.

Salisbury, J. B., T. K. Rockwell, T. J. Middleton, and K. W. Hudnut (2012), LiDAR and field observations of slip distribution for the most recent surface ruptures along the central San Jacinto Fault, *Bull. Seismol. Soc. Am.*, 102(2), 598–619.

Sanders, C. O., and H. Kanamori (1984), A seismotectonic analysis of the Anza seismic gap, San Jacinto Fault Zone, southern California, *J. Geophys. Res.*, 89, 5873–5890, doi:10.1029/JB089iB07p05873.

Saragiotis, C., L. Hadjileontiadis, and S. Panas (2002), PAI-S/K: A robust automatic seismic P phase arrival identification scheme, *IEEE Trans. Geosci. Remote Sens.*, 40, 1395-1404.

Savage, M. K. (1999), Seismic anisotropy and mantle deformation: What have we learned from shear wave splitting?, *Rev. Geophys.*, 37(1), 65–106,

Savage, M.K., X.R. Shih, R.P. Meyer, and R.C. Aster. (1989), Shear-wave anisotropy of active tectonic regions via automated S-wave polarization analysis, *Tectonophysics*, 165, 279–292.

Savage, M. K., A. Wessel, N. Teanby and T. Hurst (2010), Automatic measurement of shear wave splitting and applications to time varying anisotropy at Mt. Ruapehu volcano, New Zealand, *J. Geophys. Res.*, 115, B12321.

Sayers, C.M. (1994), The elastic anisotropy of shales, *J. Geophys. Res.*, 99(B1): 767-774.

Shearer, M. P., 2009. Introduction to seimology, 2nd ed., 119 pp., London, Cambridge University Press.

Schaff, D. P. (2008), Semiempirical statistics of correlation-detector performance, *Bull. Seismol. Soc. Am.,* 98, no. 3, 1495–1507.

Scholz, C. H. (1998), Earthquakes and friction laws, *Nature*, 391, 37-42.

Schorlemmer, D. and S. Wiemer (2005), Microseismicity data forecast rupture area, *Nature*, 434, 1086.

Seeber, L., J.G. Armbruster, N. Ozer, M. Aktar, S. Baris, D. Okaya, Y. Ben-Zion, and E. Field (2000), The 1999 Earthquake Sequence along the North Anatolia Transform at the Juncture between the Two Main Ruptures, in The 1999 İzmit and Düzce Earthquakes: preliminary results, pp. 209–223, ed. Barka et al., Istanbul Technical University.

Shelly, D. R., G.C. Beroza, and S. Ide (2007), Non-volcanic tremor and low-frequency earthquake swarms, *Nature*, 446, 305–307.

Shi, Z., and Y. Ben-Zion (2006), Dynamic rupture on a bimaterial interface governed by slip-weakening friction, *Geophys. J. Int.*, 165, 469-484.

Shih, X. R., and R. P. Meyer (1990), Observation of shear wave splitting from nature events: South Moat of Long Valley caldera, California, June 29 to August 12, 1982, *J. Geophys. Res.*, 95, 11,179–11,196.

Sibson, R. (1994), Crustal stress, faulting and fluid flow, Geological Society, London, Special Publications 1994, v. 78, p. 69-84

Sibson, R. (2003), Thickness of the seismic slip zone, *Bull. Seismol. Soc. Am.*, 93, 1169-1178.

Silver, P., and W. Chan (1991), Shear-wave splitting and subcontinental mantle deformation, *J. Geophys. Res.-Solid Earth*, 96, 16429-16454.

Silver, P., and M. Savage (1994), The interpretation of shear-wave splitting parameters in the presence of 2 anisotropic layers, *Geophys. J. Int.*, 119, 949-963.

Sleeman, R., and T. van Eck (1999), Robust automatic P-phase picking: an on-line implementation in the analysis of broadband seismogram recordings, *Phys. Earth. Planet. Int.,* 113, 265-275.

Sykes, L., and S. Nishenko (1984), Probabilities of occurrence of large plate rupturing earthquakes for the San Andreas, San Jacinto and Imperial faults, California, *J. Geophys. Res.*, 89(B7), 5905–5928.

Syracuse, E., R. Holt, M. Savage, J. Johnson, C. Thurber, K. Unglert, K. Allan, S. Karaliyadda, M. Henderson (2012), Temporal and spatial evolution of hypocentres and

anisotropy from the Darfield aftershock sequence: implications for fault geometry and age, *New Zealand Journal of Geology and Geophysics*, 55, 287-293.

Tadokoro K., and M. Ando (2002), Evidence for rapid fault healing derived from temporal changes in S wave splitting, *Geophys. Res. Lett.*, 29:1047.

Tadokoro, K., M. Ando, S. Baris, K. Nishigami, M. Nakamura, S. Ucer, A. Ito, Y. Honkura, A. Isikara (2002), Monitoring of fault healing after the 1999 Kocaeli, Turkey, earthquake, *Journal of Seismology*, 6, 411-417.

Takanami, T., and G. Kitagawa (1988). A new efficient procedure for the estimation of onset times of seismic waves, *J. Phys. Earth*, 36, 267-290.

Teanby, N., J. Kendall, M. Van der Baan (2004), Automation of shear-wave splitting measurements using cluster analysis, *Bull. Seismol. Soc. Am.*, 94, 453-463.

Thurber, C., H. Zhang, F. Waldhauser, J. Hardebeck, A. Michael, D. Eberhart-Phillips (2006), Three-dimensional compressional wavespeed model, earthquake relocations, and focal mechanisms for the Parkfield, California, region, *Bull. Seismol. Soc. Am*, 96, S38-S49.

Tibi, R., G. Bock, Y. Xia, M. Baumbach, H. Grosser, C. Milkereit, S. Karakisa, S. Zunbul, R. Kind, J. Zschau (2001), Rupture processes of the 1999 August 17 Izmit and November 12 Düzce (Turkey) earthquakes, *Geophys. J. Int.*, 144, F1-F7.

Unglert, K., M. K. Savage, N. Fournier, T. Ohkura, and Y. Abe, (2011), Shear wave splitting, Vp/Vs and GPS during a time of enhanced activity at Aso caldera, Kyushu, *J. Geophys. Res.*, 116 (2011), p. B11203.

Unsworth, M., and P. A. Bedrosian (2004), Electrical resistivity structure at the SAFOD site from magnetotelluric exploration, *Geophys. Res. Lett.*, 31(12).

van der Elst, N. J., and E. E. Brodsky (2010), Connecting near-field and far-field earthquake triggering to dynamic strain, *J. Geophys. Res.*, 115, B07311.

Wang, J., and T. Teng (1997), Identification and picking of S-phase using an artificial neural network, *Bull. Seism. Soc. Am.,* 87, 1140-1149.

Wdowinski, S., B. Smith-Konter, Y. Bock, and D. Sandwell (2007), Diffuse interseismic deformation across the Pacific-North America plate boundary, *Geology*, 35, 311-314.

Yang, W., and E. Hauksson (2013), The tectonic crustal stress field and style of faulting along the Pacific North America Plate boundary in Southern California, *Geophys. J. Int*., 194 (1): 100-117.

Yang, W., Z. Peng, B. Wang, Z. Li and S. Yuan (2015), Velocity contrast along the rupture zone of the 2010 Mw6.9 Yushu, China earthquake from fault zone head waves, *Earth Planet. Sci. Lett*., 416, 91-97.

Yang, Z., A. Sheehan, and P. Shearer (2011), Stress induced upper crustal anisotropy in southern California, *J. Geophys. Res*., 116, B02302.

Yang, H., and L. Zhu (2010), Shallow low-velocity zone of the San Jacinto fault from local earthquake waveform modelling, *Geophys. J. Int.*, 183, 421–432.

Yang H., Z. Li, Z. Peng, Y. Ben-Zion, and F. L. Vernon (2014), Low velocity zones along the San Jacinto Fault, Southern California, from body waves recorded in dense linear arrays, *J. Geophys. Res*., 119, 8976–8990.

Yang, H., L. Zhu, and R. Chu (2009), Fault-plane determination of the 18 April 2008 Mt. Carmel, Illinois, earthquake by detecting and relocating aftershocks, *Bull. Seismol. Soc. Am.*, 99(6), 3413–3420.

Yao, D., J. I. Walter, X. Meng, T. E. Hobbs, Z. Peng, A. V. Newman, S. Y. Schwartz, and M. Protti (2017), Detailed spatiotemporal evolution of microseismicity and repeating earthquakes following the 2012 M_w 7.6 Nicoya earthquake, J. Geophys. Res. Solid Earth, 122, 524–542.

Yilmaz, Y.,O. Tuysuz, E. Yigitbas, S.C.Genc, and A.M.C. Sengor (1997), Geology and Tectonic Evolution of the Pontides. Robinson, A.G., AAPG, Tulsa, OK, USA, *Regional and Petroleum geology of the Black Sea and Surrounding Region: AAPG Memoir,* 68, pp. 183-226.

Yoon, C. E, O. O'Reilly, K. J. Bergen, and G. C. Beroza (2015), Earthquake detection through computationally efficient similarity search, *Sci. Adv.,* 2015;1:e1501057.

Zhang, H. J., C. Thurber, and P. Bedrosian (2009), Joint inversion for Vp, Vs, and Vp/Vs at SAFOD, Parkfield, California, *Geochem. Geophy. Geosy.*, 10, Q11002.

Zhang, H., Y. Liu, C.Thurber, and S. Roecker (2007), Three-dimensional shear-wave splitting tomography in the Parkfield, California, region, *Geophys. Res. Lett.*, 34.

Zhang, H., Thurber, C.(2007), Estimating the model resolution matrix for large seismic tomography problems based on Lanczos bidiagonalization with partial reorthogonalization, *Geophys. J. Int.,* 170, 337-345.

Zhang H., C. Thurber, and C. Rowe (2003). Automatic P-wave arrival detection and picking with multiscale wavelet analysis for single-component recording, *Bull. Seism. Soc. Am.*, 93 , 1904 -1912.

Zhang, Z., and S. Y. Schwartz (1994), Seismic anisotropy in the shallow crust of the Loma Prieta segment of the San Andreas fault system, *J. Geophys. Res.*, 99(B5), 9651–9661.

Zhang, J., H. Zhang, E. Chen, Y. Zheng, W. Kuang, and X. Zhang (2014), Real-time earthquake monitoring using a search engine method, *Nature Comm.*, 5:5664.

Zhao, P., Z. G. Peng, Z. Q. Shi, M. A. Lewis, and Y. Ben-Zion (2010), Variations of the velocity contrast and rupture properties of M6 earthquakes along the Parkfield section of the San Andreas fault, *Geophys. J. Int.*, 180, 765-780.

Zhao, Y., and K. Takano (1999), An artificial neural network approach for broadband seismic phase picking, *Bull. Seism. Soc. Am.,* 89(3), 670-680.

Zhu L., and L. A. Rivera (2002), A note on the dynamic and static displacements from a point source in multi-layered media, *Geophy. J. Int.*, 148, 619-627.

Zigone D., Y. Ben-Zion, M. Campillo and P. Roux (2015), Seismic tomography of the Southern California plate boundary region from noise-based Rayleigh and Love waves, *Pure Appl. Geophys.*, 172(3), 1007–1032.